AB INITIO NO CORE SHELL MODEL STUDY FOR LIGHTER NUCLEI

Ph.D. THESIS

by

ARCHANA SAXENA

DEPARTMENT OF PHYSICS
INDIAN INSTITUTE OF TECHNOLOGY ROORKEE
ROORKEE - 247 667 (INDIA)
MAY, 2019

AB INITIO NO CORE SHELL MODEL STUDY FOR LIGHTER NUCLEI

A THESIS

Submitted in partial fulfilment of the requirements for the award of the degree

of

DOCTOR OF PHILOSOPHY

in

PHYSICS

by

ARCHANA SAXENA

DEPARTMENT OF PHYSICS
INDIAN INSTITUTE OF TECHNOLOGY ROORKEE
ROORKEE - 247 667 (INDIA)
MAY, 2019

INDIAN INSTITUTE OF TECHNOLOGY ROORKEE
ROORKEE

CANDIDATE'S DECLARATION

I hereby certify that the work which is being presented in this thesis entitled, **"AB INITIO NO CORE SHELL MODEL STUDY FOR LIGHTER NUCLEI"** in partial fulfilment of the requirements for the award of the Degree of **Doctor of Philosophy** and submitted in the Department of Physics of the Indian Institute of Technology Roorkee, Roorkee is an authentic record of my own work carried out during a period from July, 2014 to May, 2019 under the supervision of Dr. Praveen Chandra Srivastava, Assistant Professor, Department of Physics, Indian Institute of Technology Roorkee, Roorkee.

The matter presented in this thesis has not been submitted by me for the award of any other degree of this or any other Institute.

(ARCHANA SAXENA)
Signature of Candidate

This is to certify that the above statement made by the candidate is correct to the best of my knowledge.

(**Praveen Chandra Srivastava**)
Signature of Supervisor

The Ph.D. Viva-Voce Examination of Ms. Archana Saxena, Research Scholar, has been held on . . . . . at the Department of Physics, IIT Roorkee, Roorkee, INDIA.

Chairman, SRC **Signature of External Examiner**

This is to certify that the student has made all the corrections in the thesis.

Signature of Supervisor **Head of the Department**
Dated: . . . . . .

ABSTRACT

The aim of the present thesis is to perform *ab initio* no core shell model (NCSM) calculations for lighter nuclei and to perform shell model calculations using valence-space Hamiltonians derived with *ab initio* approaches like in-medium similarity renormalization group (IM-SRG) and coupled-cluster effective interaction (CCEI) for heavier *sd* shell nuclei.

A systematic study of low-lying energy spectrum for $^{18-23}$O and $^{18-24}$F isotopes using NCSM is presented. We have used INOY potential, which is a two body interaction but also has the effect of three body forces by short range and nonlocal character. We have also performed calculations with N3LO, and N2LOopt interactions and corresponding results are compared with the experimental data and phenomenological interaction USDB. The largest model space we have reached for $^{18-21}$O and $^{18-19}$F is N_{max}=6 and for other oxygen and fluorine isotopes is N_{max}=4. We have also discussed the binding energy for O and F chain. The over binding in ground state (g.s.) energy in neutron-rich oxygen isotopes is observed in our largest model space calculations.

We have calculated the energy spectra for $^{18-22}$N isotopes using NCSM. To calculate the energy spectrum we have used three different NN potentials: INOY, N3LO, and CDB2K. The calculations have been done at $\hbar\Omega$=20 MeV, 14 MeV and 12 MeV

using INOY, N3LO and CDB2K potentials, respectively. The results of INOY interaction are in reasonable agreement with the available experimental data.

We present *ab initio* shell model calculations for electric quadrupole moments and magnetic dipole moments of *sd* shell nuclei with interactions derived from *ab initio* approaches: IM-SRG and CCEI. The results are in a reasonable agreement with the available experimental data as well as with the results from the phenomenological USDB effective interaction. We have also calculated $B(E2; 2_1^+ \rightarrow 0_1^+)$ for Ne, Mg and Si isotopes using *ab initio* interactions.

The Gamow-Teller transition strength $B(GT)$ distributions of *sd* shell nuclei for thirteen transitions using *ab initio* effective interactions: IM-SRG and CCEI are reported. The aim of the present work is to test the predictive power of *ab initio* effective interactions for available experimental data of $B(GT)$ distributions of *sd* shell nuclei. The *ab initio* results of the Gamow-Teller (GT_+/GT_-) strength distributions reproduce the experimental data with reasonable agreement. We also calculate the electron capture reaction rates for ^{23}Na(e$^-$, ν)^{23}Ne and ^{25}Mg(e$^-$, ν)^{25}Na using *ab initio* and USDB interactions.

We have performed shell model calculations to describe the structure of ^{35,37,39}S isotopes using SDPF-U and SDPFMW interactions. Protons and neutrons are restricted to the *sd*-shell for $N < 20$ and neutrons start to fill the pf-shell for $N > 20$. The natural parity states are described by only in-shell mixing and unnatural parity states with 1p-1h inter-shell neutron excitations. The calculated energy levels, electromagnetic properties, and spectroscopic factors are in good agreement with the recently available experimental data.

Finally, summary and future prospects are reported.

List of Publications

Articles in Journals

1. *Ab initio* no-core shell model study of neutron-rich nitrogen isotopes,
   Archana Saxena and P. C. Srivastava,
   Prog. Theor. Exp. Phys. **2019**, 073D02 (2019).
2. *Ab initio* calculations of Gamow-Teller strengths in the *sd* shell,
   Archana Saxena, P. C. Srivastava and T. Suzuki,
   Phys. Rev. C **97**, 024310 (2018).
3. First-principles results for electromagnetic properties of *sd* shell nuclei,
   Archana Saxena and P. C. Srivastava,
   Phys. Rev. C **96**, 024316 (2017).
4. ^{35,37,39}S isotopes in $sd-pf$ space : Shell-model interpretation,
   Archana Saxena, P. C. Srivastava, J. G. Hirsch, V.K.B. Kota and M. J. Ermamatov,
   Nuclear Physics A **961**, 68-77 (2017).
5. *Ab initio* description of collectivity for *sd* shell nuclei,
   Archana Saxena, A. Kumar, V. Kumar, P. C. Srivastava and T. Suzuki,
   Hyperfine Int. **240**, 37 (2019).
6. No core shell model study of $^{18-23}$O and $^{18-24}$F isotopes,
   Archana Saxena and P. C. Srivastava,
   Communicated for publication, arXiv:1812.08744.
7. Isospin symmetry in $B(E2)$ values: Coulomb excitation study of ^{21}Mg,
   P. Ruotsalainen, J. Henderson, G. Hackman, G. H. Sargsyan, K. D. Launey,
   Archana Saxena, P. C. Srivastava et al.,
   Phys. Rev. C **99**, 051301(R)(2019).

Papers in Conferences/Symposium:

1. Study of Nitrogen Isotopes with No Core Shell Model
   Archana Saxena and P. C. Srivastava
   Proceedings of DAE International Symposium on Nuclear Physics **63**, 88 (2018).

2. Doubly open-shell nuclei with ab initio approaches
   Archana Saxena, A. Kumar, V. Kumar and P. C. Srivastava,
   Proceedings of DAE International Symposium on Nuclear Physics **63**, 102 (2018).

3. Shell model results of Gamow-Teller transition strengths for ^{48}Ti$(^3He, t)^{48}$V reaction
   V. Kumar, A. Kumar, **Archana Saxena**, P. C. Srivastava,
   Proceedings of DAE International Symposium on Nuclear Physics **63**, 106 (2018).

4. No core shell model results for oxygen chain
   Archana Saxena and P. C. Srivastava
   Proceedings of DAE Symposium on Nuclear Physics **62**, 76 (2017).

5. Ab initio no core shell model results for sd shell
   Archana Saxena and P. C. Srivastava
   Proceedings of DAE Symposium on Nuclear Physics **61**, 68 (2016).

Workshops/Conferences/Symposia Attended:

1. 63^{rd} DAE International Symposium on Nuclear Physics-2018
   Bhabha Atomic Research Centre, Mumbai
   Dec 10-14, 2018.

2. Zakopane Conference 2018 on nuclear Physics, Poland during Aug 26-Sep 2, 2018.

3. 62^{nd} DAE Symposium on Nuclear Physics-2017
   Thapar University, Patiala
   Dec 20-24, 2017.

4. Attended a doctoral training program on "Microscopic Theories of Nuclear Structure, Dynamics and Electroweak Currents" at ECT* (European Centre for Theoretical Studies in Nuclear Physics and Related Areas) in Trento (Italy) for the period June 12-30, 2017.

5. SERC School on Nuclear Physics from New Perspectives
   Bharathiar University, Coimbatore
   Feb 7-27, 2017.

6. 61^{st} DAE-BRNS Symposium on Nuclear Physics-2016
   SINP, Kolkata
   Dec 5-9, 2016.

7. DST-SERC School on Modern Microscopic Approaches in Nuclear Physics
   University of Kashmir, Srinagar
   May 17-June 6, 2016.

8. 2^{nd} DAE-BRNS Workshop on Evaluation of Nuclear Structure and Decay Data (ENSDD-II)
   Homi Bhabha Centre for Science Education, Mumbai
   Feb 29-March 4, 2016.

9. DST-SERB school on Modern Theories of Nuclear Structure
   IIT Roorkee, Roorkee
   Feb 23-March 5, 2015.

ACKNOWLEDGMENTS

The completion of this thesis would not have been possible without the support and love of the people around me. During Ph.D. the role of a supervisor is the most important, he is the person who gives the right direction and strength. So, first of all, I would like to express my sincere gratitude to my supervisor **Prof. Praveen Chandra Srivastava** for his continuous support, guidance, and motivation during this Ph.D. I am very grateful for his exploration of new ideas, thoughtful and detailed comments. Thank you so much for always standing by my side in this journey from day one to the completion of this thesis.

Also, I would like to acknowledge my thesis committee: Prof. B. D. Indu (Present SRC Chairman), Prof. P. Arumugam (Internal expert), Prof. A. S. Maurya (External expert), Prof. T. Nautiyal (Former DRC chairman), Prof. D. Kaur (Present DRC Chairman) for their positive criticism, remarks, and encouraging words in achieving my goal. I owe a great deal of appreciation and gratitude to all my collaborators Prof. T. Suzuki, Prof. V.K.B. Kota, Prof. Jorge G. Hirsch and Prof. M. J. Ermamatov for their suggestions and help in this thesis work. I would like to thank Prof. P. Navrátil and Prof. C. Forssén for several suggestions on No Core Shell Model from the very beginning. Also, I am grateful to Prof. S. R. Stroberg, Prof. J. D. Holt and Prof. G. R. Jansen for tremendous help on *ab initio* interactions. I would like to

acknowledge Prof. A. K. Jain for his support and motivation. I would like to thank Prof. K. L. Yadav, Head, Department of Physics, IIT Roorkee, for providing the basic infrastructural facilities for carrying out the research work. I would like to express my heartfelt thank to all the teaching and non teaching staff of the Department of Physics, IIT Roorkee. I gratefully acknowledge the financial support provided by MHRD and DST (Govt. of India), during the period of research. Also, I would like to acknowledge Oak computational facility at TRIUMF where several No Core Shell Model calculations have been done.

Life is incomplete without friends and love. I would like to acknowledge my friends *Nisha, Sarita, Manju, Anushri, Bhoomika di, Swati di, Swatu, Anil, Bharti, Lata, Tuli and Upasna* for making this journey beautiful. Sheetal, you are the priceless GOD-gift to me. I can not define our relationship in a single word. Also, I would like to express my sincere thanks to my husband *Gopal* for his continuous support, patience, believe and love during the whole period of my Ph.D. You are my shadow who was always with me in my ups and downs.

It is the family which gives you a name in this world. Therefore, I would like to express my deep love towards my parents who gave me this beautiful life, thank you so much Mummy and Papa. Also, I would like to acknowledge my *Big B (Vikas bhaiya), bro (Guddu)* and *Surbhi bhabhi*, you guys have a special place in my heart.

I would like to acknowledge my seniors and labmates *Dr. Vikas, Dr. Gagan, Pooja, Vishal, Ankit, Abhishek, Richa, Priyanka, Madhu and Jaikhomba* for providing me a healthy environment to work. I also acknowledge other NUCLEAR FAMILY members at IITR, which includes Prof. R. Chatterjee, Prof. A. Gourishetty, Prof. A. Deo, Prof. M. Maiti, and Prof. P. Jain. I would like to thank every single person with whom I have ever contacted.

Above all, I would like to thank *Lord Shiva* for EVERYTHING in my life.

Date: ..... **Archana Saxena**

Dedicated to My Parents

Sushila Devi and Bindravan Saxena

CONTENTS

LIST OF FIGURES

LIST OF TABLES

CHAPTER 1

INTRODUCTION

One of the aims in nuclear physics is to study the structure and dynamics of nuclei using available interactions between the nucleons. However, in doing so, we face several difficulties while solving the nuclear many body problem. The main difficulty is that the interaction between nucleons is complex. We do not know the exact form of the interaction because it is not uniquely defined. Also, solving nuclear many body problem is computationally challenging. This is because the quantum many body particles interact very strongly and exhibit the single-particle, collective and clustering correlations. So, there are two basic problems which we have to solve, first is the nucleon-nucleon (NN) interaction between nucleons and second is the solving the many body Schrödinger equation. For a realistic NN interaction, there are a number of unanswered questions like what is the form and range of the potential, mechanism behind the exchange force and the spin-isospin properties of the interaction, etc. The behaviour of NN potential can be understood in terms of exchange of mesons [1], where the long-range part of the NN interaction is governed by $\pi-$ mesons, medium range by scalar mesons like $\sigma-$ mesons and the repulsive short range by the $\omega-$ mesons. In the early 1960s and 70s, Quantum Chromo-Dynamics (QCD)

was developed for explaining the nuclear force. In this theory hadrons are not fundamental, but they are made up of quarks which have color charge and interact by gluons which are the exchange particles of the strong force. But at low energies, it is very difficult to apply QCD because the interaction is very strong and we cannot use perturbative methods. So, we have to use NN potential semi phenomenologically. More recently, the nuclear force from the chiral effective field theory (χEFT) was introduced by Weinberg [2, 3]. The χEFT provides a bridge between QCD and hadronic systems [4]. Using this theory we define different energy scales in nature. It provides a cut off energy scale known as chiral symmetry breaking scale $\Lambda_{QCD} \approx$ 1 GeV below which the degree of freedom are pions and nucleons. At the present time many high-quality NN potentials [5–8] are available with parameters fitted by the NN scattering data and deuteron bound state. These NN potentials will now be used as input in many body techniques to solve nuclear many body problem.

Now, we come to the second problem which is to solve the non relativistic quantum many body Hamiltonian using NN potentials. Many body calculations with the high-quality NN potentials are very difficult and require high computing power and sophisticated method. With the recent advances in the computational facilities, it is now possible to study the lighter nuclei using *ab initio* approaches. The aim of the *ab initio* methods is to explain the nuclei from the first principle assuming interacting nucleons as non relativistic point-like particles.

Recently, many body methods like, no-core shell model (NCSM) [9], Green function Monte Carlo (GFMC) [10], the coupled-cluster (CC) [11, 12] and in-medium similarity renormalization group (IM-SRG) [13] are used to study the nuclear structure physics. In the present thesis, we focus on NCSM method to study the nuclear structure properties of nuclei. In NCSM all the nucleons are active and treated on equal footing. Lately, the NCSM has become a reliable tool to study the structure of nuclei microscopically. It gives good results where it is applicable and the only method capable to solve Schrödinger equation using nonlocal interactions. This method is limited to lower mass region (A$\sim$ 20) of nuclear chart. To study heavier

nuclei we use other methods.

Due to the limitation on Hilbert space, there is another method to study medium and higher mass nuclei in which valence space Hamiltonians can be derived from *ab initio* approaches and then used in the shell model calculations [14–19]. In this approach, we start from a few body Hamiltonian which consists of two- and three body interactions from χEFT. Stroberg et al. derived a mass-dependent Hamiltonian for *sd* shell nuclei using the IM-SRG approach [13, 20]. Similarly, an effective Hamiltonian for *sd* shell by applying a unitary transformation from the CC approach has been developed [11]. The g.s. energies and low-lying spectra are well reproduced with IM-SRG and CCEI [11, 20]. These effective interactions can be tested for recently available experimental data for the electromagnetic moments, electromagnetic transitions, $B(GT)$ strengths and electron capture rates. The shell model is also applicable to study the pairing correlations for the *sd* shell nuclei [21].

In the next section we will discuss the evolution of NCSM and formalism in chapter 2.

1.1 Evolution of the *ab initio* NCSM

The single-particle shell model was initially used to study the structure of atomic nuclei using NN effective interactions [22]. At the earlier stage, these effective interactions were purely empirical and based on fitting methods but recently these effective interactions were obtained from microscopic approaches. In the starting, these NN interactions from the microscopic approaches constructed from Bloch- Horowitz-Brandow perturbation theory (BHBPT) [23]. This approach was a success but it has also faced some problems such as

- the NN matrix elements of the G-matrix [24, 25] depending upon starting energy parameter was not well defined.
- contributions of the spurious center-of-mass (COM) motion.

- negligence of the many body forces.
- because of the tensor part in the NN force, a poor convergence rate of the intermediate-state summations for each term in the PT expansion (also called Vary-Saur-Wong (VSW) effect) [26].
- non convergence (in reaction matrix G) of the PT series [27, 28].

Later the divergence in PT expansion for NN effective interaction was generalized by Schuan and Weidenmüler [29, 30]. After this, it was realized that a non perturbative approach is required to study nuclear structure properties microscopically. With the recent advances in computing power, a new approach like NCSM has been made possible. In NCSM all the nucleons are active *i.e.* we have to solve the Schrödinger equation for A nucleons numerically. In this method, we get rid of many problems like excitations of nucleons from core such as VSW effect [26] and core-polarization effects [28,31] as there is no core in NCSM. The NCSM being a non-perturbative approach, there are no issues regarding the convergence in this expansion. The spurious COM motion has been also removed in this approach. The solutions of $A = 3$ and $A = 4$ in NN coordinates were made possible in 1980's and 1990's, respectively. The diagonalization of Hamiltonian with realistic NN interactions gives a convergent approach to study the structure of $A = 3$ and $A = 4$ nuclei microscopically [32–34]. In 2000 this approach was named "*ab initio* NCSM" where all the nucleons are important in solving the problem exactly and all the underlying Hamiltonian symmetries are preserved [35, 36]. For the very first time, the NCSM calculations were performed with real NNN interactions in 2002 [37]. Using NCSM approach, the g.s. energy and the excitation spectrum were calculated. After this other physical observables like electromagnetic moments, transition strengths of nuclei were calculated [38–41]. The renormalization of all the operators was also needed after this work in a truncated model space. Stetcu et al. [41] showed for the first time how renormalization of an operator under a truncated model space is highly dependent on its range. The initial NCSM calculations were focused to get the correct form of effective operators and

the suitable set of basis configurations to use in the NCSM calculations. In Ref. [42], the importance of using relative kinetic-energy operator, and in Refs. [43, 44], importance of suitable set of basis configuration such as Hartree-Fock rather than a single-particle HO were reported. The NCSM calculations were also compared with other many body methods like BHB PT results, so that we can see up to which order PT was breaking down or leading to a reasonable approximation of the "exact" results [45,46]. In the previous years, the progress of NCSM has been very fast with the advances in computer resources. Now, the NCSM application in the nuclear reactions is also under progress. In the chapter 2 we will discuss the NCSM formalism, the effective NN interaction, and renormalization scheme.

1.2 Overview of the present work

The aims of the present thesis are as follows:

1. to perform *ab initio* NCSM calculations for lower mass *sd* shell nuclei $^{18-23}$O and $^{18-24}$F and also locate the drip-line using NN INOY interaction.

2. to study N isotopes far from the stability line using NCSM.

3. to test the Hamiltonians derived from *ab initio* approaches like IM-SRG and CCEI for the calculation of the electromagnetic properties of nuclei: the magnetic and quadrupole moments.

4. to calculate the GT- strengths of *sd* shell nuclei with *ab initio* interactions which are applicable to evaluate the weak rates, important for astrophysical processes.

5. to predict the energy spectrum for unnatural parity states of ^{35,37,39}S isotopes in $sd-pf$ space and also to calculate the spectroscopic factor strengths and electromagnetic properties for comparison with recently available experimental data.

The research work in this thesis has been presented in the form of eight chapters. The introduction to the historical development of no-core shell model (NCSM) is presented in the **chapter 1**.

In **chapter 2**, we present the formalism of NCSM. In the Hamiltonian, we have used up to two body interaction in the present thesis. The Hamiltonian used in the calculations is an effective Hamiltonian in model space P and cut off by model space size parameter N_{max}. The Hamiltonian is dependent on variational parameter harmonic oscillator (HO) frequency $\hbar\Omega$ and parameter N_{max}. For the diagonalization of the matrices, we have used pANTOINE code [47]. For diagonalization, it uses Lanczos method to find eigenvalues and eigenvectors of a sparse and huge, Hermitian matrix. This code can handle the dimensions up to $\sim 10^{10}$ in m-scheme. With this code, we can calculate the wave functions, occupancies, the electromagnetic moments and transitions, the proton and neutron radii. We also discuss the computational issue for the diagonalizations in the calculations.

In **Chapter 3**, we have done the systematic study of the low-lying energy spectrum (positive parity) for oxygen ($^{18-23}$O) and fluorine ($^{18-24}$F) chain using *ab initio* NCSM [48]. We have used inside nonlocal outside Yukawa (INOY) potential [8, 49], which is a two body interaction but also have the effect of three body forces by short range and nonlocal character. We have also performed calculations with next-to-next-to-next-leading order (N3LO), and next-to-next leading order (N2LOopt) interactions [50, 51] and corresponding results are compared with the experimental data and phenomenological interaction USDB. The INOY and N3LO are the effective interactions while N2LOopt is a bare interaction, *i.e.* this interaction is without the Okubu-Lee-Suzuki transformation [52–54]. The largest model space we have reached for $^{18-21}$O and $^{18-19}$F is N_{max}=6 and for other oxygen and fluorine isotopes is N_{max}=4. The over binding in g.s. energy in neutron rich oxygen isotopes is observed in our largest model space calculations. The results with INOY interaction show good agreement with the experimental data. We have also shown the occupancy of different orbitals involved corresponding to the largest model space in the calculations. The

most important finding of the present study is the location of drip-line in oxygen isotopes even using only two body interaction.

In **Chapter 4**, a systematic study has been done for $^{18-22}$N isotopes using NCSM [55]. To calculate the energy spectrum we have used three different NN potentials: INOY, N3LO from chiral effective field theory and charge-dependent Bonn 2000 (CDB2K) [7]. The calculations have been done at $\hbar\Omega$= 20 MeV, 14 MeV and 12 MeV using INOY, N3LO and CDB2K potentials, respectively. Apart from this, we have also performed shell model calculations with the YSOX interaction [56] which includes (0-3) $\hbar\Omega$ excitations in full $p-sd$ model space. The results with INOY interaction show good agreement with the experimental data in comparison to the other three interactions. The INOY interaction ($\hbar\Omega$= 20 MeV) gives correct g.s. for all $^{18-22}$N isotopes. We have also shown the occupancy of different orbitals involved corresponding to the largest model space (N_{max}= 4) in the present calculations. We also show the g.s energy of $^{18-22}$N isotopes corresponding to N_{max}= 4 model space size with INOY interaction at $\hbar\Omega$= 20 MeV. The g.s. energy follows the same trend as the experimental data.

In **Chapter 5**, we present *ab initio* shell model calculations for electric quadrupole moments and magnetic dipole moments of *sd* shell nuclei using valence-space Hamiltonians derived with two *ab initio* approaches [57]: IM-SRG [20] and CCEI [11]. These effective interactions are based on chiral effective field theory, where NN and $3N$ parts are taken from a N3LO chiral nucleon-nucleon and a N2LO chiral three-body interaction, respectively. The $\hbar\Omega$ values for IM-SRG and CCEI effective interactions are 24 MeV and 20 MeV, respectively. For both IM-SRG and CCEI, we use Λ_{NN} = 500 MeV for the chiral N3LO NN interaction, and Λ_{3N} = 400 MeV for the chiral N2LO $3N$ interaction. The results are in a reasonable agreement with the available experimental data as well as with the results from the phenomenological USDB effective interaction. Using these *ab initio* interactions we have also reported the $B(E2; 2_1^+ \rightarrow 0_1^+)$ for Ne, Mg and Si isotopes. This work will add more information to the available *ab initio* results for the spectroscopy of *sd* shell nuclei.

In **Chapter 6**, we have reported a systematic shell model study using *ab initio* effective interactions for Gamow-Teller transition strength distribution of *sd* shell nuclei [58]. The *ab initio* effective interactions are based on IM-SRG and CCEI approaches. The aim of the present work is to test the predictive power of *ab initio* effective interactions for available experimental data of Gamow-Teller strength distributions of *sd* shell nuclei. In the present study, we perform calculations for ^{20}Ne $\rightarrow$ ^{20}F, ^{23}Na $\rightarrow$ ^{23}Mg, ^{23}Na $\rightarrow$ ^{23}Ne, ^{24}Mg $\rightarrow$ ^{24}Na, ^{24}Mg $\rightarrow$ ^{24}Al, ^{25}Mg $\rightarrow$ ^{25}Al, ^{26}Mg $\rightarrow$ ^{26}Na, ^{26}Mg $\rightarrow$ ^{26}Al, ^{26}Si $\rightarrow$ ^{26}Al, ^{27}Al $\rightarrow$ ^{27}Si, ^{28}Si $\rightarrow$ ^{28}P, ^{31}P $\rightarrow$ ^{31}Si, and ^{32}S $\rightarrow$ ^{32}P transitions. The results are also compared with the phenomenological USDB and experimental data. The *ab initio* results of the Gamow-Teller (GT_+/GT_-) strength distributions reproduce the experimental data with reasonable agreement. We have also calculated the electron capture reaction rates for ^{23}Na(e^-, ν)^{23}Ne and ^{25}Mg(e^-, ν)^{25}Na. The GT calculated strengths are found to be applicable to evaluate nuclear weak rates for some lower-mass *sd* shell nuclei, such as ^{23}Na and ^{25}Mg, within a factor of 2-4 in stellar environments. These nuclear weak rates play important roles in astrophysical processes.

In **Chapter 7**, the structure of ^{35,37,39}S isotopes [59] is described by performing comprehensive shell model calculations with SDPF-U [60] and SDPFMW [61] interactions. Protons and neutrons are restricted to the *sd*-shell for $N < 20$, neutrons start to fill the pf-shell for $N > 20$. The natural parity states are described by only in-shell mixing and unnatural parity states with 1p-1h inter-shell neutron excitations. With SDPF-U interaction, reported are the results for natural parity states only because this interaction is not suitable for cross shell excitations. Overall the SDPFMW interaction is seen to be much better for describing simultaneously properties of levels of both parities in ^{37,39}S isotopes. We have also calculated the electric quadrupole and the magnetic dipole moments for ^{35,37,39}S and spectroscopic factors in ^{37}S. The shell model results are in good agreement with recently available experimental data.

In **Chapter 8**, an overall summary with future outlook is presented. Finally, we provide bibliography of this thesis.

CHAPTER 2

NO CORE SHELL MODEL FORMALISM

2.1 *Ab initio* NCSM Method

The no core shell model (NCSM) [35,36] is basically an extended version of standard shell model. In NCSM, all the nucleons are treated as active and there is no inert core, however in the standard shell model, a nucleus is treated as an inert closed shell core and valence nucleons. Thus, there is no effective single-particle energies in the NCSM and "no-core" in the name of approach. The powerful techniques which are based on the second quantization and developed for standard shell model calculations used here, so "shell model" in the name of approach. In the NCSM model we treat a nucleus as a system of A- point like particles, behaving non-relativistically and interacting by realistic NN interactions. Meaning of "realistic NN interactions" is that NN potentials fit the nucleon-nucleon phase shifts data with high precision up to 350 MeV energy. In this approach, we work in truncated HO basis. The reason behind choosing HO basis is that it allows for the use of single nucleon co-

ordinate basis while the shortcoming in this basis is due to its incorrect asymptotic behaviour. As we work in a truncated basis the standard accurate NN potentials, such as ArgonneV18 (AV18) [62], CDB2K [7], INOY [63] and to some extent the chiral N3LO [6, 50] generate short range correlations that can not be accommodated in many nucleon HO bases accessible at present computers. In order to include these short range correlations and speed up the convergence with the enlargement of basis, we use a renormalization procedure. This is a similarity transformation that softens the interactions and generate the effective operators for all the observables while preserving all the experimental quantities in the low-energy domain. The derived "effective" interactions still act among all A nucleons and preserve all the symmetries of the initial or bare NN interactions. There are two renormalization schemes that currently in use, one is Okubo-Lee-Suzuki (OLS) scheme [52–54, 64, 65] and other is Similarity Renormalization Group (SRG) [66]. In the present work we are using OLS technique.

Now a days, a new type of soft potentials has been developed, by using unitary transformations of the standard accurate NN potentials mentioned earlier like V_{lowk} [67, 68] and the SRG NN [66] potentials. There is an another type of soft phenomenological NN potentials which is based on inverse scattering named JISP (J-matrix inverse scattering potential) [5]. For simplifying many body calculations, JISP potentials are already normalized to some extent. So, we can perform NCSM calculations with these potentials without modifying or "bare".

2.1.1 NN interactions

An overview of some NN interactions is given below:

Chiral Potentials: these potentials are derived from χEFT. This theory acts as a bridge between QCD and nuclear structure. In this theory, we get very clear picture of the nuclear forces which are organized in terms of power counting scheme.

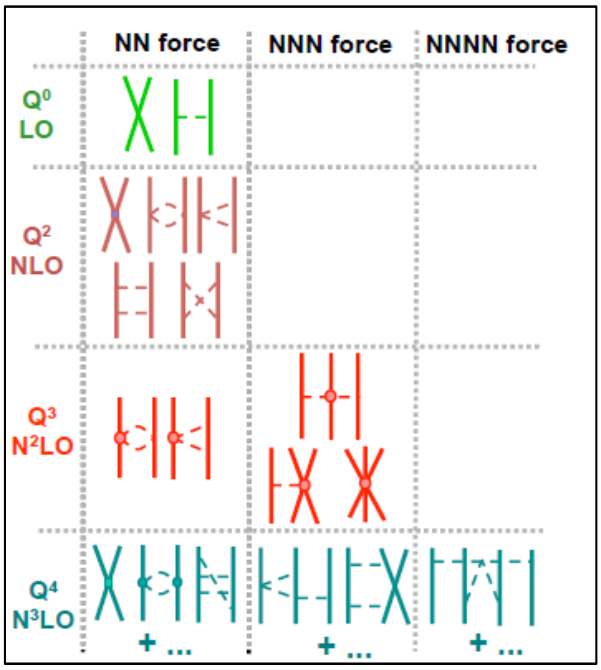

Figure 2.1: Schematic diagram for chiral forces. Solid lines and dashed lines correspond to nucleons and interacting pions, respectively. The solid dot starting from N2LO order at vertices explain the low-energy constants (LECs). These LECs are obtained from experimental data.

We can see the hierarchy of nuclear forces from Fig. 2.1 with a pictorial description. In this figure, every order in the perturbation series is arranged with an expansion in powers of $(\frac{Q}{\Lambda_\chi})$ with Q as a pion mass and Λ_χ as a chiral symmetry breaking scale of the order of 1 GeV. In this perturbation expansion the higher order term is lesser than the previous terms e.g. $V_{NNNN} \ll V_{NNN} \ll V_{NN}$. The important point in this theory is the determination of low-energy constants (LECs). These LECs appear in the diagram as a solid dot on vertical line. They appear because we are not dealing with full QCD theory and can be calculated from the experiments not from theory.

CD-Bonn Potential: This is meson exchange based potential. The charge dependent one boson exchange NN potential fitted to the proton-proton scattering data below 350 MeV was available in the year of 2000 with χ^2/datum of 1.01 for 2932 data and neutron proton data with χ^2/datum of 1.02 for 3058 data [7]. This

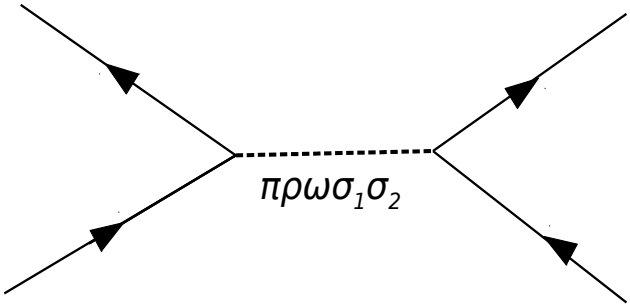

Figure 2.2: The CD-Bonn NN potential in terms of one-boson exchange Feynman diagrams.

potential reproduces the scattering data more accurately in comparison to the other NN potentials available at that time. This potential is derived from the predictions of the Bonn Full Model [69] where the charge symmetry and charge independence breaking in all partial waves with $J \leq 4$. This model includes all mesons π, η, ρ, ω and scalar-isoscalar σ bosons. This potential can be written in terms of the nonlocal covariant Feynman amplitudes for one-boson exchange. The one-boson exchange Feynman diagrams for the CD-Bonn NN potential is shown in Fig. 2.2.

INOY Potentials: Due to the internal structure of nucleons, the nonlocality is introduced in short range (1-1.5 fm) in NN interactions. The first nonlocal NN interaction was developed by Machleidt et al. [69] which was in momentum space and named as r-space long range nonlocal interaction [70]. The INOY NN interaction was prepared in coordinate space. Because of in coordinate space it was easy to control the range of local and nonlocal part. The INOY interaction was constructed in such a way that it must reproduce the known NN phase shifts data and the deuteron properties. The form of the INOY interaction is given as:

$$V_{ll'}^{full}(r,r') = W_{ll'}(r,r') + \delta(r-r')F_{ll'}^{cut}(r)V_{ll'}^{Yukawa}(r), \tag{2.1}$$

where,

$$F_{ll'}^{cut}(r) = \begin{cases} 1 - e^{-[\alpha_{ll'}(r-R_{ll'})]^2} & for\ r \geq R_{ll'} \\ 0 & for\ r \leq R_{ll'} \end{cases}$$

$W_{ll'}(r,r')$ and $V_{ll'}^{Yukawa}(r)$ parts are the nonlocal and Yukawa tail (it is taken from AV18 potential [62]), respectively. The $F_{ll'}^{cut}(r)$ is the cut off function for Yukawa tail. The $\alpha_{ll'}$ and $R_{ll'}$ are the fixed parameters which are 1.0 fm^{-1} and 2.0 fm, respectively. The nonlocal form $W_{ll'}(r,r')$ with parameters is given in Ref. [8]. These nonlocal INOY interactions are phenomenological and reproduces the $3N$ binding energies without adding a $3N$ force.

In the present NCSM calculations, we mainly focus on INOY NN potential. There are two reasons behind choosing this interaction 1) we can get converged results at lower model space size in comparison to other interactions and 2) INOY interaction has nonlocality character in its form. The nonlocality and three body forces are correlated with each other. So, this interaction also give the effect of three body forces without adding three body forces explicitly.

In the present thesis, we generate NN effective interactions using code which is developed by P. Navrátil [71].

2.1.2 Hamiltonian

We start with the $A-$ body Hamiltonian which is translationally invariant.

$$H_A = T_{rel} + V = \frac{1}{A}\sum_{i<j}^{A}\frac{(\vec{p}_i - \vec{p}_j)^2}{2m} + \sum_{i<j}^{A} V_{NN,ij} + ... \tag{2.2}$$

where m is the mass of the nucleon (it is taken 938.92 MeV, the average value of the proton and neutron masses) and A is the number of nucleons (*i.e.*, the mass number). The first term is relative kinetic energy defined in terms of momenta of each nucleon ($p_{i,j} = 1, 2, 3...A$), second term is nucleon-nucleon NN interaction having nuclear and

Coulomb part both. We modify Eq. 2.2, by adding to it the HO center-of-mass term $H_{CM} = T_{CM} + U_{CM}$, where $U_{CM} = \frac{1}{2}Am\Omega^2\vec{R}^2$, $\vec{R} = 1/A\sum_{i=1}^{A}\vec{r}_i$.

$$H_A^{\Omega} = H_A + H_{CM} = \sum_{i=1}^{A} h_i + \sum_{i<j}^{A} V_{ij}{}^{\Omega,A} = \sum_{i=1}^{A}\left[\frac{\vec{p}_i^2}{2m} + \frac{1}{2}m\Omega^2\vec{r}_i^2\right] + \sum_{i<j}^{A}\left[V_{NN,ij} - \frac{1}{2A}m\Omega^2(\vec{r}_i - \vec{r}_j)^2\right]. \quad (2.3)$$

In the final calculations CM term will be subtracted out. This term does not affect the properties of the system because the Hamiltonian (2.3) is translationally invariant. Now, Eq. 2.3 depends on A and HO frequency $\hbar\Omega$. The choice of $\hbar\Omega$ affect the calculated g.s. energy. As we are using Slater determinant basis, so, we also add the Lawson projection term [72] $\beta(H_{CM} - \frac{3}{2}\hbar\Omega)$ to shift the spurious CM excitations (because of spurious CM excitations we get unnecessary state in low energy spectrum). The eigenvalues of physical states are independent of the β. In the present work we have taken β=10.

2.1.3 Basis

To describe the intrinsic motion of a nuclear system the Jacobi coordinate HO basis [32–34] are the most favourable and it is easy to handle computationally only if the number of nucleons are very few ($A < 4$). As the nucleons are fermions, so we need to do the antisymmetrization of the basis but as the number of nucleons increases the antisymmetrization becomes very difficult. Hence, in the NCSM calculations both type of bases the Jacobi coordinate and single-nucleon Slater determinant HO basis are used depending upon the number of nucleons present in the system. For nuclear system ($A > 4$), it is more suitable to use Slater determinant HO basis. We use the m-scheme basis, where the projection of total angular momentum and parity remain conserved quantum numbers. Here, the antisymmetrization is easy but the dimension becomes large due to the presence of CM degrees of freedom and no JT coupling.

Here, one more thing is that we can use the powerful second quantization techniques as used in the shell model codes.

2.1.3.1 Slater determinant basis

The basic equation which we have to solve:

$$H|\psi_\alpha\rangle = E_\alpha|\psi_\alpha\rangle, \tag{2.4}$$

where, $H = H_0 + H_I$, the first term is the unperturbed Hamiltonian and second term is the interaction. To solve this Hamiltonian we use HO basis. The eigenstates of translationally invariant Hamiltonian are product of a wave function depending on relative coordinates and a wavefunction depending on the CM coordinates.

The normalized wave function for A nucleons is given by [73]:

$$\Psi = \frac{1}{\sqrt{n!}} \begin{vmatrix} \psi_{a_1}(x_1) & \psi_{a_1}(x_2) & \dots & \psi_{a_1}(x_n) \\ \psi_{a_2}(x_1) & \psi_{a_2}(x_2) & \dots & \psi_{a_2}(x_n) \\ \vdots & \vdots & & \vdots \\ \psi_{a_n}(x_1) & \psi_{a_n}(x_2) & \dots & \psi_{a_n}(x_n) \end{vmatrix} \tag{2.5}$$

Where, $\psi_i's$ are the single-particle HO wavefunctions. With the help of second quantization, the many body space can be created with annihilation and creation operators. Let $|\Phi_\alpha\rangle$ represents a Slater determinant of single-particle states,

$$|\Phi_\alpha\rangle = a_i^\dagger a_j^\dagger a_k^\dagger ... a_{n_\alpha}^\dagger |0\rangle \tag{2.6}$$

$$H_0|\Phi_\alpha\rangle = \epsilon_\alpha|\Phi_\alpha\rangle \tag{2.7}$$

$$\epsilon_\alpha = \epsilon_i + \epsilon_j + \epsilon_k + ... + \epsilon_n. \tag{2.8}$$

The index carrying by creation and annihilation operator represents the location of single particle in particular orbit. The full Hamiltonian is diagonalized in this basis. After diagonalization we get

$$\Psi_\alpha = \sum_\beta C_{\alpha\beta}|\Phi_\beta\rangle. \tag{2.9}$$

Here, exact solutions are represented by Ψ_α and many body basis states are represented by $|\Phi_\beta\rangle$. The expansion coefficients can be calculated as:

$$C_{\alpha\beta} = \langle\Psi_\alpha|\Phi_\beta\rangle, \tag{2.10}$$

2.1.3.2 Parameters in NCSM calculations

The NCSM calculations depend upon two basis space parameters, N_{max} and $\hbar\Omega$. The N_{max} parameter is defined as the maximum number of the total oscillator quanta allowed in the many body basis space above the minimum HO configuration for a particular nucleus followed by the Pauli principle. The $\hbar\Omega$ is the HO energy which is the spacing between major shells and each shell is defined by the quantum no. $N = 2n + l$ with $N = 0, 1, 2....$

In Fig 2.3, the example of N_{max}=2 configuration is shown for ^{6}Li nucleus which has 3 protons and 3 neutrons. According to the Pauli principle, the $N_{max} = 0$ configuration corresponds to lowest configuration in which there is no excitation of particles in the oscillator shells. The $N_{max} = 2$ configuration gives the excitation of 2 quanta in the oscillator shells. In NCSM, we want to reach N_{max} as maximum as possible, and after that extrapolates the g.s. energy as a function of N_{max} for a fixed value of $\hbar\Omega$. However, what proper value of $\hbar\Omega$ will be used is not known before hand. So, in practice, a series of calculations have been performed, with a range of $\hbar\Omega$ values. The optimal choice of $\hbar\Omega$ is usually accepted for which the g.s. energy value is minimum in the largest possible N_{max} space. In the *ab initio* NCSM formalism, when we use soft potentials we get converged NCSM results which means the g.s. energy

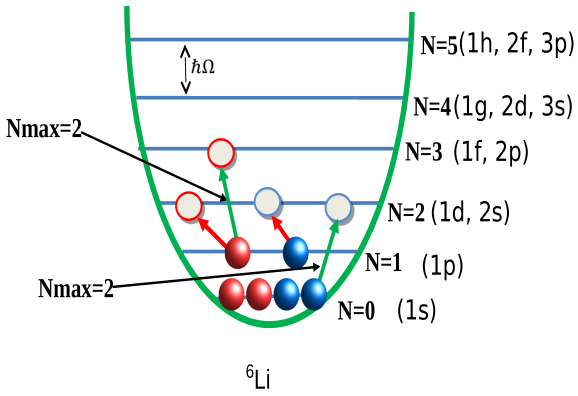

Figure 2.3: $N_{max} = 2$ configuration for ^{6}Li using HO potential.

of a particular nucleus has been calculated (or estimated) without any dependence on the NCSM parameters. But, situation is different when standard potentials that generate short-range correlations are used or when a not enough N_{max} truncation can be reached. For getting convergence we adopt renormalization scheme specified by a similarity transformation that softens the interactions. The derived "effective" interactions still act among all A nucleons and preserve all the symmetries of the initial or "bare" NN interactions. As mentioned earlier we use OLS scheme for renormalization.

2.1.3.3 Okubo-Lee-Suzuki (OLS) similarity transformation method

The full Hilbert space which is made up of a finite model space (P-space) and its complementary infinite space (Q-space). The P-space and Q-space are defined by P and Q projector operator, respectively. These operators satisfy the conditions $P^2 = P$, $Q^2 = Q$, $PQ = 0$, and $P + Q = 1$. We introduce an operator, ω, which is a transformation operator of similarity transformation of the Hamiltonian $e^{-\omega}He^{\omega}$, satisfies the condition $\omega = Q\omega P$. This operator acts as a mapping between the P

and Q spaces. The eigenstates of initial Hamiltonian can be denoted by $|k\rangle$ with eigenvalues E_k.

$$H|k\rangle = E_k|k\rangle. \tag{2.11}$$

The basis states of P and Q spaces are expressed as $|\alpha_P\rangle$ and $|\alpha_Q\rangle$. The $|\alpha_P\rangle$ belongs to $|\alpha_Q\rangle$ and follow the relation $Qe^{-\omega}He^{\omega}P = 0$. The $|\alpha_Q\rangle$ states can be expressed in terms of $|\alpha_P\rangle$ states with the help of ω operator,

$$\langle\alpha_Q|k\rangle = \sum_{\alpha_P}\langle\alpha_Q|\omega|\alpha_P\rangle\langle\alpha_P|k\rangle. \tag{2.12}$$

The operator ω can be find out from Eq. 2.12. Let d_P is the dimension of model space P and $\mathscr{K}$ which is a set of the d_P eigen vector vectors which satisfies the relation 2.12. The $d_P \times d_P$ which is a matrix having matrix elements $\langle\alpha_P|k\rangle$ for $|k\rangle \in \mathscr{K}$ is invertible, under this condition the operator ω,

$$\langle\alpha_Q|\omega|\alpha_P\rangle = \sum_{k\in\mathscr{K}}\langle\alpha_Q|k\rangle\langle\tilde{k}|\alpha_P\rangle, \tag{2.13}$$

where tilde denotes the matrix elements of inverse matrix $\langle\alpha_P|k\rangle$, e.g.,
$\sum_{\alpha_P}\langle\tilde{k}|\alpha_P\rangle\langle\alpha_P|k'\rangle = \delta_{k,k'}$, for $k, k' \in \mathscr{K}$.

For model space P, the Hermitian effective Hamiltonian is given by [53, 64]

$$\bar{H}_{eff} = [P(1+\omega\,\dagger\,\omega)P]^{1/2}PH(P+Q\omega P)[P(1+\omega\,\dagger\,\omega)P]^{-1/2}. \tag{2.14}$$

This Hamiltonian can be rewritten by using properties of ω operator

$$\bar{H}_{eff} = [P(1+\omega\,\dagger\,\omega)P]^{-1/2}(P+P\omega\,\dagger\,Q)H(Q\omega P+P)[P(1+\omega\,\dagger\,\omega)P]^{-1/2}. \tag{2.15}$$

The matrix elements of the effective Hamiltonian can be written as

$$\langle\alpha_P|\bar{H}_{eff}|\alpha_{P'}\rangle = \sum_{\alpha_{P''}}\sum_{\alpha_{P'''}}\sum_{kk'k''\in\mathscr{K}} \langle\alpha_P|\tilde{k''}\rangle\langle\tilde{k''}|\alpha_{P''}\rangle\langle\alpha_{P''}|\tilde{k}\rangle E_k\langle\tilde{k'}|\alpha_{P'''}\rangle\langle\alpha_{P'''}|\tilde{k'}\rangle\langle\tilde{k'}|\alpha_{P'}\rangle. \tag{2.16}$$

Here the summations over Q-space basis are removed. We get the energies E_k, $k \in \mathscr{K}$ in the model space using this effective Hamiltonian.

The Hermitian effective Hamiltonian (2.15) can also be obtained directly from unitary transformation of the original Hamiltonian

$$\bar{H}_{eff} = Pe^{-S}He^{S}P, \tag{2.17}$$

where S is an anti-Hermitian operator S=arctanh$(\omega - \omega\dagger)$. The decoupling conditions $Qe^{-S}He^{S}P = Pe^{-S}He^{S}Q = 0$ will be satisfied by this transferred Hamiltonian, see Fig. 2.4. For an A nucleon system, all terms up to A-body will arise in the effective Hamiltonian (2.16) even if the original Hamiltonian have just two-body or two-plus three body terms. In the present thesis we are using two body NN interaction.

The OLS method is applied in NCSM as follows: first we add the the CM Hamiltonian to the initial Hamiltonian. In the final many body calculations, the effect of CM Hamiltonian will be subtracted out. The CM Hamiltonian has in fact no effect on the intrinsic properties of the system due to translational invariance of the Hamiltonian. So, the modified Hamiltonian

$$\begin{aligned} H_A^{\Omega} = H_A + H_{CM} = \sum_{i=1}^{A} h_i + \sum_{i<j}^{A} V_{ij}{}^{\Omega,A} \\ = \sum_{i=1}^{A}\left[\frac{\vec{p}_i^{\,2}}{2m} + \frac{1}{2}m\Omega^2\vec{r}_i^{\,2}\right] + \sum_{i<j}^{A}\left[V_{NN,ij} - \frac{1}{2A}m\Omega^2(\vec{r}_i - \vec{r}_j)^2\right] + ... \end{aligned} \tag{2.18}$$

In A-nucleon Hamiltonian (2.18), the two-body part dominates so, two nucleon correlations in full space Hamiltonian are important. Using OLS method we construct

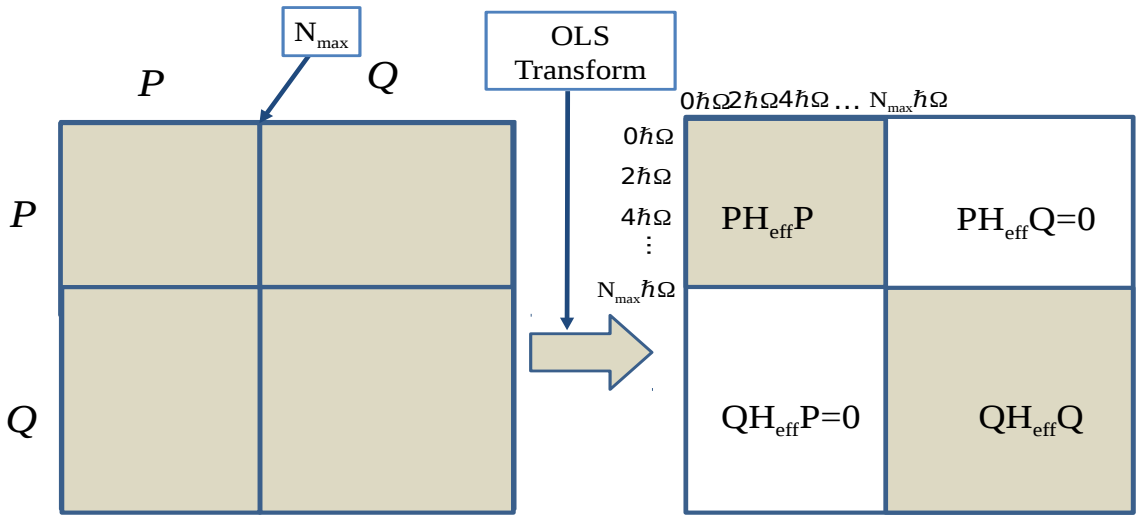

Figure 2.4: Schematic representation of OLS transformation

two-body effective interaction. Using the notation of Eq. 2.18, the two-nucleon effective interaction is given by

$$V_{2eff,12} = P_2[e^{-S_{12}}(h_1 + h_2 + {V_{12}}^{\Omega,A})e^{S_{12}} - (h_1 + h_2)]P_2. \tag{2.19}$$

with $S_{12} = arctanh(\omega_{12} - {\omega_{12}}^{\dagger})$ and P_2 is a two-nucleon model space projector. The two-nucleon model space is defined by a truncation N_{12max} corresponding to the A-nucleon N_{max}. For example, for A=3,4, $N_{12max} = N_{max}$, for p-shell nuclei with $A > 5$ $N_{12max} = N_{max} + 2$.

The two-body effective Hamiltonian in A- nucleon calculations is then

$$H^{\Omega}_{A,eff} = \sum_{i<j}^{A} h_i + \sum_{i<j}^{A} V_{2eff,ij} \tag{2.20}$$

At this point we also subtract the H_{CM}.

2.1.4 Computational resources to diagonalize sparse Hamiltonian matrix

It is very difficult to solve nuclear quantum many body problem computationally as it is large sparse matrix eigenvalue problem. In nuclear physics the nuclear interactions are very strong, many body and complex. Our main aim is to get converge results as much as possible to minimize the extrapolation uncertainties. For this, we have to do calculations in a large basis space. The dimensions of the Hamiltonian increase with increasing N_{max} and A. In Fig. 2.5, we see how the dimension explodes with increasing N_{max} and A. All nucleus are taken under condition for the natural parity basis space and this parity coincides with $N_{max} = 0\hbar\Omega$ configuration for that nucleus. The figure represent the limit of up to four-nucleon ($4N$) interactions (near in future). Although, we know the order of potentials is $NN > NNN > NNNN$, the four-nucleon potential is relatively less important than NNN and NN. Higher order potentials show their contributions with increasing number of nucleons. The memory required to store the non zero matrix elements for different nuclei corresponding to 2-body, 3-body and 4-body are shown in Table 2.1. Here, the notations GB (10^9 bytes), TB (10^{12} bytes), PB (10^{15} bytes) and EB (10^{18} bytes) correspond to Gigabytes, Terabytes, Petabytes and Exabytes, respectively. People are trying to solve the nuclear sparse matrix eigenvalue problem with greater efficiency. The main aim is to get the low energy spectra using Lanczos method in m-scheme of HO basis. Further developments are in progress to solve this computationally hard problem.

2.2 Lanczos Algorithm

When we are interested in only few eigen values and eigenstates, then for diagonalization Lanczos method [74] is employed. This method is a standard method for diagonalization. The most of diagonalization technique whose CPU time increases as N^3, where N is the dimension of the matrix can not be used in large basis space

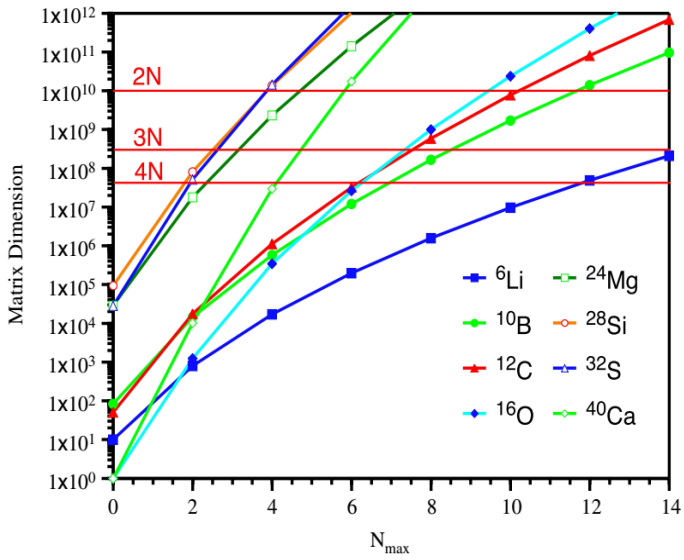

Figure 2.5: Matrix dimension for $N = Z$ nuclei with different N_{max} using $2N$, $3N$ and $4N$ interactions [9].

Table 2.1: Table for the required space to store the nonzero matrix elements corresponding to $2N$, $3N$ and $4N$ interactions for a given range of nuclei [9].

Nucleus	Dimension (N_{max})	$2N$	$3N$	$4N$
^{6}Li	4.9×10^{6} (12)	0.6 GB	33 TB	590 TB
^{12}C	6.0×10^{8} (8)	4 TB	180 TB	4 PB
^{12}C	7.8×10^{9} (10)	80 TB	5 PB	140 PB
^{16}O	9.9×10^{8} (8)	5 TB	300 TB	5 PB
^{16}O	2.4×10^{10} (10)	230 TB	12 PB	350 PB
^{8}He	4.3×10^{8} (12)	7 TB	300 TB	7 PB
^{11}Li	9.3×10^{8} (10)	11 TB	390 TB	10 PB
^{14}Be	2.8×10^{9} (8)	32 TB	1100 TB	28 PB
^{20}C	2×10^{11} (8)	2 PB	150 PB	6 EB
^{28}O	1×10^{11} (8)	1 PB	56 PB	2 EB

calculations. In Lanczos method we construct a orthogonal basis in which the Hamiltonian matrix H is tridiagonal. We start with a normalized vector which is called pivot state (Φ_1) is applied by the Hamiltonian operator and we get a parallel and an orthogonal components to this pivot vector.

$$H|\Phi_1\rangle = E_{11}|\Phi_1\rangle + E_{12}|\Phi_2\rangle, \tag{2.21}$$

where, $E_{11} = \langle\Phi_1|H|\Phi_1\rangle$ and $E_{12}|\Phi_2\rangle = H|\Phi_1\rangle - E_{11}|\Phi_1\rangle$. We again apply H on $|\Phi_2\rangle$, then a third state $|\Phi_3\rangle$ is created, which is orthogonal to $|\Phi_1\rangle$ and $|\Phi_2\rangle$.

$$H|\Phi_2\rangle = E_{21}|\Phi_1\rangle + E_{22}|\Phi_2\rangle + E_{23}|\Phi_3\rangle. \tag{2.22}$$

Here, $E_{21} = E_{12}$, because H matrix is real symmetric in our basis.

After n iteration, we get the form

$$H|\Phi_n\rangle = E_{nn-1}|\Phi_{n-1}\rangle + E_{nn}|\Phi_n\rangle + E_{nn+1}|\Phi_{n+1}\rangle, \tag{2.23}$$

$E_{nn-1} = E_{n-1n}$, $E_{nn} = \langle\Phi_n|H|\Phi_n\rangle$, and $E_{nn+1}|\Phi_{n+1}\rangle = H|\Phi_n\rangle - E_{nn}|\Phi_n\rangle - E_{nn-1}|\Phi_{n-1}\rangle$.

At each iteration the matrix is diagonalized and the iteration continues until we get all the converged eigenvalues. The computing time is directly proportional to number of matrix elements (in standard methods cubic dependence on the dimension of the matrix). For getting converged value, the choice of pivot state is very important.

The tridiagonal Lanczos matrix H_t in which the diagonal elements are denoted by a_i and subdiagonal and superdiagonal elements are denoted by b_{i+1}, is given as:

$$H_t = \begin{pmatrix} a_1 & b_2 & 0 & 0 & \dots \\ b_2 & a_2 & b_3 & 0 & \dots \\ 0 & b_3 & a_3 & b_4 & \dots \\ 0 & 0 & b_4 & a_4 & \dots \\ \dots & \dots & \dots & \dots & \dots \end{pmatrix} \tag{2.24}$$

2.3 pANTOINE

pANTOINE code (developed by B. D. Carlsson and coworkers) is an exact diagonalization code, based on NCSM version of ANTOINE (developed by Caurier and coworkers) [75–77]. Basically pANTOINE is an advanced version of ANTOINE code. For diagonalization, it uses Lanczos method to find eigenvalues and eigenvectors of a sparse and huge, Hermitian matrix. It uses the same factorization scheme as in BIGSTICK code [78]. Using pANTOINE code, for ^{6}Li, the NCSM calculations increased from $N_{max} = 18$ to 22 with NN interactions, where $N_{max} = 18$ was the previous computational limit [79, 80]. The model-space dimension is also increased from 2.7×10^9 to 2.5×10^{10}. This code runs on single shared-memory machines in a very efficient manner, although it needs large memory resources ($\geq$ 32 GB). The operation $y = Mx$ can be factorized into subsets: $y_i = (M_{i1}x_1 + M_{i2}x_2 + ...)$ to handle vectors which are much larger than the available memory [47]. In the case of NN interactions, this code creates the Hamiltonian matrix on the fly so the distribution of matrix elements over thousands of nodes is no longer needed. In Fig. 2.6, the results are shown on a single compute node [47]. The current version of code needs node local disk space for temporary storage. This code efficiently uses the local scratch space and carries out streaming of multi-100 MB/s reads while maintaining full CPU load of multicore

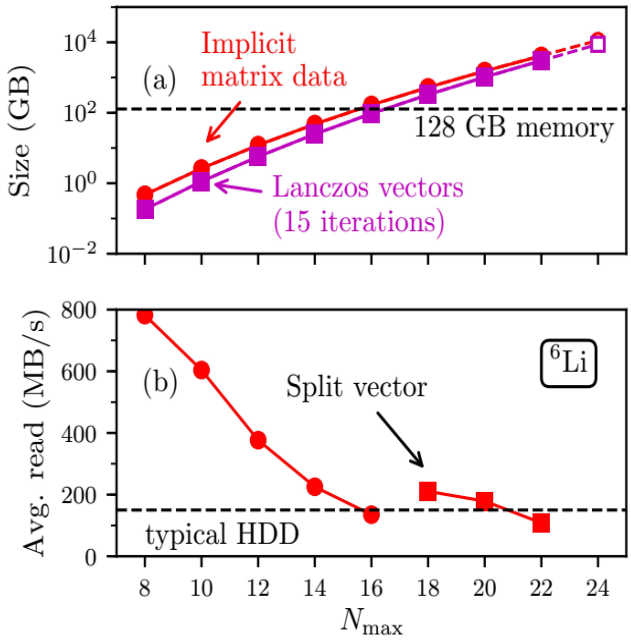

Figure 2.6: Plot for ^{6}Li as a function of model space size. (a) shows the storage needed for implicit matrix and Lanczos vectors. (b) shows the average speed of matrix data from disk [47].

matrix-vector when the size job exceeds the available memory.

In Fig. 2.6(a) the example for ^{6}Li is given. For storing the Hamiltonian matrix and Lanczos vectors, almost 10 TB of storage is needed. In the case of $N_{max} \geq 18$, the Lanczos vector is split in many blocks. With a split vector, mirror blocks are taken care separately causing multiple passes over the same implicit matrix data. The average read speed increases as more data is read in total, see Fig. 2.6 (b). The main advancements made in pANTOINE are given in Ref. [47].

The other popular code developed by IOWA group for NCSM calculations is Many Fermion Dynamics (MFDn) code [81] which is written in Fortran 90/95 based on MPI.

CHAPTER 3

NO CORE SHELL MODEL STUDY OF $^{18-23}$O AND $^{18-24}$F ISOTOPES

3.1 Introduction

Recent developments in computing power made possible to study the nuclei beyond p shell from NCSM approach [35,36,82]. The NCSM is a basic tool for explaining the nuclear structure and nuclear bound state problems, which uses nuclear interactions from the first principle. Now, the calculations are also available with the continuum effect in NCSM for explaining unbound states, scattering and nuclear reactions. Recently, NCSM calculations with continuum effect for ^{11}Be have been performed, the parity inversion problem is solved for ^{11}Be using NCSMC approach [83–85] with chiral interaction N^{2}LO$_{SAT}$ only [86]. *Ab initio* approaches give us opportunity to calculate more precisely the electromagnetic properties of exotic nuclei [87]. The NCSM calculations have various applications in nuclear structure as well as in nuclear reaction physics. New physics is coming out, e.g. N=8 magic number is no more magic number when we increase neutron and proton ratio. There is another

method which is named as no core shell model with core constructed for the heavier nuclei [9, 88]. To understand the details of fully open shell medium mass nuclei from first principle is still a challenge. Research for open shell nuclei is still going on using many *ab initio* approaches [20, 89]. The study of neutron rich nuclei from first principles is a interesting topic now a days. The exact location of drip-line in neutron rich oxygen isotopes can be explained using *ab initio* approaches using NN+3N(full) chiral interactions where role of $3N$ forces is very important [90]. Still it is very challenging to perform NCSM calculations for O and F chain. The NCSM with perturbation approach (NCSM-PT) results for low-lying states in $^{18-20}$O isotopes are reported in Ref. [89]. In the present chapter our aim is to study systematically the low-lying energy spectrum (positive parity) for oxygen ($^{18-23}$O) and fluorine ($^{19-24}$F) chain using *ab initio* NCSM. We have used inside nonlocal outside Yukawa (INOY) potential for NCSM calculations. In the present chapter we have also compared our NCSM results with phenomenological USDB effective interaction [91]. In the present chapter we have used the pANTOINE [47, 75, 76] shell model code which is adapted to NCSM [92].

3.2 Effective interactions and details of the calculations

In NCSM, as we increase model space size, solving many body problem become computationally hard. We want to do calculations with NN interactions in maximum model space size but do not want to loose the effects of three body forces. Previously, the INOY interaction is used in NCSM calculations to find the binding energies, excited states of both parities, electromagnetic moments, and point-nucleon radii in Be isotopes [87]. There are two reasons behind choosing INOY potential, first one is that it contains three body effect through nonlocality in some partial waves so we get the effect of three body forces also without adding three body forces explicitly

and the second reason is that we get fast convergence for INOY interaction for a given N_{max} $\hbar\Omega$ in comparison to any other interaction. The nonlocality and three body forces are deeply related to each other [93]. The INOY potential is a nonlocal potential in coordinate space. Actually it is a mixture of local and nonlocal parts, local Yukawa tail at longer ranges (> 3 fm) and nonlocal at short range. As we know that nucleons have a internal structure, because of this a nonlocality character comes at short range (up to 1-1.5 fm). The INOY NN interaction (set of $^1S_0$ and $^3SD_1$ NN interactions) is in coordinate space and it was constructed to see the effect on triton binding energy. When we use the coordinate space, it is easy to handle the ranges of local and nonlocal parts explicitly. In coordinate space, because of the basic property (short range nature) of NN interaction, it should vary as an exponential function at long ranges. The form of INOY NN interaction is given in chapter 2 and details are given in Refs. [8, 49]. Apart from INOY NN interaction, we have also used next-to-next-to-next leading order (N3LO) interaction which is derived from chiral effective field theory. The NCSM calculations are done with this interactions at $\hbar\Omega$=14 MeV. Previously, the NCSM calculations are done using N3LO NN interaction for ^{18}F up to N_{max}=4 [9]. In the present calculations we have reached up to N_{max}=6 in case of $^{18-21}$O and ^{18,19}F and the dimensions of the matrices which we have diagonalized for these isotopes are $\sim 10^8 - 10^9$. The calculations with next-to-next leading order (N2LOopt) interaction at $\hbar\Omega$=20 MeV have been also included, which is a bare interaction. In the bare interaction, OLS transformation is not used. In the present calculations, we also see the difference between the results using bare and all other interactions (N3LO, INOY and USDB). Please see chapter 2 for more details about NCSM formalism.

3.3 Results and discussions

We have performed the NCSM calculations for oxygen ($^{18-23}$O) and fluorine chain ($^{18-24}$F). As we know NCSM calculations are variational, depend on $\hbar\Omega$, and size of

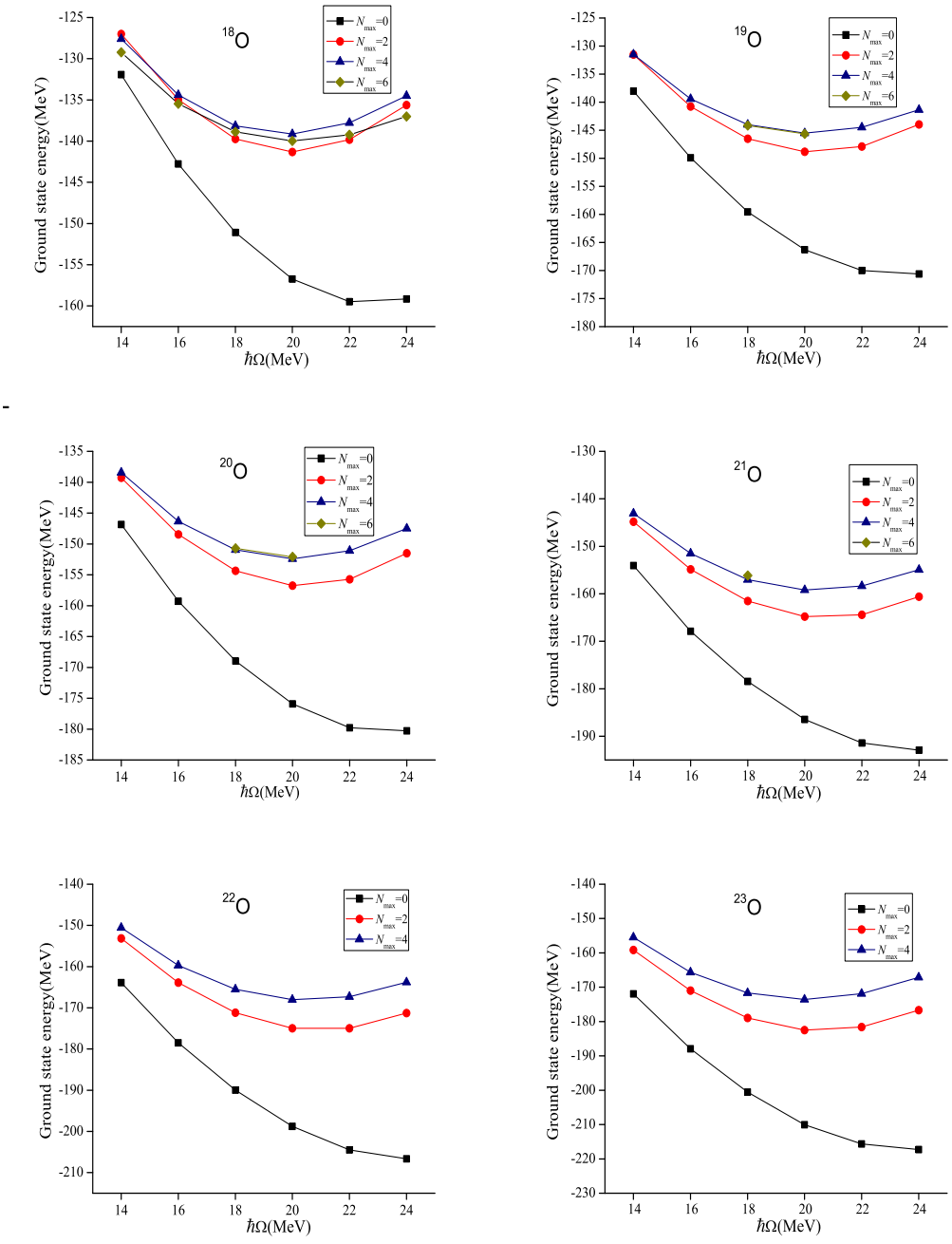

Figure 3.1: The variation of g.s. energy with different frequencies and model spaces for INOY interaction.

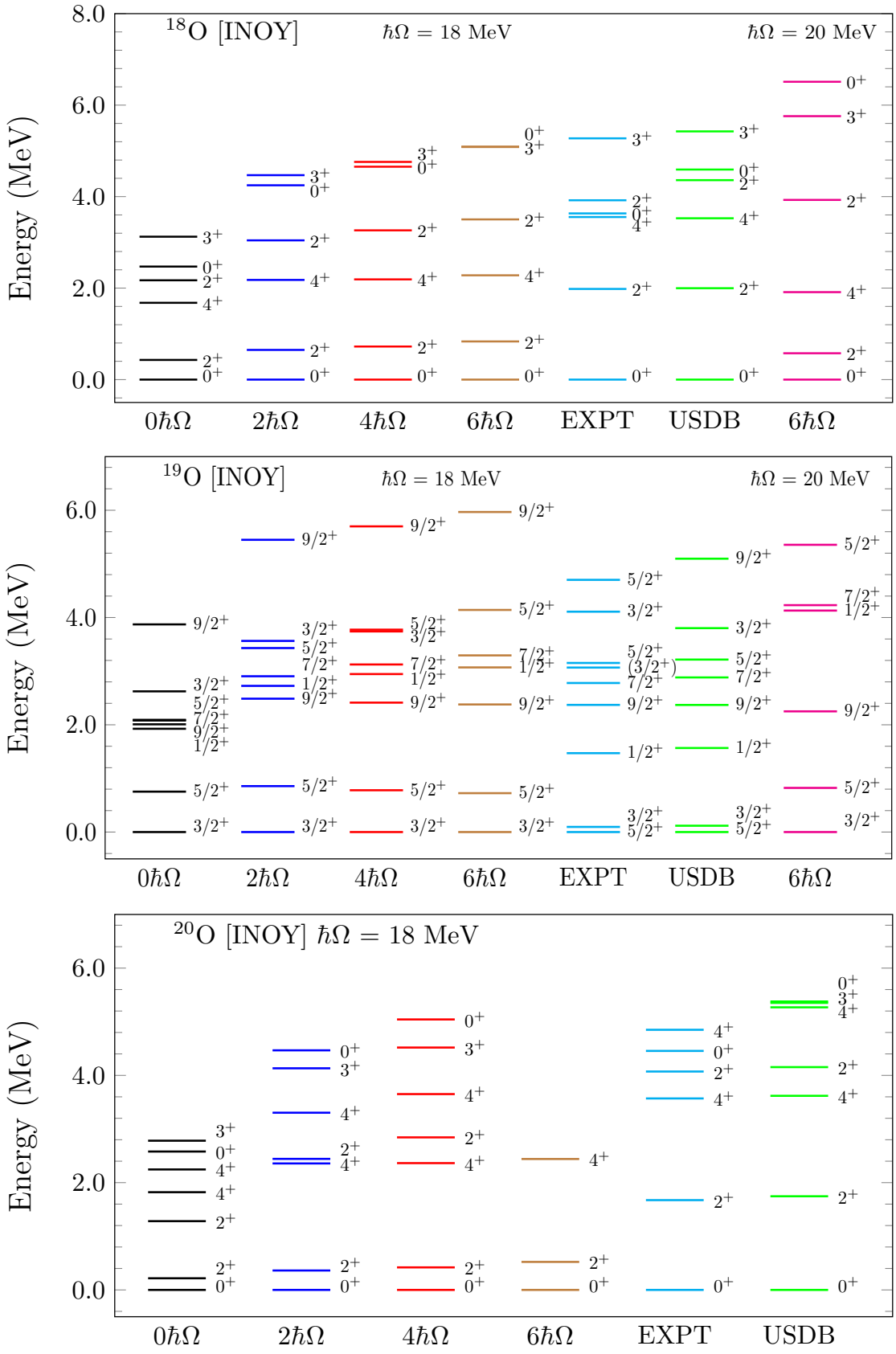

Figure 3.2: The energy spectra of $^{18-20}$O isotope with INOY and USDB interaction.

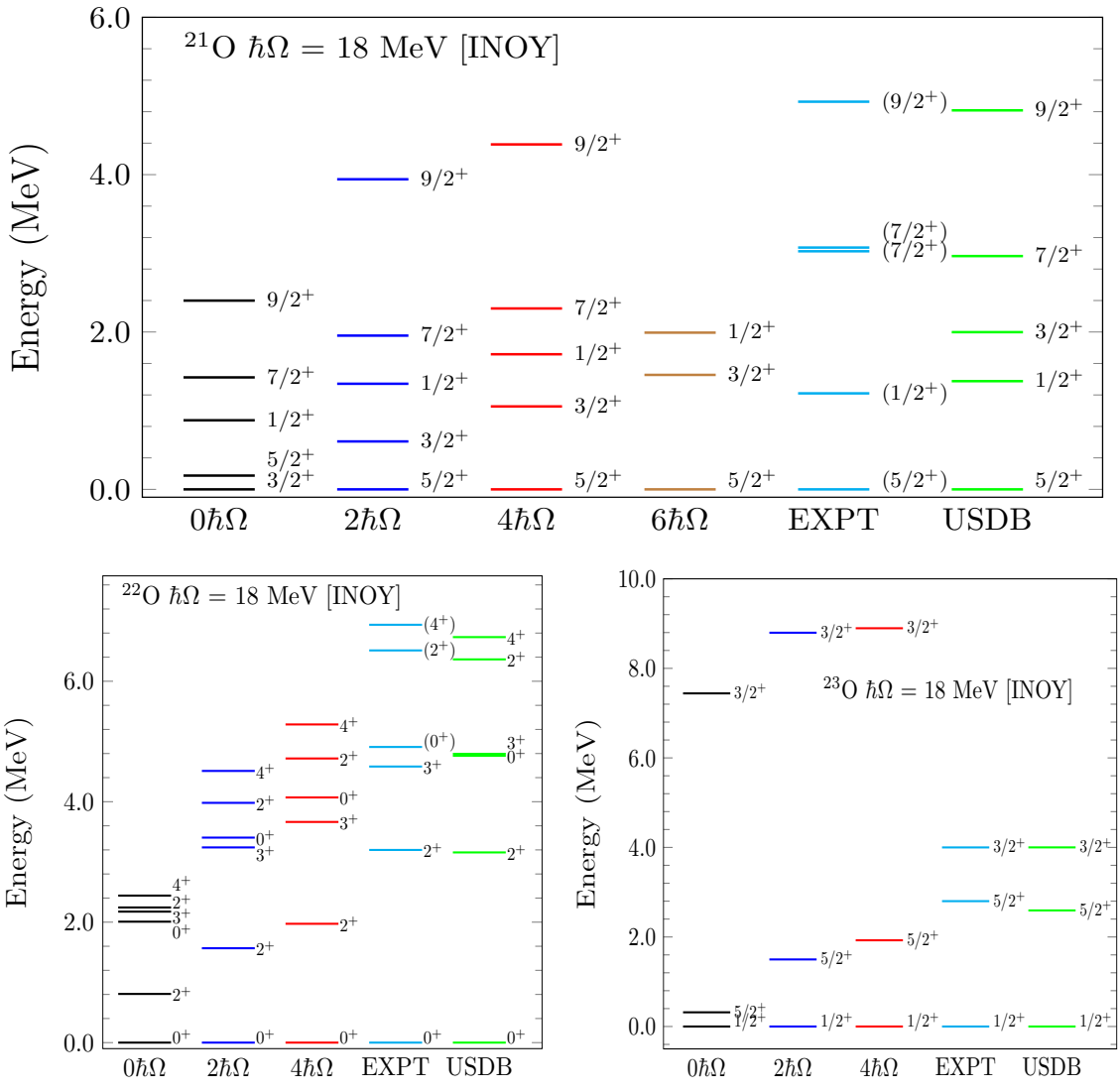

Figure 3.3: The energy spectra of $^{21-23}$O isotope with INOY and USDB interaction.

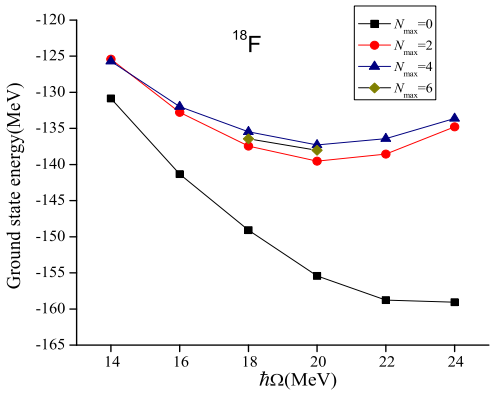

Figure 3.4: The variation of g.s. energy with different frequencies and model spaces for INOY interaction. Similarly for other F isotopes.

model space N_{max}. To see the dependence, first we do the calculations with different frequencies for a given N_{max}. We are interested to see that region in which the dependence of g.s. energy on frequency is minimum (for largest model space). We select that frequency for NCSM calculations. This procedure is called optimization of frequency. When we use this frequency, we get faster convergence rather than other values of frequencies. This is the benefit for doing optimization of frequency. We will see when we go for higher model space, the dependence on frequency decreases.

In Fig. 3.1 and 3.4, we have shown the variation of g.s. energies with the HO frequencies and different model space sizes. We can see the g.s. energy becomes less dependent when we move to higher N_{max}. We are getting a minima at $\hbar\Omega$=20 MeV. As we will go higher model space, we expect that this minima will shift at $\hbar\Omega$=18 MeV. We pick up the frequency 18 and 20 MeV for the calculating another properties like energy spectra, and occupancy. We have shown the energy spectra using different interactions for oxygen and fluorine chain in Figs. 3.2-3.3 and Figs. 3.5-3.8, respectively. We have also compared our NCSM results with phenomenological interaction USDB and experimental data [94]. Here, we will discuss the results corresponding to largest N_{max}.

In the case of ^{18}O, we can see as we move towards the higher N_{max} from 0 to 6,

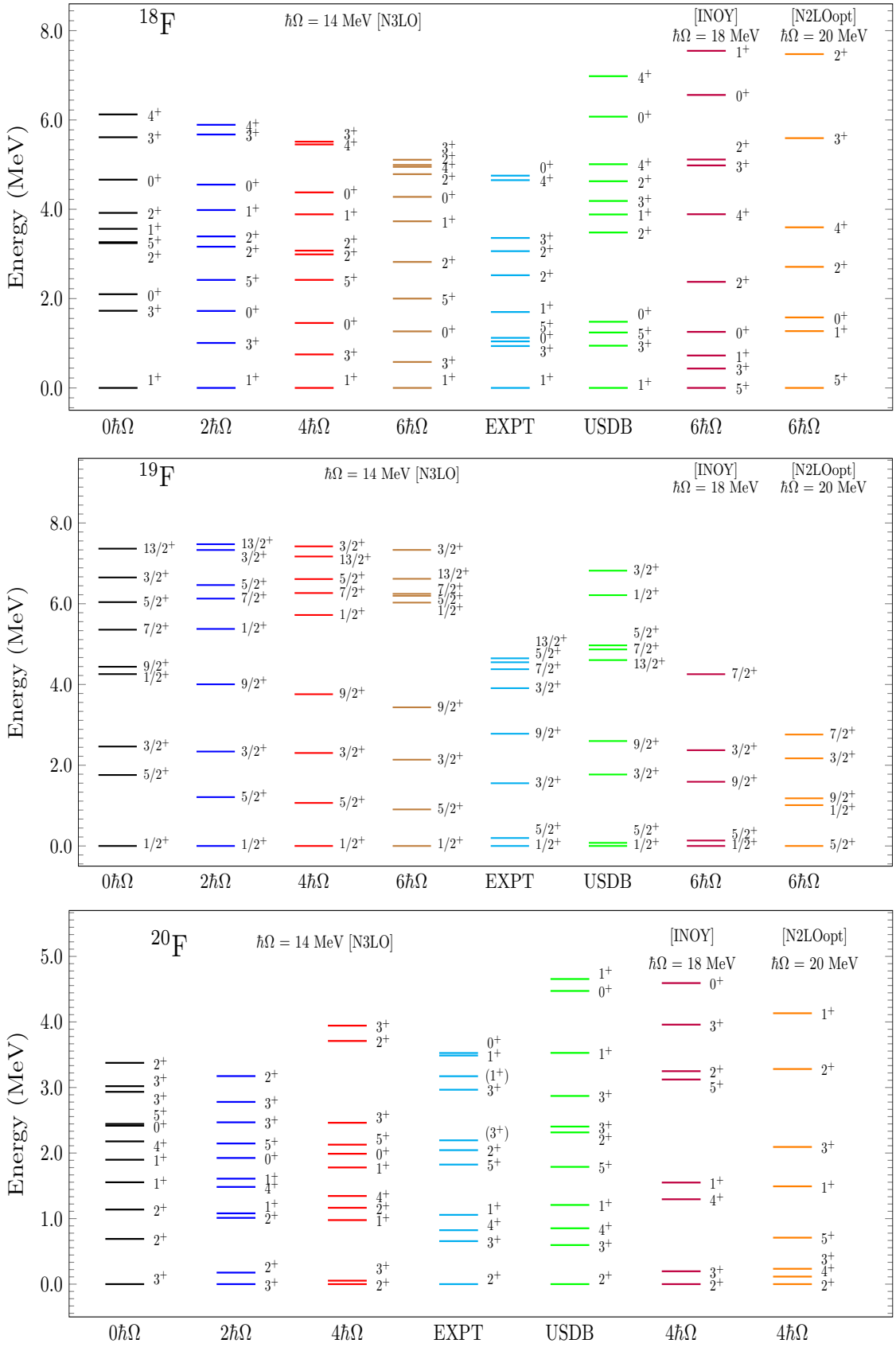

Figure 3.5: The energy spectra of $^{18-20}$F isotopes with N3LO, USDB, INOY and N2LOopt.

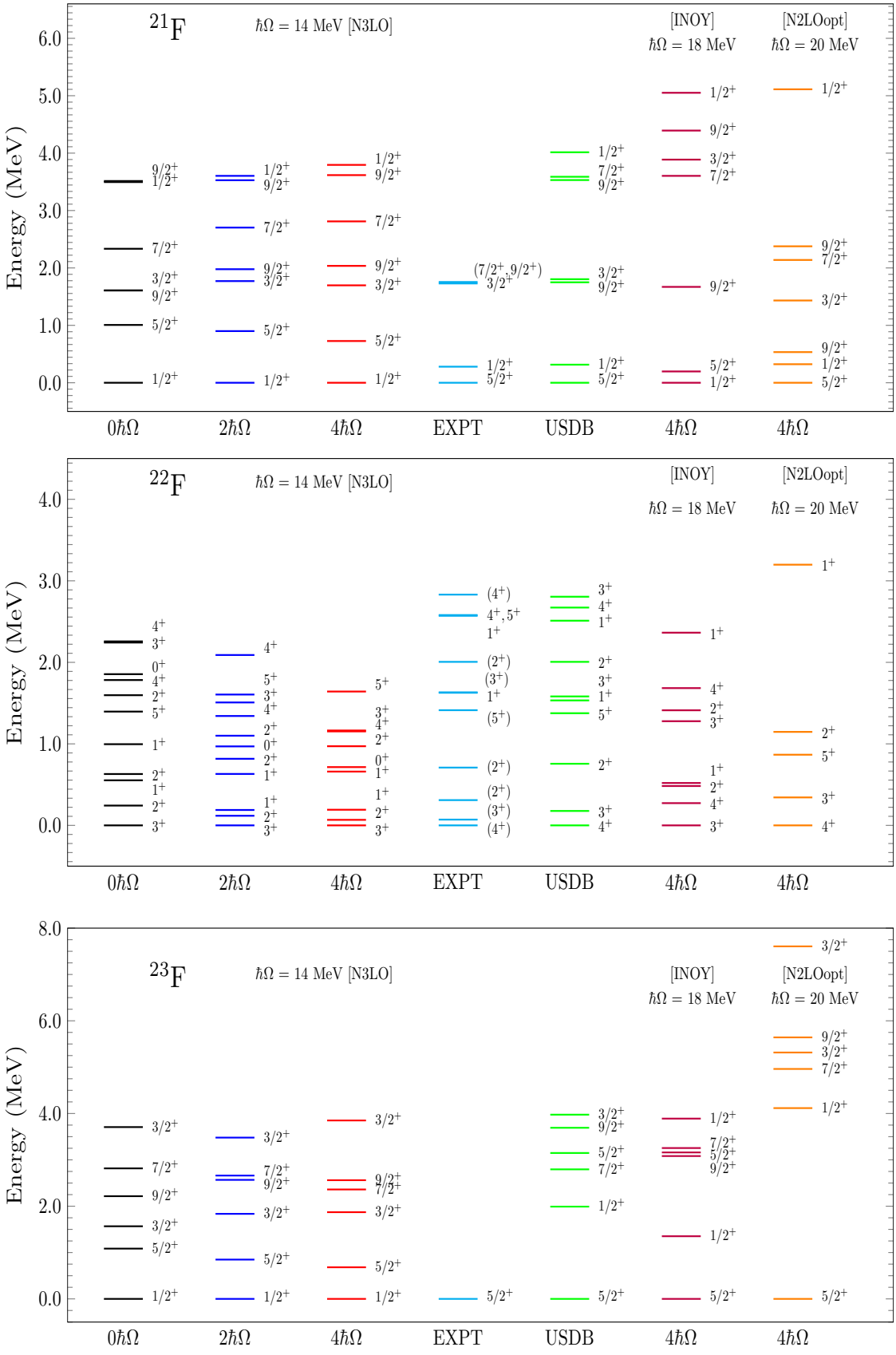

Figure 3.6: The energy spectra of $^{21-23}$F isotopes with N3LO, USDB, INOY and N2LOopt.

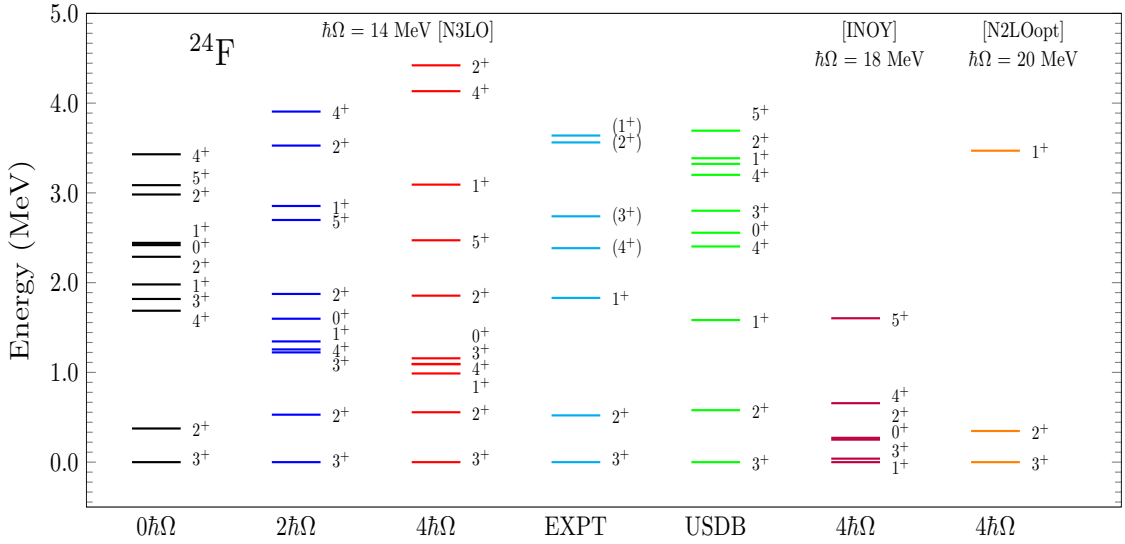

Figure 3.7: The energy spectra of ^{24}F isotope with N3LO, USDB, INOY and N2LOopt.

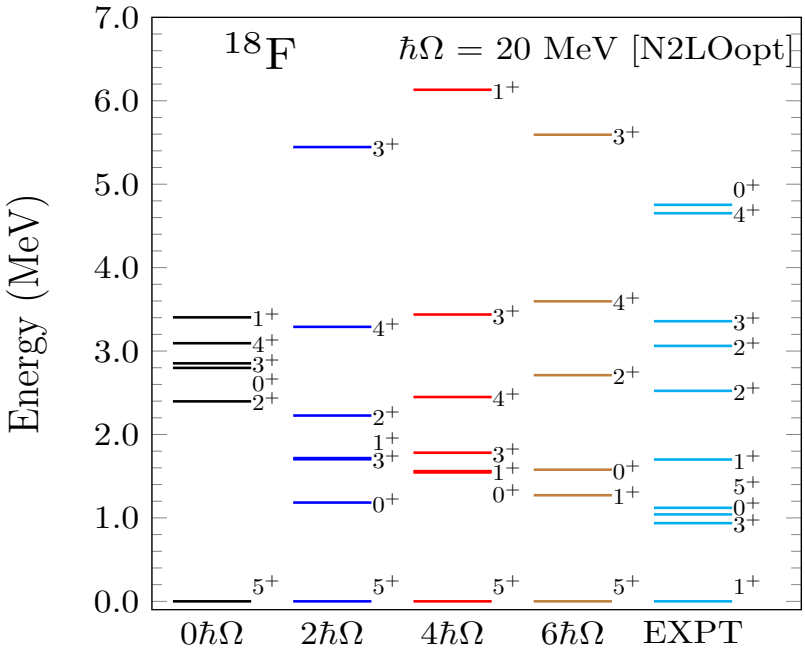

Figure 3.8: The energy spectra of ^{18}F with N2LOopt.

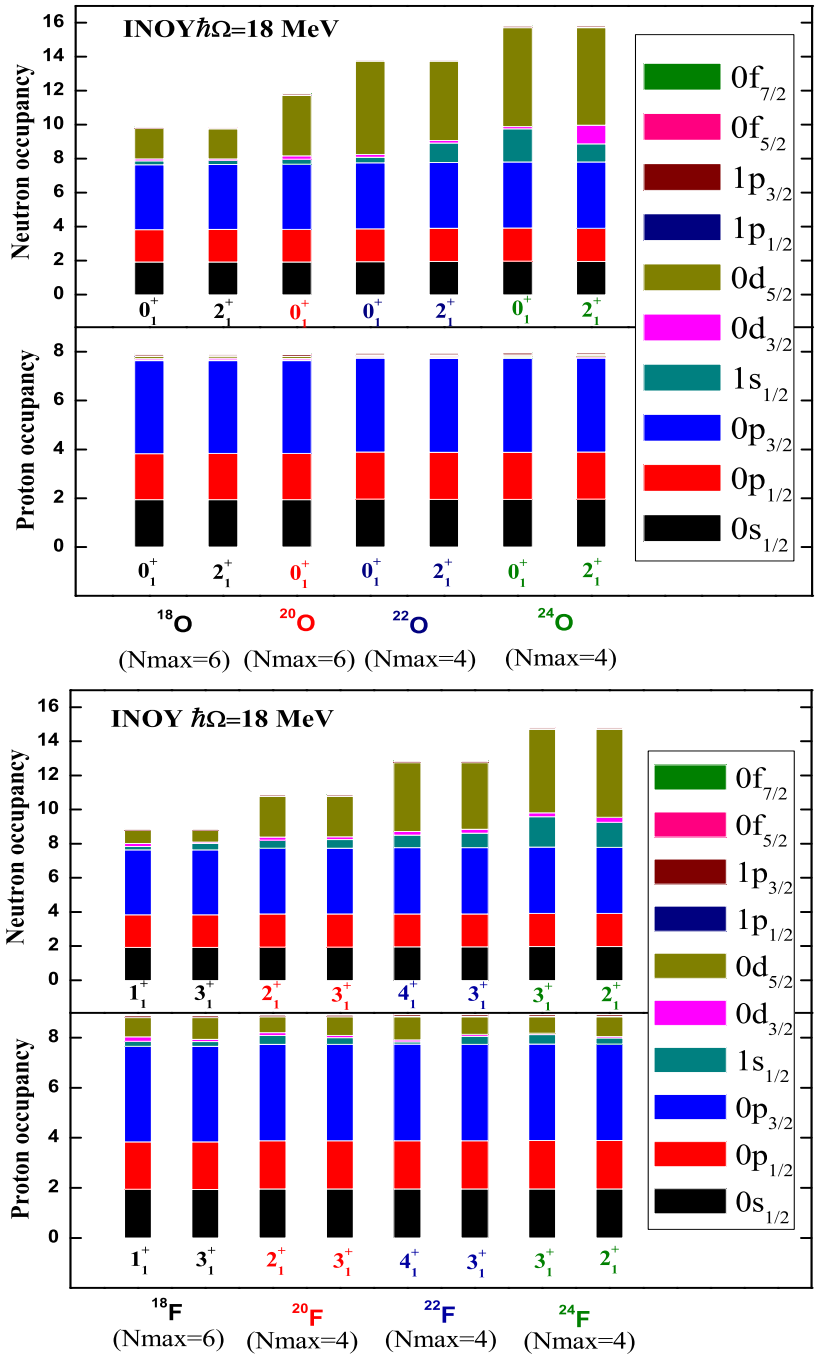

Figure 3.9: Systematics of occupation numbers for even O and F isotopes.

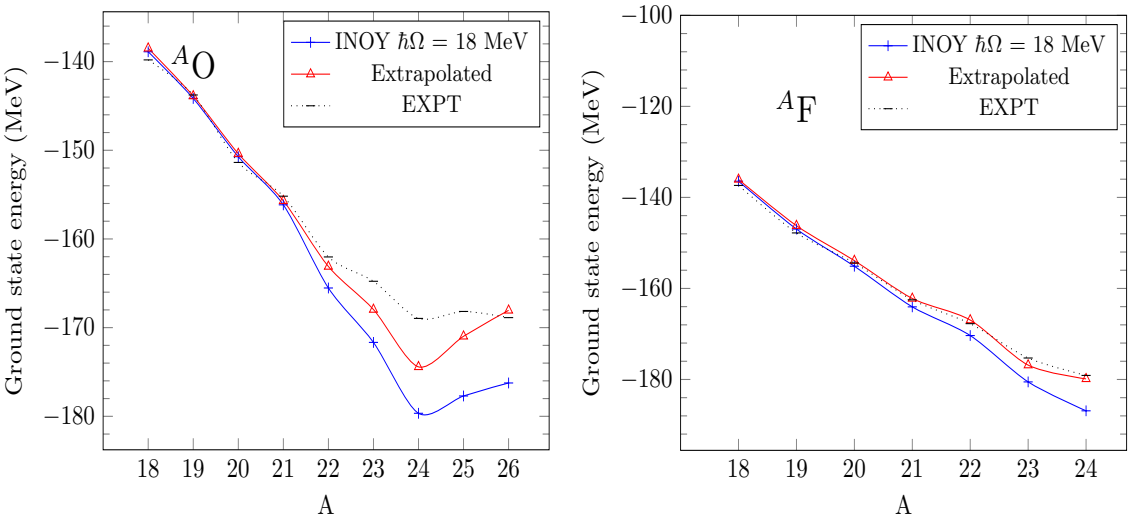

Figure 3.10: Ground state energies of O and F isotopes at $\hbar\Omega$ = 18 MeV. For $^{18-21}$O and ^{18,19}F, the g.s. energy corresponds to N_{max} = 6 and for rest isotopes corresponds to N_{max} = 4.

the calculated results also improve in comparison to lower N_{max} (however, 0_2^+ is at higher energy for N_{max}=6 in comparison with the lower N_{max}).

The gap between 0_1^+ and 2_1^+ increases smoothly as we move to higher N_{max}. The results with $\hbar\Omega$=18 MeV are better than with $\hbar\Omega$=20 MeV. At $\hbar\Omega$=18 MeV, the 2_1^+ and 4_1^+ states follow the same order but the 0_2^+ and 2_2^+ sates are in reverse order in comparison to the experimental data. This reverse order is also seen with USDB. In the case of ^{19}O, we are not getting the correct g.s. $5/2^+$ with both the frequencies. The $5/2^+$ state is at higher energy. The calculated $9/2^+$ state is near to the experimental $9/2^+$ state. The $1/2^+$ state is going far for N_{max}=6 in comparison with the lower N_{max} values. In case of ^{20}O, low-lying spectra is in correct order below energy ∼3.5 MeV for N_{max}=6. The 4_1^+ state is lower in energy in compared to experimental data. For ^{21}O, NCSM predicts g.s. $5/2^+$ (although it is tentative experimentally). For ^{22}O, we get slightly better results rather than previous oxygen isotopes. Here, the calculated states are in the same order as in the experimental data using NCSM calculations. The states 0_2^+ and 3_1^+ are in reverse order with USDB interaction. For ^{23}O, we get correct g.s. with the NCSM. The theoretical $5/2^+$ state

is reaching close to the experimental $5/2^+$ state with increasing model space size.

In the case of fluorine isotopes ($^{18-24}$F), we show the NCSM results using three interactions N3LO, INOY and N2LOopt at $\hbar\Omega$= 14 MeV, 18 MeV and 20 MeV, respectively.

For ^{18}F (see Fig. 3.5), we can see that the NCSM calculations using N3LO interaction are better than INOY and N2LOopt interaction. The N3LO interaction predicts correct g.s. 1^+ while INOY interaction and N2LOopt fails to predict correct g.s. The order of low lying states up to 5^+_1 is correct using N3LO interaction while other three interactions are not able to reproduce.

In case of ^{19}F, the $5/2^+_1$ state is close to the experimental data for INOY interaction and the order of $3/2^+_1$ and $9/2^+_1$ is reverse while for the N3LO interaction the $5/2^+_1$ state is at high in energy in comparison to the experimental data and it predicts the correct order of $3/2^+_1$ and $9/2^+_1$ states. N2LOopt interaction fails to reproduce the correct g.s. $1/2^+$. For ^{20}F, all the three interactions reproduces the correct g.s. 2^+. The NCSM results using INOY interaction are better in comparison to N3LO and N2LOopt. In the case of ^{21}F and ^{22}F the N2LOopt interaction reproduces the correct g.s $5/2^+$ and 4^+, respectively. In the case of ^{23}F, all the interactions give correct g.s. $5/2^+$ except N3LO. In the case of ^{24}F, the 3^+ and 1^+ states are very close using INOY interaction. With the N3LO interaction the 2^+_1 state is near to the experimental data. The 1^+_1 state is in low in energy with N3LO interaction while with INOY interaction it becomes the g.s. The N2LOopt interaction gives 1^+_1 state at very high energy. In the case of all fluorine isotopes we see the energy levels are more spread using INOY interaction in comparison with N3LO interaction. This is because of the strong **l.s** coupling in INOY interaction.

For better description we need to go to higher model space size. Fig. 3.9 shows the occupancies for the g.s. and first excited state in even oxygen and fluorine chain, respectively. We have shown the occupation numbers up to fp shell. Above the fp shell the occupation numbers are very small and very hard to visualize (in the present figure). So, we have not shown the orbitals beyond fp shell.

3.4 Location of drip-line in oxygen isotopes

As we know from the previous work in oxygen chain, the 3NF are needed to reproduce the drip-line at ^{24}O [90, 95, 96]. The calculations are done using chiral NN, $NN + NNN$-induced and $NN + NNN$-full interactions. The NN interaction shows the drip-line at ^{28}O [89,90,97]. In the present work we have applied INOY NN interaction which have effect of three body forces in terms of short range and nonlocality character present in it and it also reproduces the correct binding energy of triton. In the left panel of Fig. 3.10, we have shown the g.s. energies for oxygen isotopes using INOY at $\hbar\Omega$=18 MeV. We see the g.s. energy decreases as we reaches to ^{24}O but we see a kink after this. This shows the drip-line in oxygen isotopes at ^{24}O. The g.s. energy for fluorine isotopes is shown in the right panel of Fig. 3.10. Using INOY interaction the g.s energies are quite good up to ^{21}F.

3.5 Conclusions

In the present work first time we have reported NCSM results of oxygen and fluorine chain using INOY NN interaction [48]. We see how *ab initio* results improve with the increasing model space size. The INOY NN interaction is very important in the calculation because it gives the effect of three body forces without adding three body forces explicitly. NCSM calculations with INOY interaction also shows the correct drip-line at ^{24}O. We have calculated energy spectra for positive parity states and neutron and proton occupancies for the maximum reached N_{max} in our calculations.

CHAPTER 4

STUDY OF NEUTRON RICH NITROGEN ISOTOPES USING NO CORE SHELL MODEL

4.1 Introduction

At present NCSM is well established technique used in nuclear physics to calculate nuclear properties. Here, we solve A-body Schrödinger equation for the particles treated as non relativistically and interacted by realistic two plus three body forces. With the NCSM, a detailed study has been done for even carbon isotopes where g.s. energy, quadruple moment of 2_1^+ state, some $B(E2)$ transitions and occupancies of 0_1^+ and 2_1^+ are calculated [98] using INOY [8, 49] and CDB2K [7] interactions.

In the present chapter we will study the nitrogen isotopes and mainly focused on neutron rich side. The structure of neutron rich nuclei $^{19-22}$N has been studied by in-beam γ-ray spectroscopy and spectra and other properties are compared with shell model calculations using WBT and WBTM interactions, where $N = 14$ closed sub

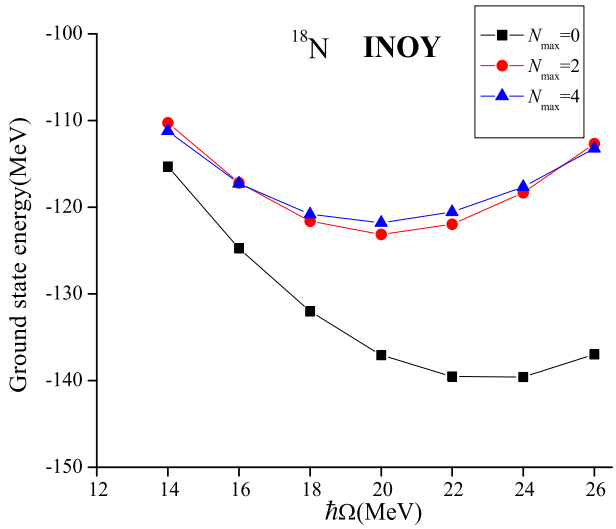

Figure 4.1: The variation of g.s. energy with different frequencies and different model space sizes.

shell is discussed [99]. The ^{22}N has halo structure in its g.s [100, 101]. Recently, the point proton radii of neutron rich $^{17-22}$N isotopes have been measured from charge changing cross section in Ref. [102].

The study of neutron rich nuclei is very important to know the behaviour of nuclear forces because many properties changed as we go away from the line of stability, like disappearance of traditional magic numbers and appearance of new magic numbers. The halo character also comes into picture when we go away from stability line [103]. Previously, the shell model calculations for nitrogen isotopes using full *psd* shell with WBT interaction of Warburton and Brown are reported in Ref. [99]. More recently, Yuan and Suzuki *et al.* have done systematic study of B to O isotopes with a interaction YSOX which include (0-3) $\hbar\Omega$ excitations [56] in full *psd* model space. To the best of our knowledge for the first time we have done systematic NCSM calculations for nitrogen isotopes.

For the NCSM calculations, we have used the pAntoine [47, 75] shell model code which is adapted to NCSM [92]. In the case of ^{22}N, for the largest model space N_{max}=

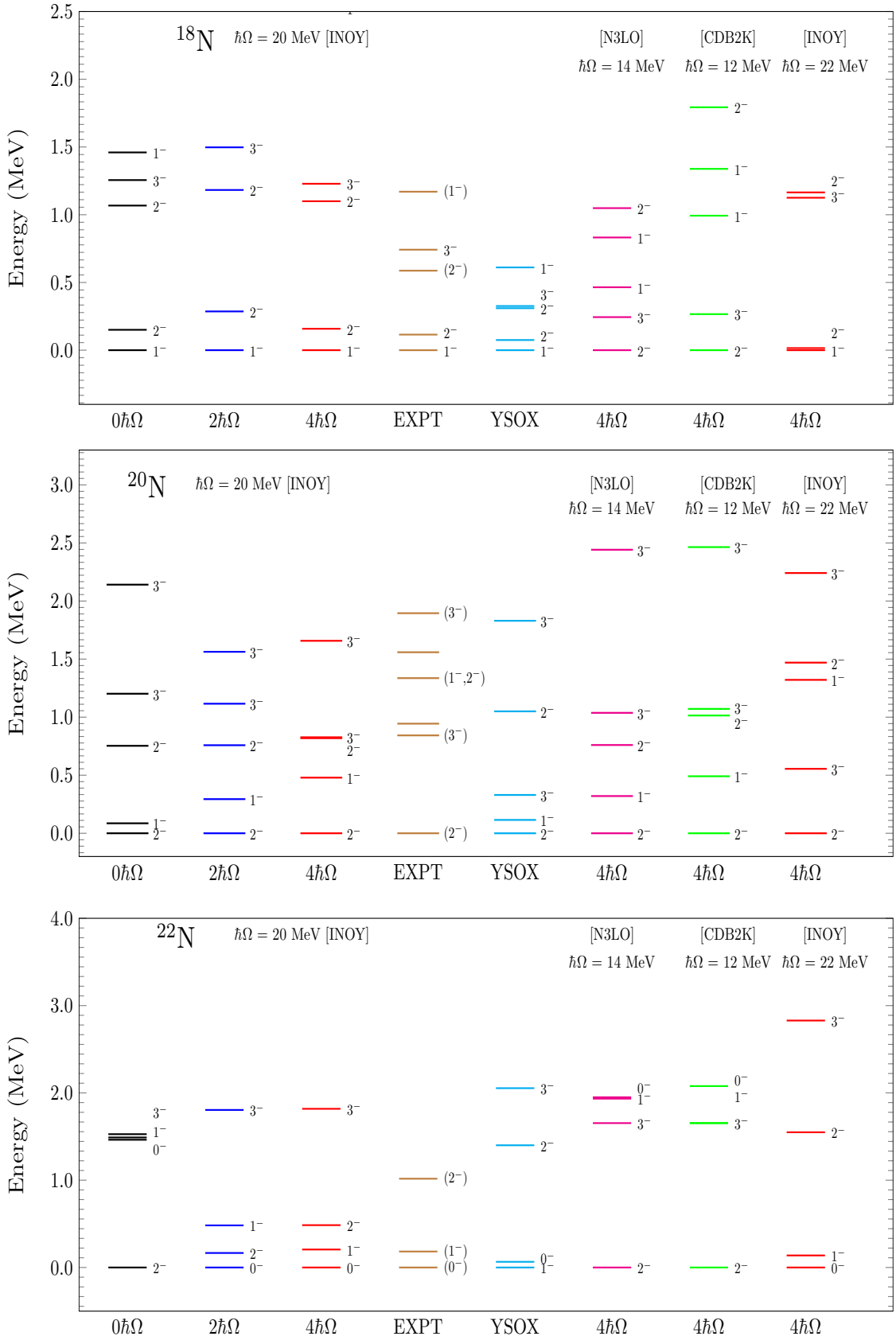

Figure 4.2: The energy spectra of ^{18,20,22}N nitrogen isotopes with different model space sizes. The experimental data is taken from Refs. [94, 104].

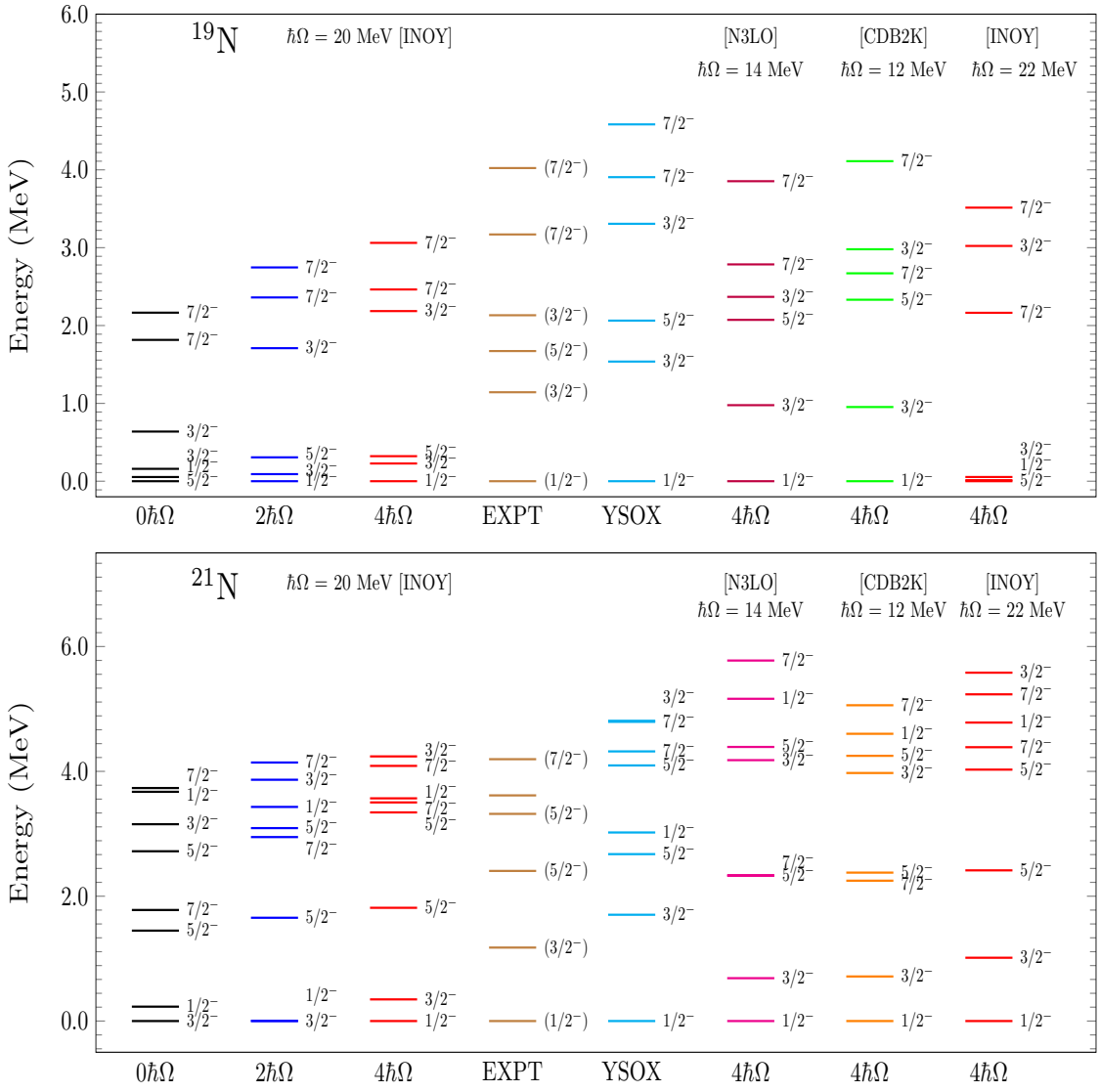

Figure 4.3: The energy spectra of ^{19,21}N nitrogen isotopes with different model space sizes. The experimental data is taken from Ref. [94].

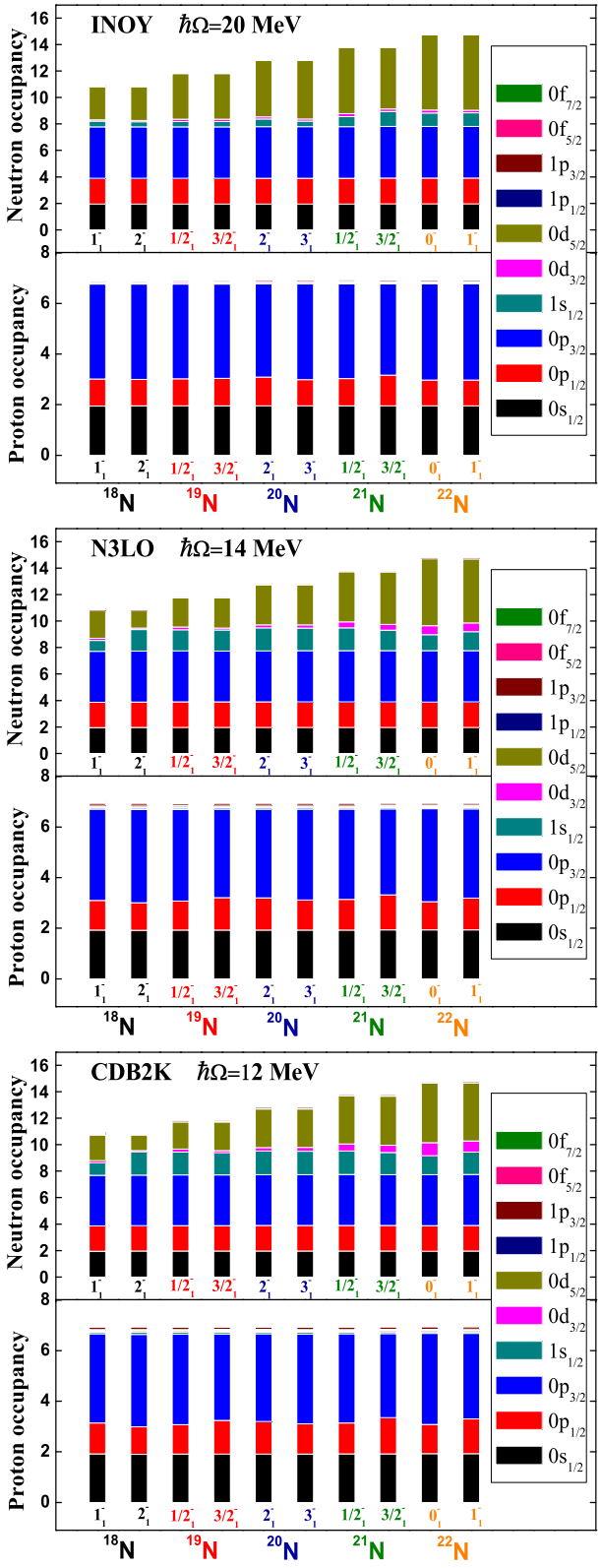

Figure 4.4: The occupancy of different orbits for nitrogen isotopes using INOY, N3LO and CDB2K interactions.

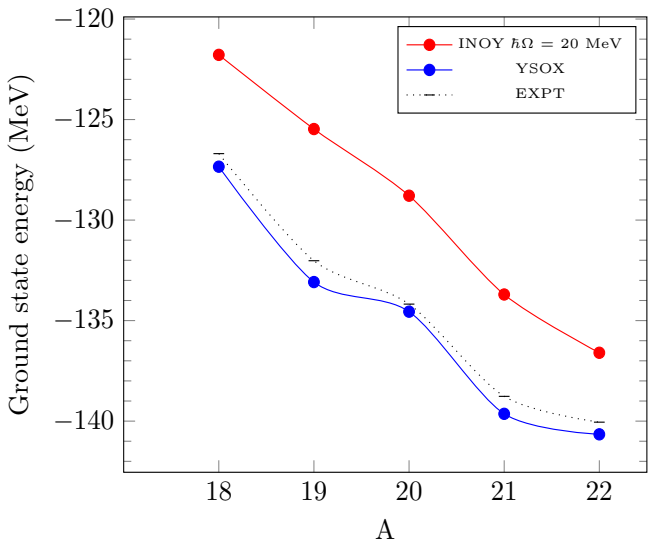

Figure 4.5: Comparison of calculated and experimental g.s. energies of N isotopes.

4, the corresponding dimension is $\sim 6.4 \times 10^7$. We have compared the NCSM results with the naive shell model calculations using YSOX interaction. For shell model calculations we have used KSHELL code [105].

4.2 Details of the calculations

In the present work we perform calculations for nitrogen isotopes. As we know NCSM calculations are variational, depend on HO frequency $\hbar\Omega$ and size of the model space N_{max}. To see this dependence, we have calculated the g.s. energy with different N_{max} and $\hbar\Omega$, see Fig. 4.1. We are interested to see that region in which the dependence of g.s. energy on frequency is minimum (for largest model space). We select that frequency for our NCSM calculations. This procedure is called optimization of frequency. When we use this frequency, we get faster convergence rather than other values of frequencies. This is the benefit for doing optimization of frequency. So, we have done our calculations with frequency $\hbar\Omega$= 20 MeV. For the other interactions we have chosen the frequency from the literature which is suitable

in this mass region. We have chosen the frequency $\hbar\Omega$=20 MeV for INOY and $\hbar\Omega$=14 MeV for N3LO interaction [9]. In the case of CDB2K, we have taken $\hbar\Omega$=12 MeV [98].

4.3 Results and discussions

We have studied the neutron rich nitrogen isotopes with the three different NN interactions: INOY, CDB2K and N3LO [6, 50, 106]. We have done calculations using INOY at $\hbar\Omega$= 20 MeV, CDB2K and N3LO interactions at 12 and 14 MeV, respectively. We have also compared our INOY results at $\hbar\Omega$= 22 MeV. The energy spectra are shown in Figs. 4.2 and 4.3. In the case of ^{18}N, the g.s. is correctly reproduced by INOY NN and YSOX interaction, while other two interactions give 2^- as a g.s. The order of energy states are correct with the INOY ($\hbar\Omega$=20 MeV) and YSOX only. The calculated 1_2^- state is at higher energy ($>$ 2.5 MeV) with INOY interaction (except for $N_{max} = 0$). The NCSM results for $N_{max} = 4$ with INOY ($\hbar\Omega$=22 MeV) are compressed in comparison to the CDB2K interaction.

For ^{20}N, the results with the INOY ($\hbar\Omega$=22 MeV) interaction are better than other interactions. Although the g.s. is correctly reproduced by all the three interactions but the higher states are not in agreement with the N3LO and CDB2K interactions. The first 3^- state is close to the experimental data with INOY ($\hbar\Omega$=20 MeV) and 1^- is close to experimental data with INOY ($\hbar\Omega$=22 MeV).

In the case of ^{22}N, only INOY interaction can reproduce the correct g.s. 0^- and level ordering with both the frequencies. All the other interactions are not able to produce correct g.s. and level ordering of the energy states.

In the case of ^{19}N, INOY ($\hbar\Omega$=20 MeV) and the other interactions reproduce the correct g.s. $1/2^-$, though, all the states are not yet been confirmed experimentally. The g.s. and first two excited states are very compressed with the INOY at both the frequencies in comparison to the other interactions. The N3LO interaction gives the energy states better and level ordering is correct with the experimental one. Overall the INOY interaction gives compressed energy levels.

Table 4.1: The g.s. energies (in MeV) for nitrogen isotopes using YSOX, INOY ($\hbar\Omega$=20 MeV), N3LO ($\hbar\Omega$=14 MeV), and CDB2K ($\hbar\Omega$=12 MeV) interactions.

Nucleus	EXP	YSOX	INOY	N3LO	CDB2K
^{18}N	-126.695	-127.344	-121.782	-112.036	-102.979
^{19}N	-132.025	-133.083	-125.471	-117.084	-107.616
^{20}N	-134.180	-134.556	-128.788	-119.857	-109.921
^{21}N	-138.768	-139.637	-133.702	-124.769	-114.278
^{22}N	-140.052	-140.657	-136.560	-127.114	-116.052

For ^{21}N, the g.s. is correctly reproduced. Higher states are not yet been confirmed experimentally. All the interactions give first excited state as $3/2^-$. Similarly, the second excited state seems to be $5/2^-$. For higher states, we are not sure for spin prediction. So, from our NCSM calculations it is clear that INOY interaction which has the effect of three body forces is suitable to study the neutron rich nitrogen isotopes. The inclusion of 3N forces is important to reproduce correct spectra with CDB2K and N3LO interactions.

In Fig. 4.4, we have shown the occupancy of first two states of nitrogen isotopes with the INOY ($\hbar\Omega$=20 MeV), CDB2K, and N3LO interactions correspond to N_{max}= 4 model space size. For N_{max}= 4, we have taken 28 orbitals. Here, we have shown the occupancy up to fp space because the occupancy of higher orbitals are very small to visualize. Although, the magnitudes of occupancies of higher orbitals are very small, still they are important in the calculation. The contribution of neutron occupancy from $0d_{3/2}$ and $1s_{1/2}$ orbitals for CDB2K and N3LO interaction is larger in comparison to INOY interaction. This larger occupancy is also reflected in the energy spectra. The CDB2K and N3LO results are similar for the g.s. spin and first excited state, however the occupancies for INOY interaction is different and for this interaction we are getting results which differ from other two interactions. In Fig. 4.5, the calculated g.s. energy for $^{18-22}$N isotopes using INOY and YSOX interactions follow the same trend as the experimental data. The g.s. energy for nitrogen isotopes with the other interactions are given in the Table 4.1 in which results with N3LO

and CDB2K are very far from the experimental data. If we go to higher N_{max}, the results will come closer to the experimental g.s. energies.

4.4 Conclusions

In the present work, we have performed NCSM calculations with different interactions (INOY, N3LO and CDB2K) for neutron rich nitrogen isotopes [55]. We have also compared our NCSM results with recently developed YSOX interaction for *psd* space from the Tokyo group. We have drawn following broad conclusions:

- In ^{18}N, the INOY and YSOX interaction predict second excited state as 2^-.
- For ^{20}N, the results of INOY ($\hbar\Omega$=22) interaction are much better than YSOX interaction.
- For ^{22}N, the INOY results for g.s. and first excited states are better than YSOX interaction. The N3LO and CDB2K interactions are unable to predict correct g.s.
- For ^{19}N, the NCSM results with N3LO are much better.
- In the case of ^{21}N, the INOY results ($\hbar\Omega$=22) are near to the experimental data.

CHAPTER 5

FIRST-PRINCIPLES RESULTS FOR ELECTROMAGNETIC PROPERTIES OF SD SHELL NUCLEI

5.1 Introduction

The study of atomic nuclei using first principles is an important topic in nuclear structure physics. The anomalous behavior for nuclei close to the drip-line can now be explained using *ab initio* approaches. The inclusion of three-body forces was found to be crucial for explaining the exact location of the drip-line for oxygen and calcium isotopes [107, 108]. Although *ab initio* calculations are difficult for heavier nuclei, recently spectroscopy of *sd* shell nuclei using different *ab initio* approaches has been reported in the literature. Using the in-medium similarity renormalization group (IM-SRG) approach, *ab initio* predictions for the g.s. and excited states of doubly open-shell *sd* nuclei have been reported in Ref. [20]. Also *ab initio* coupled-cluster effective interaction (CCEI) was derived and used to calculate the levels in p and *sd*

shell nuclei successfully [11,12,19]. A mass-dependent effective Hamiltonian in a $0\hbar\Omega$ model space for the *sd* shell nuclei, starting from a no core shell model Hamiltonian in a $4\hbar\Omega$ model space with the realistic J-matrix Inverse Scattering Potential, fitted to nuclei with masses up to A = 16 (JISP16) and chiral N3LO NN interactions, has been reported in Ref. [88]. The recent experimental results of ^{24}F have been theoretically interpreted with IM-SRG in Ref. [109] and a coupled-cluster interpretation has been presented for recently populated levels in ^{25}F [110]. In all these papers, the focus was on the spectroscopy of *p* and *sd* shell nuclei.

In the present chapter, our motivation is to test the *ab initio* Hamiltonians derived from the two approaches, IM-SRG and CCEI, by calculating electromagnetic properties of *sd* shell nuclei. The results of this work will add to the earlier studies in Refs. [11, 12, 20, 88], where only spectroscopic properties (spins, parities, and level energies) of these nuclei were reported. We compare our results to the available experimental data as well as with the calculations using the phenomenological USDB shell model interaction [91].

5.2 Details on *ab initio* calculations

In this work, we have performed shell model calculations for which the valence-space Hamiltonian was derived using two modern *ab initio* approaches: IM-SRG [20] and CCEI [11]. We have also compared the results with calculations using the phenomenological USDB effective interaction [91]. For the diagonalization of the matrices we have used the shell model code NUSHELLX [111].

5.2.1 IM-SRG

Stroberg et al. [20] derived a mass-dependent Hamiltonian for *sd* shell nuclei by using the IM-SRG [13] based on chiral two- and three-nucleon interactions. In this method, an initial Hamiltonian H, which is normal ordered with respect to a finite-density

reference state $|\Phi\rangle$ (e.g., the Hartree-Fock g.s.) is given as:

$$H = E_0 + \sum_{ij} f_{ij}\{a_i^\dagger a_j\} + \frac{1}{2!^2}\sum_{ijkl}\Gamma_{ijkl}\{a_i^\dagger a_j^\dagger a_l a_k\} + \frac{1}{3!^2}\sum_{ijklmn} W_{ijklmn}\{a_i^\dagger a_j^\dagger a_k^\dagger a_n a_m a_l\}, \quad (5.1)$$

where, $E_0, f_{ij}, \Gamma_{ijkl}$ and W_{ijklmn} are the normal ordered zero-, one-, two-, and three-body terms, respectively [112]. The normal ordered strings of creation and annihilation operators obey $\langle\Phi|\{a_i^\dagger \ldots a_j\}|\Phi\rangle = 0$. Now, a continuous unitary transformation is applied to the Hamiltonian of Eq. 5.1. This unitary transformation is parameterized by a parameter s which is called flow parameter:

$$H(s) = U(s)HU^\dagger(s) \equiv H^d(s) + H^{od}(s). \quad (5.2)$$

Here, $H^d(s)$ is the diagonal part and $H^{od}(s)$ is the off-diagonal part of the Hamiltonian. As $s \to \infty$, the off-diagonal matrix elements become zero.

The evolution of Hamiltonian with the flow parameter s is given as:

$$\frac{dH(s)}{ds} = [\eta(s), H(s)], \quad (5.3)$$

where $\eta(s)$ is the anti-Hermitian generator of the unitary transformation given by

$$\eta(s) \equiv \frac{dU(s)}{ds}U^\dagger(s). \quad (5.4)$$

The $H^{od}(s)$ permits us to decouple the *sd* valence space from the core and higher shells as $s \to \infty$. The resulting Hamiltonian is used in the shell model calculations. In the present calculations, we use the effective interactions with $\hbar\Omega$=24 MeV.

5.2.2 CCEI

For the Hamiltonian of the CCEI approach, we have used the following A-dependent Hamiltonian as a starting point:

$$\hat{H}_A = \sum_{i<j} \left(\frac{(\mathbf{p}_i - \mathbf{p}_j)^2}{2mA} + \hat{V}_{NN}^{(i,j)} \right) + \sum_{i<j<k} \hat{V}_{\rm 3N}^{(i,j,k)}. \tag{5.5}$$

The NN and $3N$ parts are taken from a N3LO chiral nucleon-nucleon interaction, and a N2LO chiral three-body interaction, respectively.

For both IM-SRG and CCEI, we use Λ_{NN}= 500 MeV for the chiral N3LO NN interaction [6, 50], and Λ_{3N}= 400 MeV for the chiral N2LO $3N$ interaction [113].

One can perform a unitary transformation of the Hamiltonian (5.5) to obtain the Hamiltonian used for the actual shell model calculations in the CCEI approach:

$$H^A_{CCEI} = H_0^{A_c} + H_1^{A_c+1} + H_2^{A_c+2} + \dots . \tag{5.6}$$

Here, the first term $H_0^{A_c}$ stands for the core, the second term $H_1^{A_c+1}$ for the valence one-body, and $H_2^{A_c+2}$ for the two- body Hamiltonian. The two-body term is derived from (5.5) by using OLS similarity transformation [53, 114]. By applying this unitary transformation, we get a non-Hermitian effective Hamiltonian. The similarity transformation is determined from the metric operator $[S^\dagger S]= P_2(1 + \omega^\dagger\omega)P_2$ (see Ref. [115] for further details). Here, for making the Hamiltonian Hermitian, the metric operator $S^\dagger S$ is used. The Hermitian shell model Hamiltonian is then obtained as $[S^\dagger S]^{1/2}\, \hat{H}^A_{CCEI}\, [S^\dagger S]^{-1/2}$.

In the present chapter, the two-body matrix elements for IM-SRG and CCEI *ab initio* approaches have been adopted from Refs. [20] and [11], respectively.

Finally, we have also compared our *ab initio* results with the shell model calculations using the phenomenological USDB interaction. The USDB interaction is fitted to two-body matrix elements [91], originally derived from a G-matrix approach. This interaction is fitted by varying 56 linear combinations of two-body matrix elements.

The shell model code NUSHELLX@MSU is a set of wrapper codes written by Brown. It uses a proton-neutron basis. With this code, it is possible to diagonalize J-scheme matrix dimensions up to $\sim$ 100 million.

5.3 Results and discussions

The magnetic dipole moment is defined as the expectation value of the dipole operator in the state with maximum M projection as

$$\mu = \langle J; M = J \mid \sum_i g_l(i) l_{z,i} + \sum_i g_s(i) s_{z,i} \mid J; M = J \rangle. \tag{5.7}$$

Here, g_l and g_s are the orbital and spin gyromagnetic ratios, respectively. By applying the Wigner-Eckart theorem,

$$\mu = \frac{J}{[J(J+1)(2J+1)]^{1/2}} \times \langle J \mid\mid \sum_i g_l(i)\mathbf{j_i} + [g_s(i) - g_l(i)]\mathbf{s_i} \mid\mid J \rangle. \tag{5.8}$$

The spectroscopic quadrupole moment (Q_s) is defined as

$$Q_s(J) = \langle J, m = J \mid Q_2^0 \mid J, m = J \rangle$$

$$= \sqrt{\frac{J(2J-1)}{(2J+1)(2J+3)(J+1)}} \langle J \mid\mid Q \mid\mid J \rangle. \tag{5.9}$$

We have used the harmonic-oscillator parameter $\hbar\Omega = 45A^{-1/3} - 25A^{-2/3}$ MeV for all the three calculations. The calculated values of the electromagnetic properties of *sd* shell nuclei with $e_p = 1.5e$, $e_n = 0.5e$, and $g_s^{eff} = g_s^{free}$ using the two *ab initio* interactions as well as the phenomenological USDB shell model interaction in the *sd* model space, along with the experimental data, are shown in the Tables 5.1 and 5.2. In Ref. [116], the suitable values of g factors and effective charges for *sd* shell

nuclei are given. However, in the present work, we have compared magnetic and quadrupole moments with two *ab initio* effective interactions along with phenomenological USDB effective interaction using free-nucleon g factors and standard values of effective charges in our calculations. The magnetic moments have been taken from Ref. [117] and more recent data were obtained from a compilation maintained by Mertzimekis under the IAEA auspices [118]. Recently, the experimental quadrupole moments for *sd* shell nuclei have been evaluated and the recommended values were presented in Ref. [119] along with shell model calculations using the USD and SDPF-U interactions. We have used these experimental quadrupole moments in Table 5.2. The values not available in this evaluation are taken from the specified references.

The experimental static and dynamic moments for Ne, Na, Mg and Al isotopes up to 20 neutrons, at the borders of (or inside) the island of inversion, are reported in Refs. [120–134]. For explaining the intruder configuration of neutron-rich nuclei ($\sim N = 20$), we need the $sd - pf$ model space. Using the SDPF-U-MIX effective interaction in the Ref. [135], it was shown the island of inversion region emerges around $N = 20$ and $N = 28$ for Ne to Al isotopes. The island of inversion is also known as island of deformation, which is due to nucleon-nucleon correlations. Because of the correlation energy, we get a deformed ground-state band and the spherical mean field breaks. The normal-order filling of orbits in the case of island of inversion candidates (^{30}Na, ^{31}Na, ^{31}Mg, and ^{33}Al) vanishes, where ^{33}Al is found to be at the border of the island of inversion [134]. The IM-SRG and CCEI *ab initio* effective interactions contain excitations of particles within different shells ($\sim$ 13 oscillator major shells), projected to a particular *sd* model space. The static and transitional quadrupole moments of nuclei lying in the island of inversion region show a drastic enhancement of quadrupole collectivity compared to neighboring nuclei. This has been attributed to a combination of a reduction in the $N = 20$ shell gap due to the tensor part of the nucleon-nucleon monopole interaction and enhanced quadrupole correlations induced by neutron excitations across this reduced shell gap. The moments of these isotopes have been very well described using the phenomenological shell model interactions in

an enhanced *sd-pf* model space where such neutron excitations are included, as illustrated e.g. in Refs. [126, 129, 134, 136]. The spectroscopy of other *sd* shell isotopes, including their moments, has been very well described by shell model calculations in the *sd* valence space using the phenomenological effective interactions, such as USDB [116]. However, the recent *ab initio* calculations reproduce also very well the spectroscopy of these *sd* shell isotopes, even improving an accurate description of their structure. It will be interesting to see how well they reproduce the ground-state static and dynamic moments.

For the oxygen isotopes, the calculated values of the magnetic moments with IM-SRG and CCEI show almost similar results. We have reported the magnetic moments for $^{17-20}$O and quadrupole moments for $^{17-19}$O isotopes. For ^{17}O, the calculated magnetic moment and quadrupole moment values using all the interactions are similar, because this is the single-particle moment (similarly for ^{17}F). The calculated magnetic moment of the 4_1^+ state of ^{18}O and of the $5/2^+$ (g.s.) for ^{19}O and 2_1^+ state of ^{20}O are showing negative sign, while the sign has not yet been confirmed experimentally. For ^{19}O, both *ab initio* interactions give the opposite sign of the quadrupole moment with USDB interaction; however, the sign from an experiment is not yet confirmed. The calculated value of magnetic moments for ^{17,18,20}F isotopes (g.s. and some isomers) are close to the experimental data. However, *ab initio* interactions give slightly different values in comparison to the experimental data for ^{19,21}F. In the case of quadrupole moments, experimental sign of $^{17-22}$F isotopes are not yet confirmed. All the interactions give the same sign.

The experimental data for magnetic moments of Ne isotopes are available from ^{19}Ne to ^{25}Ne, while the quadrupole moments are available for ^{21,22,23}Ne. In Ref. [137], shell model results of magnetic moments are reported with USD and CW interactions for odd $^{23-25}$Ne isotopes. Shape changes are reported to occur from collective to single particle in Ne isotopes when moving from ^{19}Ne to ^{25}Ne. It is shown that the magnetic moment is more sensitive than the quadrupole moment for deciding the structure of the nucleus. Our calculated results using *ab initio* approaches for

Table 5.1: Comparison of the experimental magnetic dipole moments (μ_N) with the theoretical values calculated using free g factors for sd shell nuclei. The experimental data are taken from Refs. [117, 138].

Nuclei	State	E_x (keV)	μ_{expt}	$\mu_{\text{IM-SRG}}$	μ_{CCEI}	μ_{USDB}
^{17}O	$5/2^+$	0	$-1.89379(9)$	-1.913	-1.913	-1.913
^{18}O	2^+	1982	$-0.57(3)$	-1.094	-1.022	-0.799
	4^+	3555	2.5(4)	-2.455	-2.438	-2.172
^{19}O	$5/2^+$	0	1.53195(7)	-1.509	-1.518	-1.531
	$3/2^+$	96	$-0.72(9)$	-0.885	-0.869	-0.945
^{20}O	2^+	1674	0.70(3)	-0.921	-0.926	-0.716
^{17}F	$5/2^+$	0	$+4.7213(3)$	$+4.793$	$+4.793$	$+4.793$
^{18}F	3^+	937	$+1.77(12)$	$+1.847$	$+1.826$	$+1.872$
	5^+	1121	$+2.86(3)$	$+2.880$	$+2.880$	$+2.880$
^{19}F	$1/2^+$	0	$+2.628868(8)$	$+2.917$	$+2.932$	$+2.898$
	$5/2^+$	197	3.595(13)	$+3.560$	$+3.611$	$+3.584$
^{20}F	2^+	0	$+2.09335(9)$	$+2.171$	$+2.183$	$+2.092$
^{21}F	$5/2^+$	0	3.9194(12)	$+3.393$	$+3.345$	$+3.779$
^{22}F	4^+	0	$(+)2.6944(4)$	$+2.535$	$+2.477$	$+2.540$
^{19}Ne	$1/2^+$	0	$-1.8846(8)$	-2.060	-2.092	-2.037
	$5/2^+$	238	$-0.740(8)$	-0.608	-0.669	-0.673
^{20}Ne	2^+	1634	$+1.08(8)$	$+1.036$	$+1.037$	$+1.020$
	4^+	4247	$+1.5(3)$	$+2.086$	$+2.095$	$+2.052$
^{21}Ne	$3/2^+$	0	$-0.661797(5)$	-0.665	-0.586	-0.750
	$5/2^+$	351	0.49(4)	-0.350	-0.365	-0.574
^{22}Ne	2^+	1275	$+0.65(2)$	$+0.616$	$+0.550$	$+0.748$
	4^+	3357	$+2.2(6)$	$+1.623$	$+1.332$	$+2.044$
^{23}Ne	$5/2^+$	0	$-1.077(4)$	-0.854	-0.786	-1.050
^{25}Ne	$1/2^+$	0	$-1.0062(5)$	-0.657	-0.924	-0.928
^{20}Na	2^+	0	$+0.3694(2)$	$+0.390$	$+0.330$	$+0.446$
^{21}Na	$3/2^+$	0	$+2.83630(10)$	$+2.445$	$+2.388$	$+2.489$
	$5/2^+$	332	3.7(3)	$+3.194$	$+3.196$	$+3.355$
^{22}Na	3^+	0	$+1.746(3)$	$+1.798$	$+1.806$	$+1.791$
	1^+	583	$+0.523(11)$	$+0.506$	$+0.529$	$+0.518$
^{23}Na	$3/2^+$	0	$+2.2176556(6)$	$+1.972$	$+1.887$	$+2.098$
^{24}Na	4^+	0	$+1.6903(8)$	$+1.377$	$+1.285$	$+1.631$
	1^+	472	$-1.931(3)$	$+0.908$	-0.881	-1.865
^{25}Na	$5/2^+$	0	$+3.683(4)$	$+2.934$	$+3.361$	$+3.367$
^{26}Na	3^+	0	$+2.851(2)$	$+2.296$	$+2.360$	$+2.632$
^{27}Na	$5/2^+$	0	$+3.895(5)$	$+3.230$	$+3.623$	$+3.647$
^{28}Na	1^+	0	$+2.426(5)$	$+2.146$	$+1.760$	$+2.081$
^{29}Na	$3/2^+$	0	$+2.449(8)$	$+2.181$	$+2.198$	$+2.438$
^{30}Na	2^+	0	$+2.083(10)$	$+2.245$	$+2.883$	$+2.418$
^{31}Na	$3/2^+$	0	$+2.305(8)$	$+2.535$	$+2.551$	$+2.614$
^{21}Mg	$5/2^+$	0	$-0.983(7)$	-0.342	-0.351	-0.848
^{23}Mg	$3/2^+$	0	$-0.5364(3)$	-0.305	-0.218	-0.410

Table 5.1: *Continuation.*

Nuclei	State	E_x (keV)	μ_{expt}	$\mu_{\mathrm{IM-SRG}}$	μ_{CCEI}	μ_{USDB}
^{24}Mg	2^+	1369	+1.076(26)	+1.050	+1.094	+1.026
	4^+	4123	+1.6(12)	+2.103	+2.169	+2.070
	2^+	4238	+1.2(4)	+1.072	+1.062	+1.037
	4^+	6010	+2.0(16)	+2.095	+2.115	+2.048
^{25}Mg	$5/2^+$	0	−0.85545(8)	−0.617	−0.197	−0.849
^{26}Mg	2^+	1809	+1.0(3)	+1.024	+1.281	+1.739
^{27}Mg	$1/2^+$	0	−0.411(2)	+0.197	−0.256	−0.412
^{29}Mg	$3/2^+$	0	+0.9780(6)	+1.114	+1.470	+1.071
^{31}Mg	$1/2^+$	0	−0.88355(15)	−0.563	+1.406	−0.923
^{23}Al	$5/2^+$	0	+3.889(5)	+3.716	+3.681	+3.866
^{24}Al	1^+	426	2.99(9)	+2.660	+2.071	+2.985
^{25}Al	$5/2^+$	0	3.6455(12)	+3.462	+3.142	+3.655
^{26}Al	5^+	0	+2.804(4)	+2.850	+2.907	+2.839
^{27}Al	$5/2^+$	0	+3.6415069(7)	+2.525	+2.461	+3.455
^{28}Al	3^+	0	3.242(5)	+2.718	+2.378	+3.098
	2^+	31	+4.3(4)	+1.044	+0.675	+3.215
^{30}Al	3^+	0	3.010(7)	+2.442	+3.455	+3.039
^{31}Al	$(5/2^+)$	0	+3.830(5)	+3.571	+3.863	+3.761
^{32}Al	1^+	0	1.952(2)	+1.485	+1.811	+1.612
^{33}Al	$(5/2^+)$	0	+4.088(5)	+4.012	+4.268	+4.224
^{27}Si	$5/2^+$	0	(−)0.8554(4)	+0.117	+0.337	−0.678
^{28}Si	2^+	1779	+1.1(2)	+1.040	+1.093	+1.031
^{29}Si	$1/2^+$	0	−0.55529(3)	−0.010	−0.575	−0.503
^{30}Si	2^+	2235	+0.8(2)	+0.839	+1.939	+0.732
^{33}Si	$(3/2^+)$	0	1.21(3)	+1.212	+1.803	+1.206
^{28}P	3^+	0	0.312(3)	+1.648	+1.076	+0.302
^{29}P	$1/2^+$	0	1.2346(3)	+0.558	+1.348	+1.133
^{31}P	$1/2^+$	0	+1.13160(3)	+0.081	+1.694	+1.087
	$3/2^+$	1270	+0.30(8)	+0.318	−0.063	+0.167
	$5/2^+$	2230	+2.8(5)	+1.260	+3.097	+2.218
^{32}P	1^+	0	−0.2524(3)	−0.764	+0.177	−0.021
^{31}S	$1/2^+$	0	0.48793(8)	+0.472	−1.003	−0.441
^{32}S	2^+	2231	+0.9(2)	+1.022	+0.980	+1.010
	4^+	4459	+1.6(6)	+2.046	+1.840	+2.028

Table 5.2: Comparison of the experimental quadrupole moments (eb) with the theoretical values calculated by using e_p=1.5e and e_n=0.5e.

Nuclei	State	E_x (keV)	$Q_{\rm expt}$	$Q_{\rm IM-SRG}$	$Q_{\rm CCEI}$	$Q_{\rm USDB}$	Ref.
^{17}O	$5/2^+$	0	−0.02558(22)	−0.0302	−0.0302	−0.0302	[139]
^{18}O	2^+	1982	−0.036(9)	−0.0153	−0.0172	−0.0294	[140]
^{19}O	$5/2^+$	0	0.00362(13)	+0.0003	+0.0005	−0.0026	[119]
^{17}F	$5/2^+$	0	0.0799(34)	−0.0907	−0.0907	−0.0907	[119]
^{18}F	5^+	1121	0.077(5)	−0.1226	−0.1226	−0.1224	[140]
^{19}F	$5/2^+$	197	0.0942(9)	−0.1048	−0.01056	−0.1045	[141]
^{20}F	2^+	0	0.0547(18)	+0.0677	+0.0729	+0.0679	[119]
^{21}F	$5/2^+$	0	0.0943(33)	−0.1180	−0.1175	−0.1199	[119]
^{22}F	4^+	0	0.003(2)	−0.0167	−0.0249	−0.0078	[140]
^{20}Ne	2^+	1634	−0.23(3)	−0.1573	−0.1578	−0.1576	[140]
^{21}Ne	$3/2^+$	0	+0.10155(75)	+0.1127	+0.1109	+0.1119	[119, 139]
^{22}Ne	2^+	1257	−0.19(4)	−0.1561	−0.1536	−0.1532	[140]
^{23}Ne	$5/2^+$	0	+0.1429(43)	+0.1728	+0.1699	+0.1629	[119]
^{20}Na	2^+	0	0.1009(88)	+0.0961	+0.100	+0.0946	[119]
^{21}Na	$3/2^+$	0	0.137(12)	+0.1224	+0.1216	+0.1218	[119]
^{22}Na	3^+	0	+0.167(17)	+0.2496	+0.2405	+0.2506	[119]
^{23}Na	$3/2^+$	0	+0.104(1)	+0.1217	+0.1246	+0.1180	[119, 142]
^{25}Na	$5/2^+$	0	0.00146(22)	+0.0214	+0.0674	+0.0025	[119]
^{26}Na	3^+	0	0.00521(20)	−0.0056	+0.0239	−0.0051	[119]
^{27}Na	$5/2^+$	0	0.00708(24)	−0.0120	−0.0035	−0.0127	[119]
^{28}Na	1^+	0	0.0389(11)	+0.0539	+0.0368	+0.0495	[119]
^{29}Na	$3/2^+$	0	+0.0842(25)	+0.0737	+0.1046	+0.0791	[119]
^{30}Na	2^+	0	+0.146(1.6)	−0.1122	−0.1048	−0.1149	[143]
^{31}Na	$3/2^+$	0	+0.105(2.5)	+0.0465	+0.0920	+0.0583	[143]
^{23}Mg	$3/2^+$	0	0.1133(37)	+0.1285	+0.1322	+0.1229	[119]
^{24}Mg	2^+	1369	−0.29(3)	−0.1914	−0.1857	−0.1931	[140]
^{25}Mg	$5/2^+$	0	+0.1994(20)	+0.2235	+0.1809	+0.2243	[144]
^{26}Mg	2^+	1809	−0.21(2)	−0.1747	+0.1155	−0.1439	[140]
^{25}Al	$5/2^+$	0	0.249(18)	+0.1949	+0.1813	+0.2018	[119]
^{26}Al	5^+	0	+0.259(29)	+0.3260	+0.294	+0.3028	[119]
^{27}Al	$5/2^+$	0	+0.1466(10)	+0.1563	+0.091	+0.1803	[119, 145]
^{28}Al	3^+	0	0.172(12)	+0.2289	+0.1388	+0.1877	[119]
^{31}Al	$5/2^+$	0	0.1365(23)	+0.1836	+0.1320	+0.1706	[134]
^{32}Al	1^+	0	0.0250(21)	+0.0370	+0.006	+0.0310	[119]
^{33}Al	$5/2^+$	0	0.141(3)	+0.1375	+0.1368	+0.1390	[134]
^{27}Si	$5/2^+$	0	0.063(14)	+0.1291	+0.072	+0.1409	[146]
^{28}Si	2^+	1779	+0.16(3)	+0.2332	+0.196	+0.2087	[140]
^{30}Si	2^+	2235	−0.05(6)	+0.0465	+0.1470	+0.0239	[140]
^{32}S	2^+	1941	−0.15(2)	−0.0140	−0.0801	−0.1283	[140]
^{33}S	$3/2^+$	0	−0.0678(13)	−0.1431	−0.0565	−0.0736	[147]

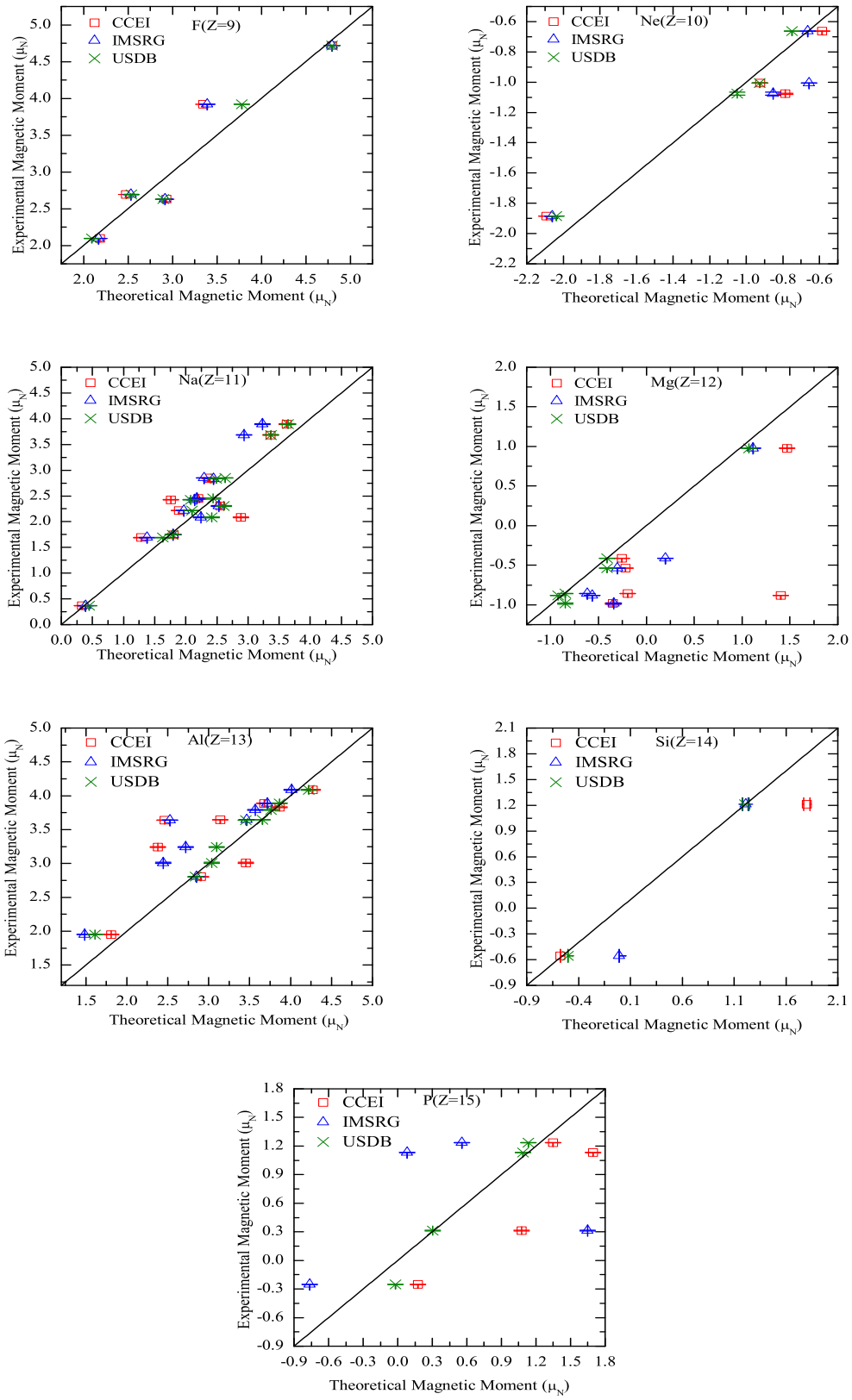

Figure 5.1: Comparison between the experimental and theoretical magnetic dipole moments for F, Ne, Na, Mg, Al, Si, and P isotopes. The calculated shell model signs are used in the cases when it was not measured.

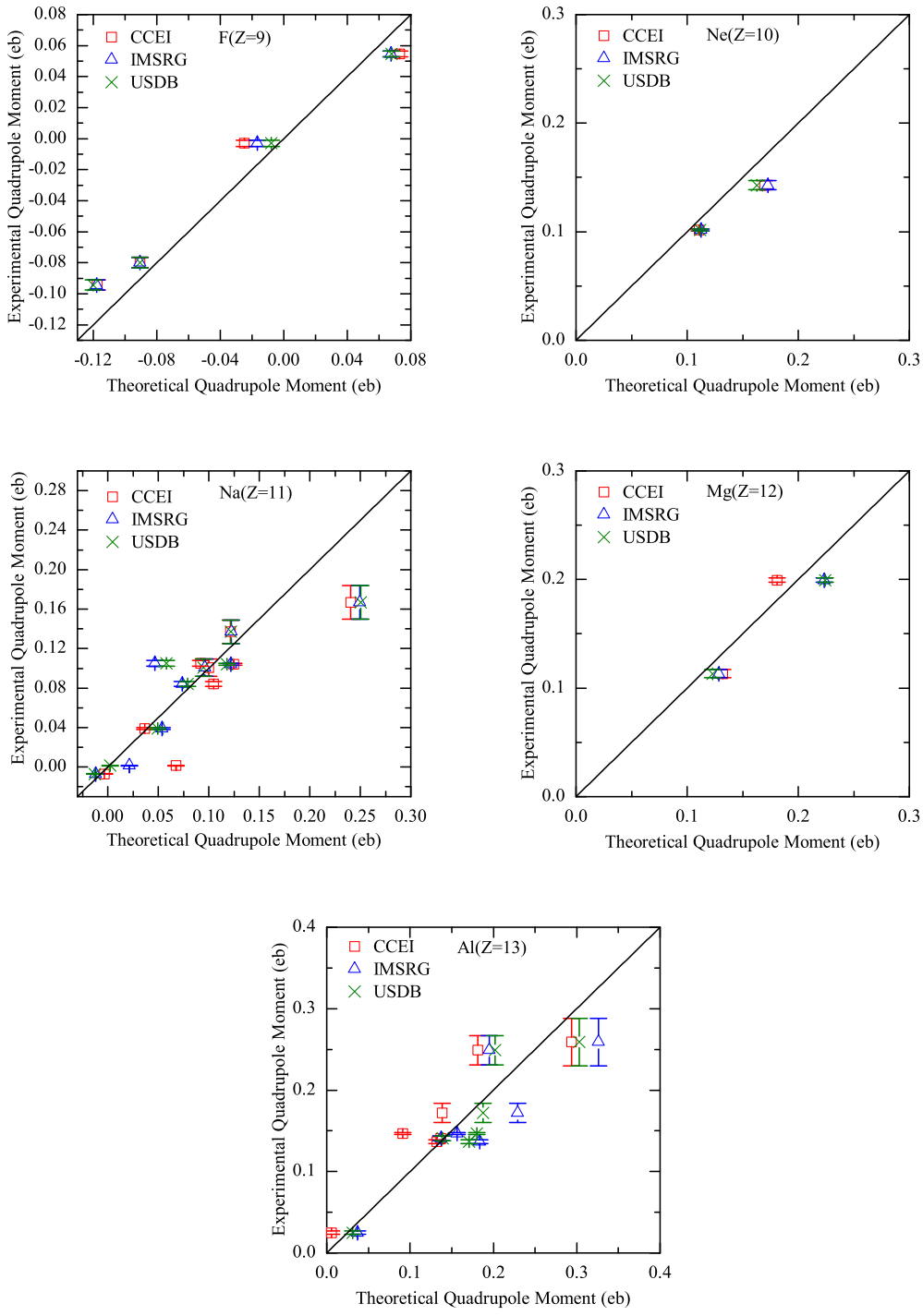

Figure 5.2: Comparison between experimental and theoretical quadrupole moments for F, Ne, Na, Mg and Al isotopes. The calculated shell model signs are used in case when it was not measured.

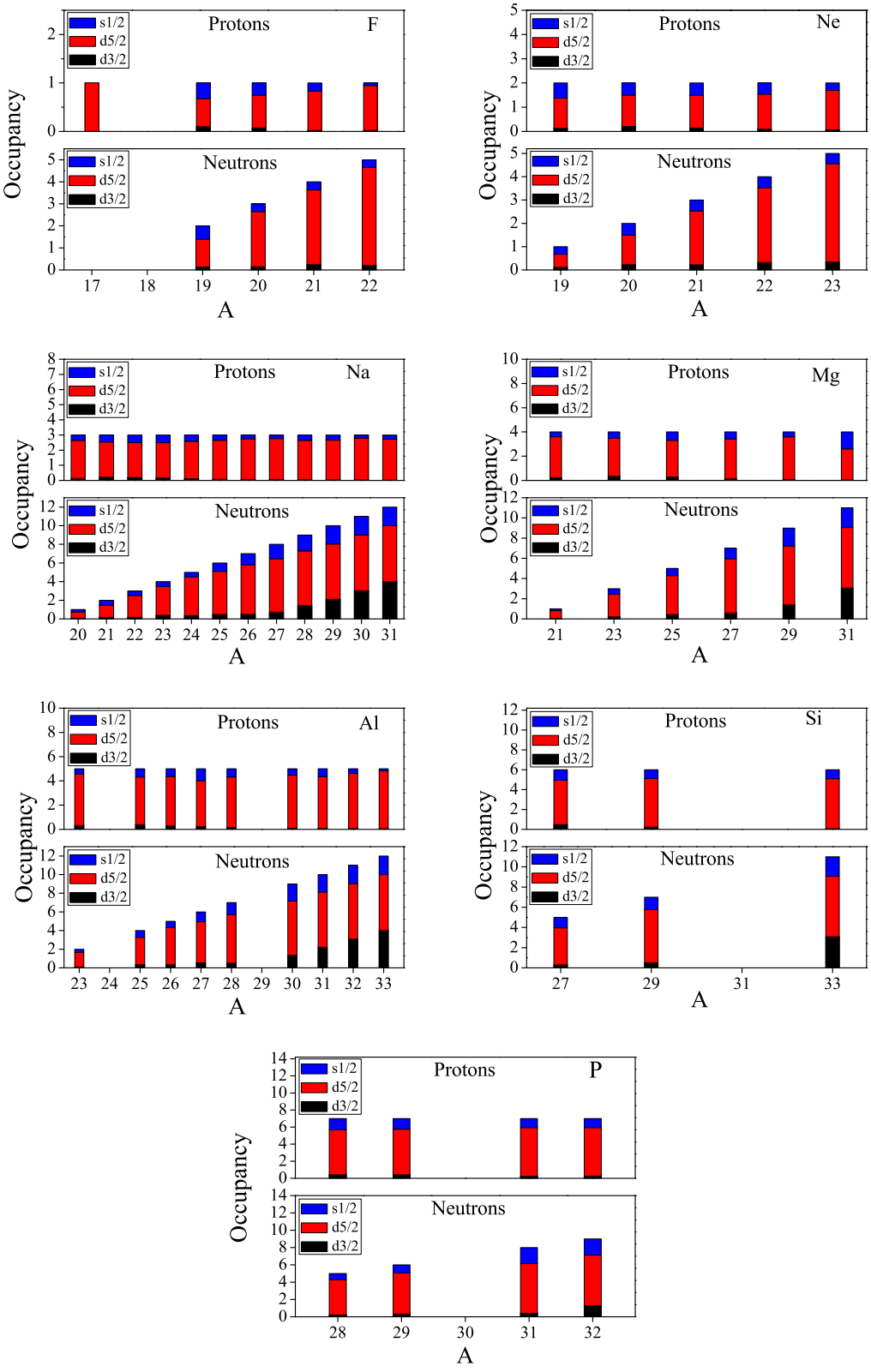

Figure 5.3: Occupancies of $d_{3/2}$, $d_{5/2}$ and $s_{1/2}$ proton and neutron orbitals for $^{19-22}$F, $^{19-23}$Ne, $^{20-31}$Na, $^{21-31}$Mg, $^{23,25-28,30-33}$Al, ^{27,29,33}Si and $^{28-29,31-32}$P isotopes with CCEI for the g.s. We have reported occupancies of those nuclei for which the quadrupole/magnetic moments are calculated in the present work.

magnetic moments are showing reasonable agreement with the experimental data except for ^{23,25}Ne isotopes. We have reported the quadrupole moments for $^{20-23}$Ne isotopes. Both *ab initio* results are in good agreement with the experimental data. In the case of ^{20}Ne, the calculated Q_{2^+} with all the three interactions is approximately -0.15 eb, while experimental value is $-0.23(3)$ eb.

In the $^{26-31}$Na chain [125], it is claimed that the experimental results of the magnetic moments for $^{26-29}$Na are well described with *sd* model space using the USD Hamiltonian. The disagreement appears for the $^{30-31}$Na magnetic moments. The ^{30,31}Na isotopes are suggested to be members of the island of inversion, as shown by Utsuno *et al*. [148]. We have calculated the magnetic moments for the g.s. for $^{20-31}$Na isotopes. In the case of ^{21,22}Na and ^{24}Na, the magnetic moments are also given for the first excited state. The results obtained from *ab initio* approaches for the g.s. are in reasonable agreement with the experimental values (Fig. 5.1). In the case of ^{24}Na, for the magnetic moment (for the first excited state), the sign is reverse using IM-SRG while CCEI gives the sign which is in agreement with the experimental data. We have calculated the quadrupole moments for $^{20-23}$Na and $^{25-31}$Na. For ^{26}Na, *ab initio* IM-SRG interaction is giving same sign of the quadrupole moment as in the phenomenological effective interaction. Experimentally, the sign has not yet been confirmed. In the case of ^{30}Na, the results obtained from theory are far from the experimental value because ^{30}Na is an element of the island of inversion. To explain the quadrupole moment for ^{30}Na we need pf model space. Utsuno *et al*. [148], performed theoretical calculations in $sdf_{7/2}p_{3/2}$ model space using SDPF-M interaction [149] for ^{27,29}Na isotopes using the Monte Carlo shell model approach.

For Mg isotopes, the *sd* shell model space is able to explain the experimental data reasonably well up to ^{29}Mg with all the three interactions. However, in the case of ^{27}Mg, IM-SRG interaction gives opposite sign with the experimental data. In the case of ^{23}Mg, for $Q(3/2^+)$, the experimental sign has not yet been confirmed. Recently, the sign of magnetic moment has been measured using laser spectroscopy

at CERN-ISOLDE [150]. Shell model calculations predict a positive sign for the quadrupole moment. In the case of ^{27}Mg, the negative magnetic moment for the g.s. is dominated by the $\nu s_{1/2}$ configuration. The IM-SRG fails to reproduce the correct sign of its magnetic moment, although it is also predicting $\nu s_{1/2}$ configuration for the g.s. For ^{29}Mg, the g.s. spin is $I = 3/2$ ($\nu d_{3/2}$), and all interactions give the correct sign of the magnetic moment. The *sd* model space is not able to reproduce correctly the measured g.s. $1/2^+$ for ^{31}Mg. For this isotope, a strongly prolate deformed g.s. is reported in Ref. [122]. Recent theoretical results reveal the existence of $2p-2h$ and $4p-4h$ configurations for ^{32}Mg [151].

For $^{25-28,30-33}$Al isotopes, the *sd* model space is able to correctly reproduce the magnetic moments. In most of the isotopes, CCEI results are in reasonable agreement with the experimental data. For ^{25,28,30,32}Al isotopes, the sign for the g.s. magnetic moment is not yet confirmed, theoretically all the three interactions predict positive sign. The calculated $\mu(2^+)$ and $\mu(3^+)$ for ^{28}Al with IM-SRG and CCEI are not showing good agreement with the experimental data. Also, *ab initio* interactions are giving smaller values of the magnetic moment for ^{27}Al. Experimentally, the sign of the quadrupole moment is confirmed only for ^{26,27}Al isotopes. For ^{26}Al, the CCEI result for quadrupole moment is in reasonable agreement with experimental data, while for ^{27}Al, the result of quadrupole moment with IM-SRG is better than CCEI.

In the Si chain, the magnetic moments for ^{27,29,33}Si isotopes are calculated for the g.s. while for ^{28,30}Si isotopes they are for the first excited state. For ^{28,29}Si isotopes, the magnetic moments from the CCEI approach are in reasonable agreement. The calculated $\mu(1/2^+)$ for ^{29}Si is suppressed with IM-SRG in comparison with the experimental data. The *ab initio* interactions are giving smaller values with the opposite sign of $\mu(5/2^+)$ for ^{27}Si in comparison to the experimental data and with USDB interaction; however, the experimental sign is tentative. The quadrupole moment is calculated for ^{27}Si, ^{28}Si, and ^{30}Si. For ^{30}Si, all the three interactions fail to reproduce the correct sign of the quadrupole moment.

We have also reported the magnetic moments of ^{28,29,31,32}P, and all the calculated

results support positive signs for P isotopes in the g.s. except ^{32}P. For ^{32}P, IM-SRG supports the experimental sign but the magnitude is larger in comparison with the experimental value. We have also calculated the magnetic moment of ^{31,32}S and the quadrupole moment of ^{32,33}S. The CCEI results for magnetic moments (^{32}S) and quadrupole moments (^{33}S) are in reasonable agreement with the experimental data.

The calculated g factors with *ab initio* interactions for the yrast levels in even-even $N = Z$ nuclei are ~ 0.5. Thus, the calculated value is in agreement with the experimental value as reported in Ref. [152].

In Fig. 5.1, we have shown the comparison between the experimental and theoretical magnetic dipole moments for F, Ne, Na, Mg, Al, Si, and P isotopes. From this figure, it is clear that *ab initio* interactions are not giving value close to the experimental data for heavier Z nuclei. The deviation between the calculated and the experimental data is large for P isotopes. In the Figs. 5.1 and 5.2, we have shown comparison only for the g.s. of those nuclei which have confirmed experimental signs. Apart from this, we have also plotted the g.s. of those data for which all the interactions are giving the same sign but their experimental signs are not yet confirmed.

The g.s. quadrupole moments for F, Ne, Na, Mg and Al isotopes are shown in the Fig. 5.2. All the interactions are giving reasonable results for the F isotopes. For the ^{22}Na, the calculated quadrupole moment is larger in comparison with the experimental data for all the three interactions. For ^{25}Na, *ab initio* interactions give larger $Q(5/2^+)$ values in comparison with the experimental data; however, the result with USDB interaction is reasonable.

The occupancies of $d_{3/2}$, $d_{5/2}$, and $s_{1/2}$ proton and neutron orbitals for $^{19-22}$F, $^{19-23}$Ne, $^{20-31}$Na, $^{21-31}$Mg, $^{23,25-28,30-33}$Al, ^{27,29,33}Si and $^{28-29,31-32}$P isotopes with CCEI for the g.s are shown in Fig. 5.3. In general, the role of the $d_{5/2}$ orbital is important as neutron number increases.

For ^{30}Na (expt. g.s. is 2^+), IM-SRG and CCEI effective interactions predict g.s. as 0^+, while USDB predicts 2^+. For ^{30}Na, the calculated magnetic moment with

IM-SRG interaction is in reasonable agreement with the experimental data; however, all three interactions give opposite signs for quadrupole moment in comparison with the experimental data. For ^{31}Na (experimental g.s. is $3/2^+$), CCEI predicts the correct g.s. while USDB and IM-SRG give $5/2^+$. For this nuclei, the magnetic moments predicted by *ab initio* interactions are similar, whereas the quadrupole moment predicted by CCEI is close to the experimental data. For ^{31}Mg (experimental g.s. is $1/2^+$), *ab initio* and USDB interactions give g.s. of $3/2^+$. The calculated magnetic moment with CCEI is far from the experimental value and also the sign is not correct. For ^{33}Al, all the three interactions give the g.s. as $5/2^+$, although experimentally it is not yet confirmed. The IM-SRG gives value of magnetic moment close to the experimental data for this isotope. In the case of quadrupole moment, sign is not yet confirmed experimentally, but the magnitude is in reasonable agreement with experimental value with all the three interactions.

The wave functions of the nuclei which show disagreement between *ab initio* results and with the experimental data and USDB results are shown in Table 5.3. For ^{27}Al, both *ab initio* interactions give same structure. The *ab initio* results for $\mu_{5/2^+}$ are not in a good agreement with the experimental data. In ^{28}Al, the CCEI result for $\mu_{2_1^+}$ is very far from IM-SRG and USDB interactions as well as with the experimental data; also, the wave function is different from IM-SRG and USDB. In the case of CCEI interaction for the ^{28}Al($\mu_{2_1^+}$) result, we have one unpaired proton and one unpaired neutron in $s_{1/2}$ orbits whereas in USDB and IM-SRG interactions, we have one unpaired neutron in $s_{1/2}$ orbits, and one unpaired proton in $d_{5/2}$ orbit. USDB and IM-SRG are also not in very good agreement with the experimental data. In ^{32}Al, all the three interactions give same structure for the wave function but still CCEI result for $Q_{1_1^+}$ is far from the experimental data. In ^{27}Si, the structures of wave function for CCEI interaction is due to two unpaired protons and one unpaired neutron, whereas in IM-SRG and USDB interactions come from one unpaired neutron in $d_{5/2}$ orbit. In the case of ^{30}Si, the CCEI result for $Q_{2_1^+}$ is very far from the experiment, the structure comes because of the two unpaired protons which are in

$s_{1/2}$ and $d_{5/2}$ orbits, while for IM-SRG and USDB interactions two unpaired neutrons are in $d_{3/2}$ and $s_{1/2}$ orbits. For ^{31}P ($\mu_{1/2_1^+}$, $\mu_{5/2_1^+}$), ^{32}S ($Q_{2_1^+}$) and ^{33}S ($Q_{3/2_1^+}$), the structures of wave functions for IM-SRG are very different from USDB and CCEI interactions. For these nuclei, we can see results from Tables 5.1 and 5.2 that show the IM-SRG results are very far from the experimental data. For ^{28}Na, ^{25}Mg, ^{32}Al, ^{29}Si, and ^{29}P all three calculations give the same structure of the wave functions. But we can see from Table 5.1 a deviation of one of the *ab initio* results with the other two interactions and the experimental data. For ^{28}P, all the three calculations give same structure but the magnitude of USDB result is closer to the experimental data. However, the experimental sign has not yet been confirmed.

Table 5.3: Dominant configuration of the wave functions with *ab intio* effective interactions and USDB effective interaction. In these nuclei *ab initio* results are showing deviation with experimental data and USDB effective interaction results.

Nuclei	Spin	IM-SRG	Probability	CCEI	Probability
^{28}Na	μ_{1^+}	$\pi(d^0_{3/2},d^3_{5/2},s^0_{1/2}) \otimes \nu(d^1_{3/2},d^6_{5/2},s^2_{1/2})$	41.71%	$\pi(d^0_{3/2},d^3_{5/2},s^0_{1/2}) \otimes \nu(d^1_{3/2},d^6_{5/2},s^2_{1/2})$	43.52%
^{25}Mg	$\mu_{5/2^+_1}$	$\pi(d^0_{3/2},d^4_{5/2},s^0_{1/2}) \otimes \nu(d^0_{3/2},d^5_{5/2},s^0_{1/2})$	16.99%	$\pi(d^0_{3/2},d^4_{5/2},s^0_{1/2}) \otimes \nu(d^0_{3/2},d^5_{5/2},s^0_{1/2})$	18.14%
^{27}Al	$\mu_{5/2^+_1}$	$\pi(d^0_{3/2},d^4_{5/2},s^1_{1/2}) \otimes \nu(d^0_{3/2},d^5_{5/2},s^1_{1/2})$	6.46%	$\pi(d^0_{3/2},d^4_{5/2},s^1_{1/2}) \otimes \nu(d^0_{3/2},d^5_{5/2},s^1_{1/2})$	12.92%
^{28}Al	$\mu_{3^+_1}$	$\pi(d^0_{3/2},d^5_{5/2},s^0_{1/2}) \otimes \nu(d^0_{3/2},d^6_{5/2},s^1_{1/2})$	14.98%	$\pi(d^0_{3/2},d^5_{5/2},s^0_{1/2}) \otimes \nu(d^0_{3/2},d^6_{5/2},s^1_{1/2})$	29.47%
	$\mu_{2^+_1}$	$\pi(d^0_{3/2},d^5_{5/2},s^0_{1/2}) \otimes \nu(d^0_{3/2},d^6_{5/2},s^1_{1/2})$	7.72%	$\pi(d^0_{3/2},d^4_{5/2},s^1_{1/2}) \otimes \nu(d^0_{3/2},d^6_{5/2},s^1_{1/2})$	11.66%
^{32}Al	$Q_{1^+_1}$	$\pi(d^0_{3/2},d^5_{5/2},s^0_{1/2}) \otimes \nu(d^3_{3/2},d^6_{5/2},s^2_{1/2})$	71.50%	$\pi(d^0_{3/2},d^5_{5/2},s^0_{1/2}) \otimes \nu(d^3_{3/2},d^6_{5/2},s^2_{1/2})$	65.89%
^{27}Si	$\mu_{5/2^+_1}$	$\pi(d^0_{3/2},d^6_{5/2},s^0_{1/2}) \otimes \nu(d^0_{3/2},d^5_{5/2},s^0_{1/2})$	9.27%	$\pi(d^0_{3/2},d^5_{5/2},s^1_{1/2}) \otimes \nu(d^0_{3/2},d^4_{5/2},s^1_{1/2})$	13.24%
^{29}Si	$\mu_{1/2^+_1}$	$\pi(d^0_{3/2},d^6_{5/2},s^0_{1/2}) \otimes \nu(d^0_{3/2},d^6_{5/2},s^1_{1/2})$	11.62%	$\pi(d^0_{3/2},d^6_{5/2},s^0_{1/2}) \otimes \nu(d^0_{3/2},d^6_{5/2},s^1_{1/2})$	29.18%
^{30}Si	$Q_{2^+_1}$	$\pi(d^0_{3/2},d^6_{5/2},s^0_{1/2}) \otimes \nu(d^1_{3/2},d^6_{5/2},s^1_{1/2})$	8.21%	$\pi(d^0_{3/2},d^5_{5/2},s^1_{1/2}) \otimes \nu(d^0_{3/2},d^6_{5/2},s^2_{1/2})$	33.80%
^{28}P	$\mu_{3^+_1}$	$\pi(d^0_{3/2},d^6_{5/2},s^1_{1/2}) \otimes \nu(d^0_{3/2},d^5_{5/2},s^0_{1/2})$	8.61%	$\pi(d^0_{3/2},d^6_{5/2},s^1_{1/2}) \otimes \nu(d^0_{3/2},d^5_{5/2},s^0_{1/2})$	29.43%
^{29}P	$\mu_{1/2^+_1}$	$\pi(d^0_{3/2},d^6_{5/2},s^1_{1/2}) \otimes \nu(d^0_{3/2},d^6_{5/2},s^0_{1/2})$	10.38%	$\pi(d^0_{3/2},d^6_{5/2},s^1_{1/2}) \otimes \nu(d^0_{3/2},d^6_{5/2},s^0_{1/2})$	28.56%
^{31}P	$\mu_{1/2^+_1}$	$\pi(d^0_{3/2},d^6_{5/2},s^1_{1/2}) \otimes \nu(d^2_{3/2},d^6_{5/2},s^0_{1/2})$	6.46%	$\pi(d^0_{3/2},d^6_{5/2},s^1_{1/2}) \otimes \nu(d^0_{3/2},d^6_{5/2},s^2_{1/2})$	66.90%
	$\mu_{3/2^+_1}$	$\pi(d^0_{3/2},d^6_{5/2},s^1_{1/2}) \otimes \nu(d^2_{3/2},d^6_{5/2},s^0_{1/2})$	6.44%	$\pi(d^0_{3/2},d^6_{5/2},s^1_{1/2}) \otimes \nu(d^1_{3/2},d^6_{5/2},s^1_{1/2})$	22.13%
	$\mu_{5/2^+_1}$	$\pi(d^1_{3/2},d^5_{5/2},s^1_{1/2}) \otimes \nu(d^2_{3/2},d^6_{5/2},s^0_{1/2})$	5.94%	$\pi(d^0_{3/2},d^5_{5/2},s^2_{1/2}) \otimes \nu(d^0_{3/2},d^6_{5/2},s^2_{1/2})$	53.89%
^{32}S	$Q_{2^+_1}$	$\pi(d^2_{3/2},d^5_{5/2},s^1_{1/2}) \otimes \nu(d^2_{3/2},d^5_{5/2},s^1_{1/2})$	4.72%	$\pi(d^0_{3/2},d^6_{5/2},s^2_{1/2}) \otimes \nu(d^1_{3/2},d^6_{5/2},s^1_{1/2})$	36.14%
^{33}S	$Q_{3/2^+_1}$	$\pi(d^2_{3/2},d^6_{5/2},s^0_{1/2}) \otimes \nu(d^1_{3/2},d^6_{5/2},s^2_{1/2})$	7.93%	$\pi(d^0_{3/2},d^6_{5/2},s^2_{1/2}) \otimes \nu(d^1_{3/2},d^6_{5/2},s^2_{1/2})$	77.18%

Table 5.3: *Continuation.*

Nuclei	Spin	USDB	Probability
^{28}Na	μ_{1^+}	$\pi(d^0_{3/2},d^3_{5/2},s^0_{1/2}) \otimes \nu(d^1_{3/2},d^6_{5/2},s^2_{1/2})$	51.85%
^{25}Mg	$\mu_{5/2^+_1}$	$\pi(d^0_{3/2},d^4_{5/2},s^0_{1/2}) \otimes \nu(d^0_{3/2},d^5_{5/2},s^0_{1/2})$	26.20%
^{27}Al	$\mu_{5/2^+_1}$	$\pi(d^0_{3/2},d^5_{5/2},s^0_{1/2}) \otimes \nu(d^0_{3/2},d^6_{5/2},s^0_{1/2})$	27.19%
^{28}Al	$\mu_{3^+_1}$	$\pi(d^0_{3/2},d^5_{5/2},s^0_{1/2}) \otimes \nu(d^0_{3/2},d^6_{5/2},s^1_{1/2})$	37.28%
	$\mu_{2^+_1}$	$\pi(d^0_{3/2},d^5_{5/2},s^0_{1/2}) \otimes \nu(d^0_{3/2},d^6_{5/2},s^1_{1/2})$	28.15%
^{32}Al	$Q_{1^+_1}$	$\pi(d^0_{3/2},d^5_{5/2},s^0_{1/2}) \otimes \nu(d^3_{3/2},d^6_{5/2},s^2_{1/2})$	78.19%
^{27}Si	$\mu_{5/2^+_1}$	$\pi(d^0_{3/2},d^6_{5/2},s^0_{1/2}) \otimes \nu(d^0_{3/2},d^5_{5/2},s^0_{1/2})$	27.35%
^{29}Si	$\mu_{1/2^+_1}$	$\pi(d^0_{3/2},d^6_{5/2},s^0_{1/2}) \otimes \nu(d^0_{3/2},d^6_{5/2},s^1_{1/2})$	32.52%
^{30}Si	$Q_{2^+_1}$	$\pi(d^0_{3/2},d^6_{5/2},s^0_{1/2}) \otimes \nu(d^1_{3/2},d^6_{5/2},s^1_{1/2})$	25.39%
^{28}P	$\mu_{3^+_1}$	$\pi(d^0_{3/2},d^6_{5/2},s^1_{1/2}) \otimes \nu(d^0_{3/2},d^5_{5/2},s^0_{1/2})$	37.24%
^{29}P	$\mu_{1/2^+_1}$	$\pi(d^0_{3/2},d^6_{5/2},s^1_{1/2}) \otimes \nu(d^0_{3/2},d^6_{5/2},s^0_{1/2})$	32.60%
^{31}P	$\mu_{1/2^+_1}$	$\pi(d^0_{3/2},d^6_{5/2},s^1_{1/2}) \otimes \nu(d^0_{3/2},d^6_{5/2},s^2_{1/2})$	34.38%
	$\mu_{3/2^+_1}$	$\pi(d^1_{3/2},d^6_{5/2},s^0_{1/2}) \otimes \nu(d^0_{3/2},d^6_{5/2},s^2_{1/2})$	15.28%
	$\mu_{5/2^+_1}$	$\pi(d^0_{3/2},d^5_{5/2},s^2_{1/2}) \otimes \nu(d^0_{3/2},d^6_{5/2},s^2_{1/2})$	19.05%
^{32}S	$Q_{2^+_1}$	$\pi(d^0_{3/2},d^6_{5/2},s^2_{1/2}) \otimes \nu(d^1_{3/2},d^6_{5/2},s^1_{1/2})$	11.36%
^{33}S	$Q_{3/2^+_1}$	$\pi(d^0_{3/2},d^6_{5/2},s^2_{1/2}) \otimes \nu(d^1_{3/2},d^6_{5/2},s^2_{1/2})$	47.69%

5.4 Collectivity for sd shell nuclei

In this section, we have calculated $B(E2; 2_1^+ \rightarrow 0_1^+)$ for selected nuclei Ne, Mg and Si isotopes with $10 \leq N \leq 20$ using above *ab initio* interactions. We have also compared results with a phenomenological USDB effective interaction and the recently derived interaction from effective field theory, which will be referred to CEFT [153]. We perform calculations with SDPF-MU interaction [154] in the $sd - pf$ shell. For the diagonalization of matrices, we have used shell model code KSHELL [105].

The $B(E2)$ values are calculated with the formula:

$$B(E2) = \frac{1}{2J_i + 1} \mid (J_f \mid\mid \sum_i e_i r_i^2 Y_2(\theta_i, \phi_i) \mid\mid J_i) \mid^2 . \tag{5.10}$$

Where, J_i and J_f are the initial and final state spins, respectively. The $B(E2)$ values are calculated with the effective charges e_p=1.35e and e_n=0.35e.

The $E_{2_1^+}$ and $B(E2; 2_1^+ \rightarrow 0_1^+)$ transitions using *ab initio* interactions and USDB interactions along with experimental data for even Ne isotopes with $N = 10 - 20$ are shown in Fig. 5.4. The USDB results for $E_{2_1^+}$ are close to experimental data up to $N = 16$ but above this, the results are deviating. The IM-SRG results are the best and close to the experimental data from $N = 10$ to $N = 18$. At $N = 20$, only CCEI shows the same pattern as the experimental data, while results of all the other interactions go upward deviating from the experiment. Experimentally, $N = 18$ shows less collectivity in comparison to $N = 16$ and an enhancement in collectivity is seen at $N = 20$. The $B(E2)$ values obtained are not satisfactory especially at $N = 20$ for Ne and Mg isotopes. For all the interactions the collectivity is decreasing from $N = 18$ to $N = 20$ in contrast to the experiment. From the literature the $N = 20$ lies on the boundary of "island of inversion" [155] and $0\hbar\omega$ shell model calculations are not able to reproduce the enhancement in collectivity at $N = 20$. To see the importance of neutron excitations from sd to pf shell, we have shown results with $2p - 2h$ and $4p - 4h$ excitations in Fig. 5.5. The results with $4p - 4h$ excitations

show the same trends as in the experiment: there is an increase of $B(E2; 2_1^+ \rightarrow 0_1^+)$ from $N = 18$ to $N = 20$ though not enough to reproduce the experimental data. The increase in the occupancy of pf orbitals is also confirmed from Fig. 5.6.

For the Mg isotopes, the energy of the 2_1^+ state is near to the experimental data with IM-SRG effective interaction except at $N = 14$ and $N = 20$. The CCEI results are also good except at $N = 14$. At $N = 20$ the energy of the 2_1^+ state is correctly given by CCEI but $B(E2)$ value is far from the experimental data. This shows there is a problem with the wavefunction, that is, there is a large configuration mixing in this wavefunction. Here, with *ab initio* interactions it is not possible to show collectivity at $N = 20$. The shell model results with $2p-2h$ and $4p-4h$ excitations for SDPF-MU interaction are shown in Fig. 5.5. They show a smooth decrease in $B(E2)$ values from $N = 12-16$ for both $2p-2h$ and $4p-4h$ excitations, however, the results of $4p-4h$ show the same trends as in the experiment at $N = 20$: there is an increase of $B(E2; 2_1^+ \rightarrow 0_1^+)$ from $N = 18$ to $N = 20$. In the case of ^{34}Si isotope, none of the interaction explains properly the spectra. For Si isotopes the trend of the energy of 2_1^+ state for $N = 10$ to $N = 18$ isotopes are well predicted by CEFT and USDB interactions. The $B(E2; 2_1^+ \rightarrow 0_1^+)$ the trend from $N = 12$ to $N = 18$ are showing reasonable agreement with the experiment for all the interactions. The $B(E2; 2_1^+ \rightarrow 0_1^+)$ values for the case with $2p-2h$ and $4p-4h$ excitations show similar results.

In the present calculations, the gap between $d_{3/2}$ orbital and fp shell is large for the SDPF-MU interaction compared with the interaction in Ref. [156], where the neutron ESPE's of pf-shell are very close to the sd-shell; the difference between $f_{7/2}$ and $d_{3/2}$ is as small as about 2 MeV for Z=12 (N=20). Therefore, even if we allow $4p-4h$ excitation from sd to pf shell, the occupancy of fp-shell are around 2.23 in ^{32}Mg. As we can see in Ref. [156], where energies and $B(E2)$ are well reproduced up to $N = 20$, the occupancy of fp-shell becomes as large as 3.5 for ^{32}Mg. Thus, our results might be improved if we reduce the gap between sd and fp shells for the SPDF-MU interaction.

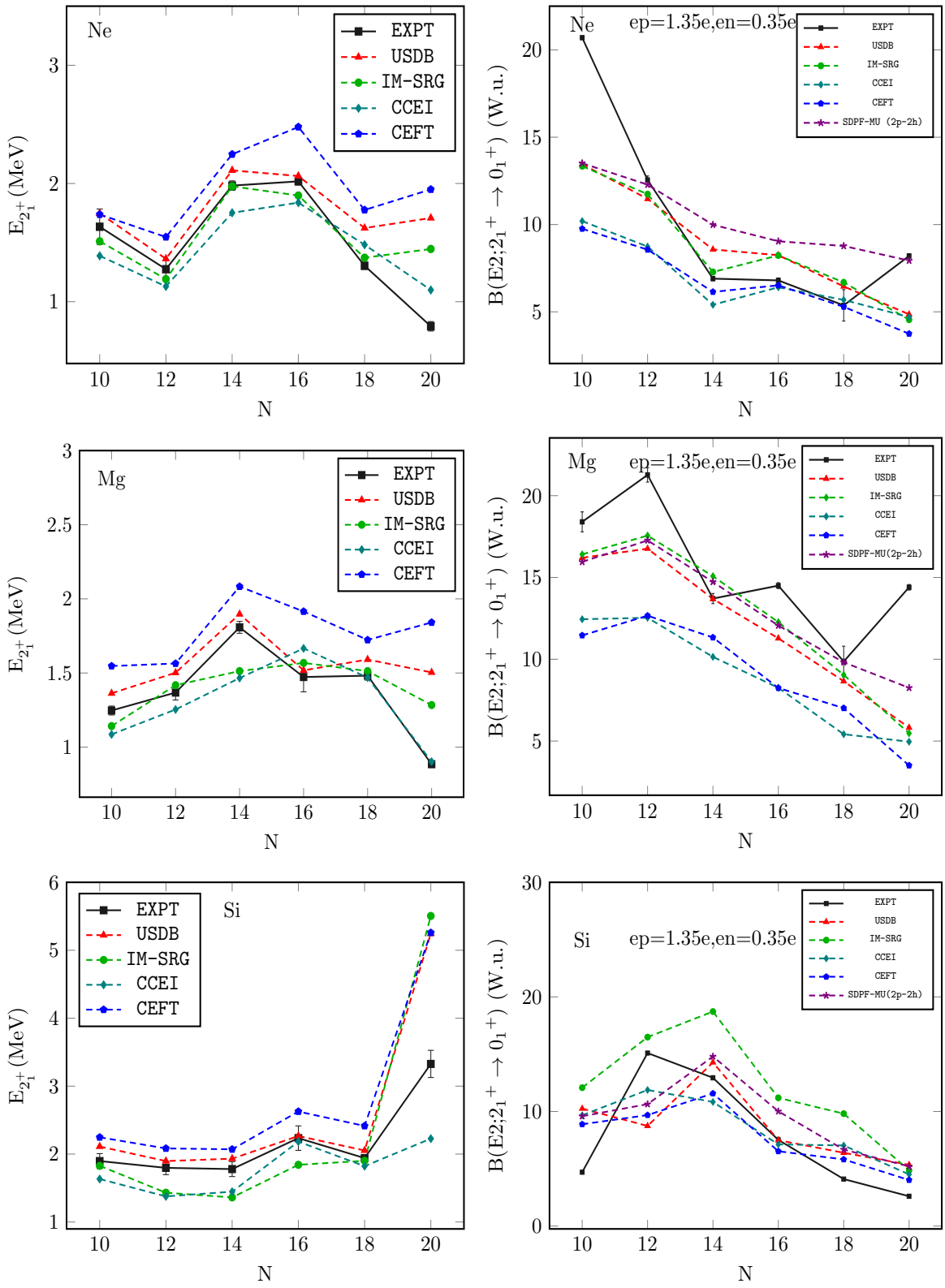

Figure 5.4: The energy of 2_1^+ and $B(E2; 2_1^+ \to 0_1^+)$ values of Ne, Mg and Si isotopes.

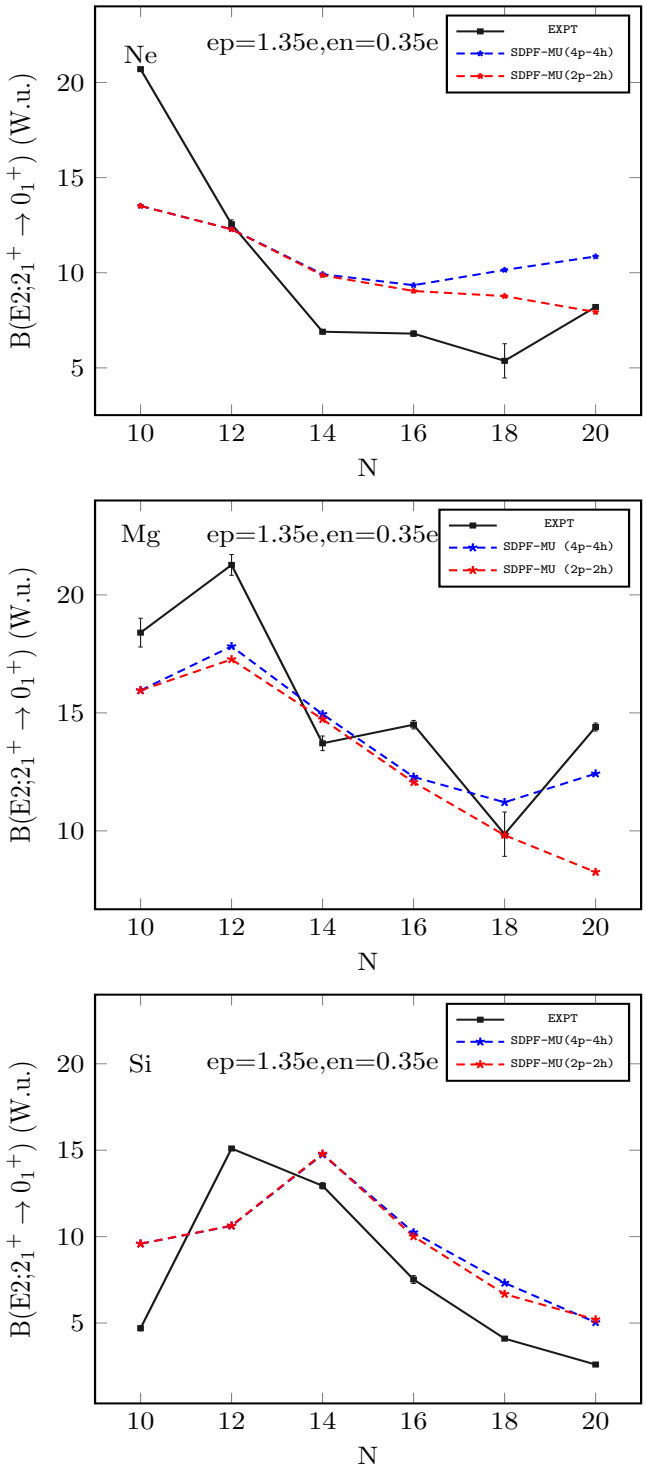

Figure 5.5: Comparison between calculated and experimental $B(E2; 2_1^+ \rightarrow 0_1^+)$ values of Ne, Mg and Si isotopes for $sd - pf$ shell with $2p - 2h$ and $4p - 4h$ excitations.

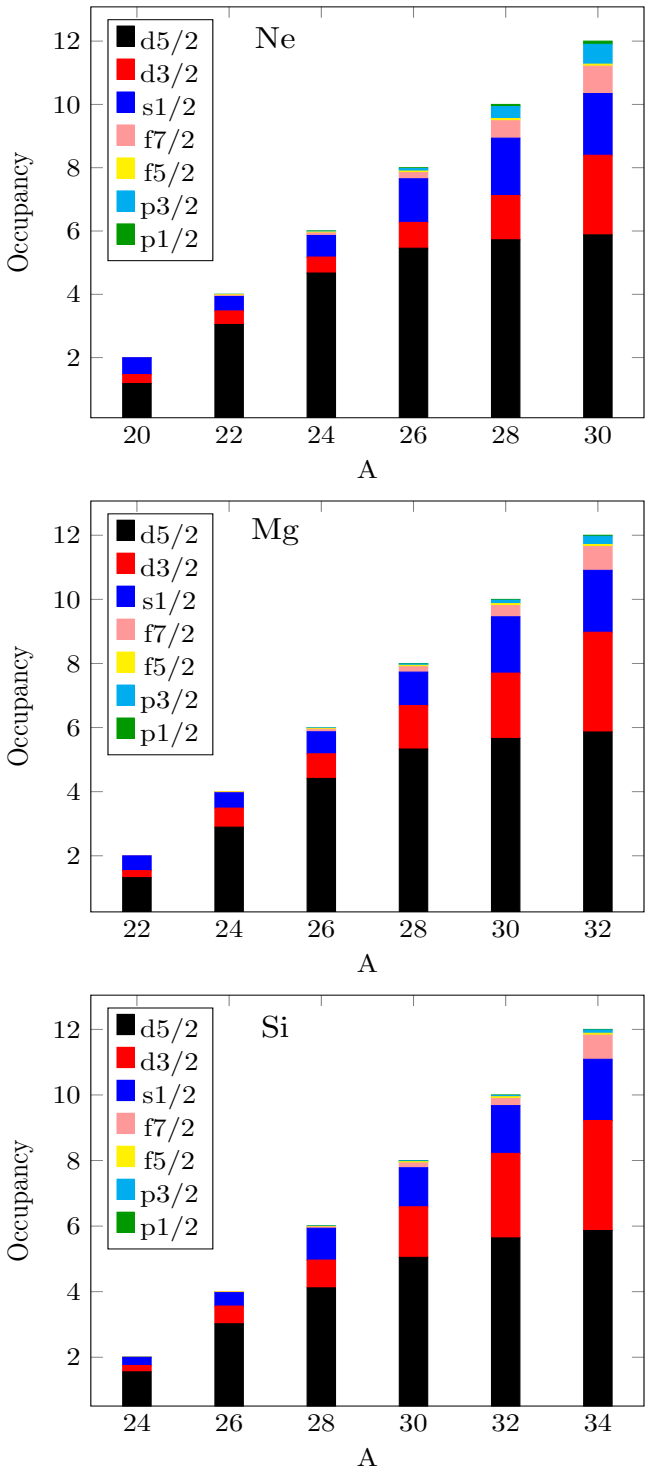

Figure 5.6: The neutron occupancy of 2_1^+ state for Ne, Mg and Si isotopes with SDPF-MU interaction with $2p-2h$ excitations .

5.5 Conclusions

In the present work using *ab initio* approaches, we have reported the quadrupole and magnetic moments for *sd* shell nuclei with the shell model [57]. We perform calculations with effective interactions derived from in-medium similarity renormalization and coupled-cluster approaches. Along with *ab initio* interactions, we have also compared these results with the phenomenological USDB interaction. The results show reasonable agreement with the available experimental data.

In the case of $B(E2)$ values for open shell nuclei with $10 \leq N \leq 20$ for Ne, Mg and Si isotopes, we have also performed calculations in the *sd* and $sd-pf$ spaces [157]. The results are also compared with the CEFT effective interaction based on chiral effective field theory in *sd* space. The degree of freedom of *sd* and *pf* shells are essential for the nuclei close to "island of inversion" so, we have also reported results of $sd-pf$ shell with SDPF-MU interaction. The results of *ab initio* interactions show reasonable agreement with the experimental data except at N =20. For nuclei in the island of inversion such as ^{30}Ne and ^{32}Mg, the admixture of *pf* shells is important to explain the lowering of the energies of 2_1^+ states and the enhancement of the $B(E2)$ values. The present study will add more information to earlier theoretical $B(E2)$ values of Ne, Mg and Si isotopes. This work will add more information to previously known spectroscopic properties of *sd* shell nuclei from *ab initio* approaches.

CHAPTER 6

AB INITIO CALCULATIONS FOR GAMOW-TELLER STRENGTHS IN THE *SD* SHELL

6.1 Introduction

The Gamow-Teller (GT) transitions are one of the important tools to explore the structure of atomic nuclei [158–167]. It has many applications, such as β-decay in stellar evolution and electron capture [168–171]; double electron capture for heating of stars [172] and neutrino nucleosynthesis [173–176]. There are two types of GT transitions: the GT_+ transition where a proton changes into a neutron, and the GT_- transition where a neutron changes into a proton. The experimental $B(GT)$ strengths can be obtained from β-decay studies, but the excitation energies are limited by the decay Q-values in this approach. On the other hand, with the charge exchange (CE) reactions, such as (p,n), (n,p), $(d,{}^2\mathrm{He})$ or $({}^3\mathrm{He},t)$, it is possible to access GT transitions at higher energies without the Q-value limitation. The experi-

mental measurements at scattering angles around 0° and incident energies above 100 MeV/nucleon provide valuable information on the GT transitions.

There are various experimental probes for the measurement of the GT strengths in *sd* shell nuclei in $A = 20 - 32$ mass region. For the GT_+ transition, the (n, p) and $(d,^2\mathrm{He})$ reactions are mainly used to obtain the strength distribution. The $(t,^3\mathrm{He})$ reaction is also an alternative tool. The GT transition strengths extracted from β-decay and CE reactions provide also important tests for *ab initio* calculations.

Modern *ab initio* approaches, like the IM-SRG [177], the coupled cluster theory [178] and the self-consistent Green's function method [179], have been established and provide accurate description of nuclear structure properties. The *ab initio* approaches are more fundamental, although in many cases empirical interactions still are used as benchmarks. The *ab initio* calculations can be used not only for spherical nuclei, but also to predict the ground- and excited-state energies and deformations for doubly-open-shell nuclei [20]. The yrast deformed states in ^{20}Ne and ^{24}Mg have been recently reported in Ref. [20].

The aim of the present study is to calculate the GT strengths for *sd* shell nuclei using *ab initio* approaches. In Table 6.1, we give a list of *sd* shell nuclei and corresponding types of reactions for which we perform the shell model calculations. Thus, the present work will add more information to earlier $B(GT)$ results for *sd* shell nuclei obtained by using phenomenological interactions. Previously, the $B(GT)$ strengths for $A = 10 - 13$ (p shell) nuclei, using the no-core shell model with two-nucleon (NN) and three-nucleon ($3N$) interactions derived from chiral effective field theory, were reported in Ref. [180]. Results for the GT strength in the $^7\mathrm{Be}(3/2^-_{g.s})$ $\rightarrow$ $^7\mathrm{Li}(3/2^-_{g.s},1/2^-_1)$ transition, obtained by using the no-core shell model with the Argonne V8′ NN potential and the Tucson-Melbourne TM′(99) $3N$ potential, were reported in Ref. [181].

Table 6.1: List of the GT transitions studied in this work. The data types available and the types of theoretical calculations used are given. In the last column are given the references for the data sets, which are used for comparison with the theoretical calculations.

S.No.	Initial	Final	$\beta-$decay	(n,p)	$(d,^2\mathrm{He})$	$(t,^3\mathrm{He})$	$(^3\mathrm{He},t)$	(p,n)	CCEI	IM-SRG	USDB	Ref.
1.	$^{20}\mathrm{Ne}(0^+)$	$^{20}\mathrm{F}(1^+)$		√					√	√	√	[182]
2.	$^{23}\mathrm{Na}(\frac{3}{2}^+)$	$^{23}\mathrm{Mg}(\frac{1}{2}^+,\frac{3}{2}^+,\frac{5}{2}^+)$					√		√	√	√	[183]
3.	$^{23}\mathrm{Na}(\frac{3}{2}^+)$	$^{23}\mathrm{Ne}(\frac{1}{2}^+,\frac{3}{2}^+,\frac{5}{2}^+)$		√					√	√	√	[184]
4.	$^{24}\mathrm{Mg}(0^+)$	$^{24}\mathrm{Na}(1^+)$			√	√			√	√	√	[185, 186]
5.	$^{24}\mathrm{Mg}(0^+)$	$^{24}\mathrm{Al}(1^+)$					√	√	√	√	√	[187, 188]
6.	$^{25}\mathrm{Mg}(\frac{5}{2}^+)$	$^{25}\mathrm{Al}(\frac{3}{2}^+,\frac{5}{2}^+,\frac{7}{2}^+)$					√		√	√	√	[189]
7.	$^{26}\mathrm{Mg}(0^+)$	$^{26}\mathrm{Na}(1^+)$			√	√			√	√	√	[190, 191]
8.	$^{26}\mathrm{Mg}(0^+)$	$^{26}\mathrm{Al}(1^+)$					√	√	√	√	√	[190, 192]
9.	$^{26}\mathrm{Si}(0^+)$	$^{26}\mathrm{Al}(1^+)$	√						√	√	√	[193]
10.	$^{27}\mathrm{Al}(\frac{5}{2}^+)$	$^{27}\mathrm{Si}(\frac{3}{2}^+,\frac{5}{2}^+,\frac{7}{2}^+)$					√		√	√	√	[194]
11.	$^{28}\mathrm{Si}(0^+)$	$^{28}\mathrm{P}(1^+)$					√	√	√	√	√	[187, 195]
12.	$^{31}\mathrm{P}(\frac{1}{2}^+)$	$^{31}\mathrm{Si}(\frac{1}{2}^+,\frac{3}{2}^+)$		√					√	√	√	[196]
13.	$^{32}\mathrm{S}(0^+)$	$^{32}\mathrm{P}(1^+)$			√				√	√	√	[197]

In the present work to describe the measured GT strength distribution of *sd* shell nuclei we performed shell model calculations with *ab initio* interactions with two modern *ab initio* approaches: in-medium similarity renormalization (IM-SRG) and coupled-cluster effective interaction (CCEI). Along with *ab initio* calculations, we have also performed calculations with a phenomenological USDB effective interaction. For the diagonalization of matrices we used the shell model code NuShellX. More deatils about IM-SRG and CCEI are given in chapter 5.

6.2 Gamow-Teller $B(GT)$ strength

The Gamow-Teller strength $B(GT)$ is calculated using the following expression,

$$B(GT_{\pm}) = \frac{1}{2J_i+1} f_q^2 \, |\langle f|| \sum_k \sigma^k \tau_{\pm}^k ||i\rangle|^2, \tag{6.1}$$

where $\tau_+|p\rangle = |n\rangle$, $\tau_-|n\rangle = |p\rangle$, the index k runs over the single particle orbitals, and $|i\rangle$ and $|f\rangle$ describe the state of the parent and daughter nuclei, respectively. In the present work we have taken the value of quenching factor as $f_q = 0.77$ [91, 198]. To support our choice above, we show the calculated quenching factors for $T = 1/2$ *sd* shell nuclei with $A = 17 - 39$ [199] using the three different interactions in Fig. 6.1. These quenching factors are obtained by a chi-square fit of the theoretical GT transition strengths to the corresponding experimental strengths. Note that the IM-SRG interaction and corresponding theoretical transition strengths are available up to $A = 34$. We can see that the quenching factors obtained are 0.79, 0.78 and 0.81 for the USDB, CCEI and IM-SRG interactions, respectively. Although these values show a slight dependence on the interaction, in this work we adopt $f_q = 0.77$ for all three interactions, because this is more consistent with the value $f_q = 0.764 \pm 0.013$ obtained for USDB in Ref. [91], where more data have been used for the fitting. With this choice $f_q = 0.77$, the rms deviations from the experimental values are 0.088, 0.177 and 0.149 for USDB, CCEI and IM-SRG interactions, respectively. Compared with

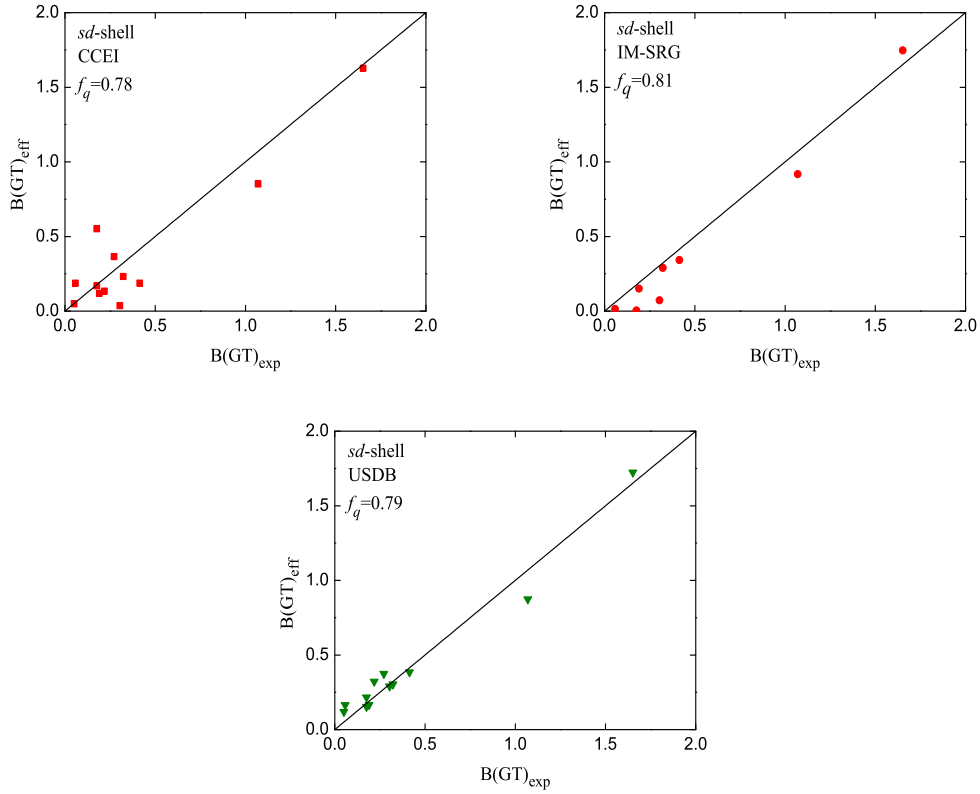

Figure 6.1: The calculated value of quenching factor for GT transitions in $T = 1/2$ *sd* shell mirror nuclei with $A = 17 - 39$ ($A = 17 - 33$) using CCEI and USDB (IM-SRG) effective interactions.

the USDB case, the enhancement of the rms deviations for CCEI and IM-SRG is qualitatively similar to the deviations for the energy levels [11, 20]. In the case of IM-SRG, the calculated $B(GT)$ values are very small and the deviations from the experimental values become large for higher mass nuclei with $A \geq$27. In the case of CCEI, large deviations are also seen in several nuclei with higher mass, $A = 31$, 27, 25 and 33 with descending order of magnitude. This tendency may be attributed to the increasing number of three-valence-nucleon combinations interacting via $3N$ forces [20], which we neglected in our calculation.

In the present work we have also checked the Ikeda sum rule $[B(GT_-) - B(GT_+) = 3(N - Z)]$ for $A = 23$, 24 and 26. Both *ab intio* interactions used in the IM-SRG and CCEI methods satisfy this sum rule, as does the phenomenological USDB interaction. Thus we are confident that sufficient excited states are taken into account in the calculation of GT strengths for *sd* shell nuclei in the two *ab initio* calculations.

6.3 Comparison of the experimental and theoretical GT-strength distributions

In this section we compare the theoretical results with the experimental data.

6.3.1 ^{20}Ne $\rightarrow$ ^{20}F

In Fig. 6.2, we compare the $B(GT)$ strength distribution obtained from the two *ab initio* effective interactions CCEI (Fig. 6.2 (b)) and IM-SRG (Fig. 6.2 (c)) and the phenomenological USDB (Fig. 6.2 (d)) interaction with the experimental data for the transition ^{20}Ne $\rightarrow$ ^{20}F. The $B(GT)$ values for these transitions are known from Ref. [182], where the data is obtained from the reaction ^{20}Ne(n,p)^{20}F up to the excitation energy E_x=10 MeV of ^{20}F. On the horizontal axis the excitation energies of different 1^+ states of ^{20}F are shown. In the experimental data the $B(GT)$ strength is spread over a wide range of excitation energies of ^{20}F. The theoretical calculations for the $B(GT)$ strength have already been done [182] in the framework of the shell model using the universal *sd* shell (SD) interaction of Wildenthal [200]. All three interactions used here give the strongest peak around the excitation energy $\sim$ 1 MeV, and other strong peaks are observed around excitation energies $\sim$ 4 MeV and $\sim$ 8 MeV. The other peaks are small in strength. In Fig. 6.2 (c), the strongest peak is observed around the excitation energy $\sim$ 1 MeV, but the strength is less than that of the strongest peak in the CCEI. The USDB interaction also shows the strongest peak at $\sim$ 1 MeV, but its strength is smaller than that obtained with both *ab initio* interactions. In the experimental data shown in Fig. 6.2 (a), a wide spread of the $B(GT)$ strength distribution is observed in the energy range 6-7 MeV and 8-9 MeV. However, theoretically very small $B(GT)$ strength is obtained in the energy range 6-7 MeV. All three interactions also show zero strength in the energy range 2-3 MeV. From Figs. 6.2(b)-6.2(d), it is clear that, as we go towards higher excitation energy, the $B(GT)$ strength decreases and then increases again at the excitation

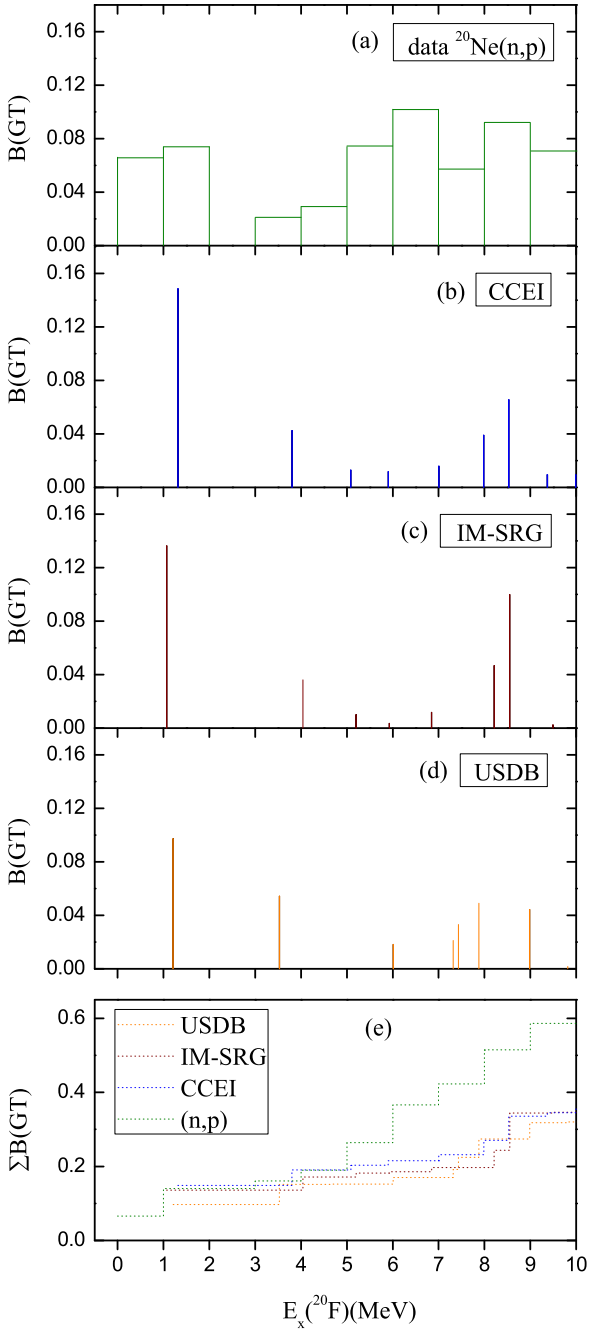

Figure 6.2: Comparison of the experimental and theoretical $B(GT)$ distributions for ^{20}Ne $\rightarrow$ ^{20}F.

energy around 8-9 MeV. All three interactions give the g.s. 2^+ for ^{20}F, in agreement with the experiment. In Fig. 6.2(e), the accumulated sums of $B(GT)$ are shown as a function of excitation energy of ^{20}F. The CCEI gives better results compared with the other interactions. The summed $B(GT)$ values at higher excitation energies are lower than the experimental data for all three interactions used here. The small calculated $B(GT)$ values in comparison with the experimental values at $E_x > 5$ MeV can be attributed to the limitation of the configuration space within the *sd* shell. The breaking of ^{16}O core is important for the fragmentation of the GT strength. Shell model calculations can be performed in *p-sd* model space to include the $B(GT)$ strength beyond $E_x > 10$ MeV. ^{20}Ne is a well deformed nucleus and has admixtures of *g*-shell components [201]. We should also keep in mind that the experimental data have rather large errors; as large as 0.209 for the sum of $B(GT)$ [182].

6.3.2 ^{23}Na $\rightarrow$ ^{23}Mg

Figure 6.3 shows the experimental and theoretical $B(GT)$ strength distributions for the transition ^{23}Na $\rightarrow$ ^{23}Mg. Here, the experimental data is available from the ^{23}Na(^{3}He,t)^{23}Mg reaction [183]. In this reaction the $B(GT)$ transitions were measured at the incident energy of 140 MeV per nucleon with the energy resolution of 45 keV. The ^{23}Na and ^{23}Mg are deformed nuclei with the static quadrupole moments 10.1 ± 0.2 fm^2 [202] and 11.4 ± 0.3 fm^2 [203], respectively. These nuclei are important from an astrophysical point of view. In Fig. 6.3 (a) the experimental data are shown up to the excitation energy 11.132 MeV of ^{23}Mg. In Ref. [183], the strength of the first transition (^{23}Na($\frac{3}{2}^+$) $\rightarrow$ ^{23}Mg($\frac{3}{2}^+$)) is 0.340, which is the mixture of $B(GT)$ and Fermi transition strength. We have excluded the Fermi transition strength. Now, the $B(GT)$ transition strength is 0.09. The largest $B(GT)$ strength is at the excitation energy 8.168 MeV. Figure 6.3 (b) shows the $B(GT)$ strength obtained in the CCEI. The CCEI gives a strong peak at the excitation energy 5.637 MeV, and the magnitude of strength is also comparable with the strongest peak observed in the

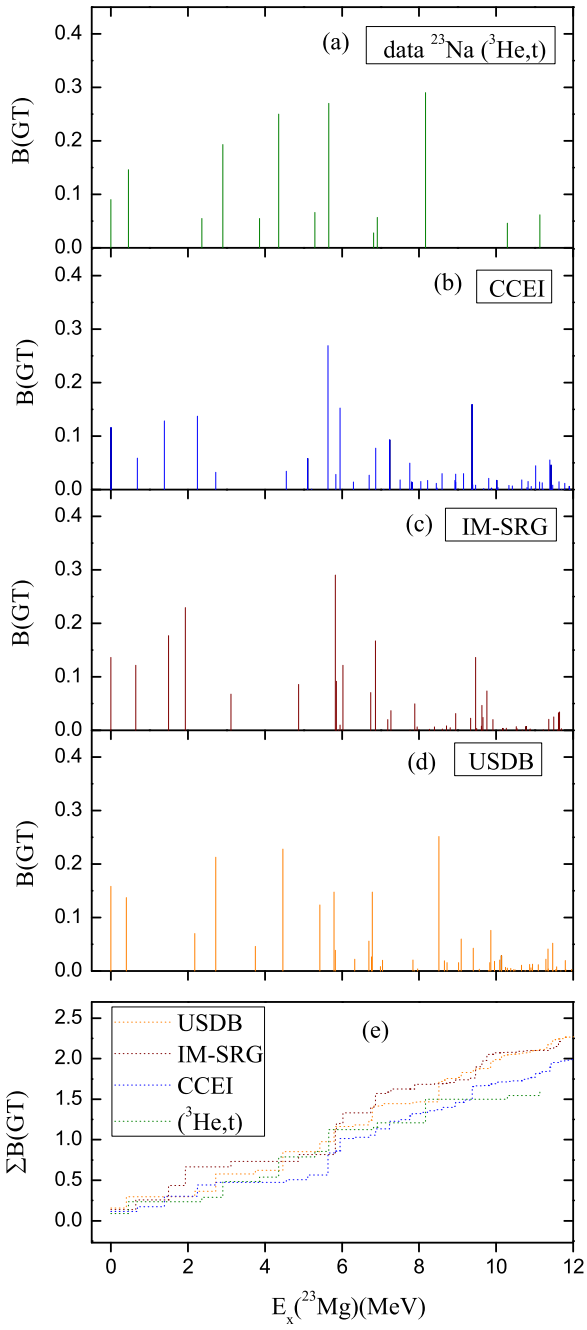

Figure 6.3: Comparison of the experimental and theoretical $B(GT)$ distributions for ^{23}Na $\rightarrow$ ^{23}Mg.

experiment. This peak comes from the transition $^{23}\mathrm{Na}(\frac{3}{2}^{+}_{1}) \rightarrow {}^{23}\mathrm{Mg}(\frac{5}{2}^{+}_{4})$. In the energy range 6-12 MeV, we see many $B(GT)$ transitions which are not observed in the experiment. Figure 6.3 (c) shows results of the IM-SRG interaction. The IM-SRG interaction gives the strongest peak of the $B(GT)$ strength at the excitation energy 5.826 MeV, and its strength is comparable with the strength of the strongest peak obtained with the CCEI and observed in the experiment. The density of peaks is smaller for the IM-SRG interaction compared with the CCEI. In Fig. 6.3 (d), we see the strongest peak at the excitation energy 8.513 MeV. All three interactions give the g.s. $\frac{3}{2}^{+}$ for ^{23}Mg, in agreement with the experimentally observed g.s. The distribution of accumulated sums of $B(GT)$ for the experimental data and the theoretical calculations is shown in Fig. 6.3 (e). The CCEI and USDB interactions show similar trends for the summed $B(GT)$. The IM-SRG interaction gives larger values for the summed $B(GT)$ strengths than the CCEI or the experiment.

6.3.3 $^{23}\mathrm{Na} \rightarrow {}^{23}\mathrm{Ne}$

In Fig. 6.4 (a) is shown the experimental $B(GT)$ strength distribution for the transition $^{23}\mathrm{Na} \rightarrow {}^{23}\mathrm{Ne}$ [184], observed in the charge exchange reaction $^{23}\mathrm{Na}(n,p)^{23}\mathrm{Ne}$. Previously, the shell model results for $B(GT)$ distribution were shown in Ref. [184], and in the present work we show the calculations obtained by using the recent phenomenological USDB interaction in comparison with the *ab initio* effective interactions. The experimental $B(GT)$ strength (Fig. 6.4 (a)) is dominated in the excitation energy-range 3.432-3.458 MeV. The other peaks outside this range have very small $B(GT)$ values. With the CCEI (Fig. 6.4 (b)), we get the strongest peak at the excitation energy 3.170 MeV, but its strength is approximately three times less than the experimental value. We also see some other peaks with $B(GT)$ values below 0.1. In the IM-SRG approach (Fig. 6.4 (c)), we get two peaks with strengths larger than 0.1. In Fig. 6.4 (d), the $B(GT)$ distribution is shown for the USDB interaction. We see the strongest peak at the excitation energy 3.508 MeV. All strong peaks in

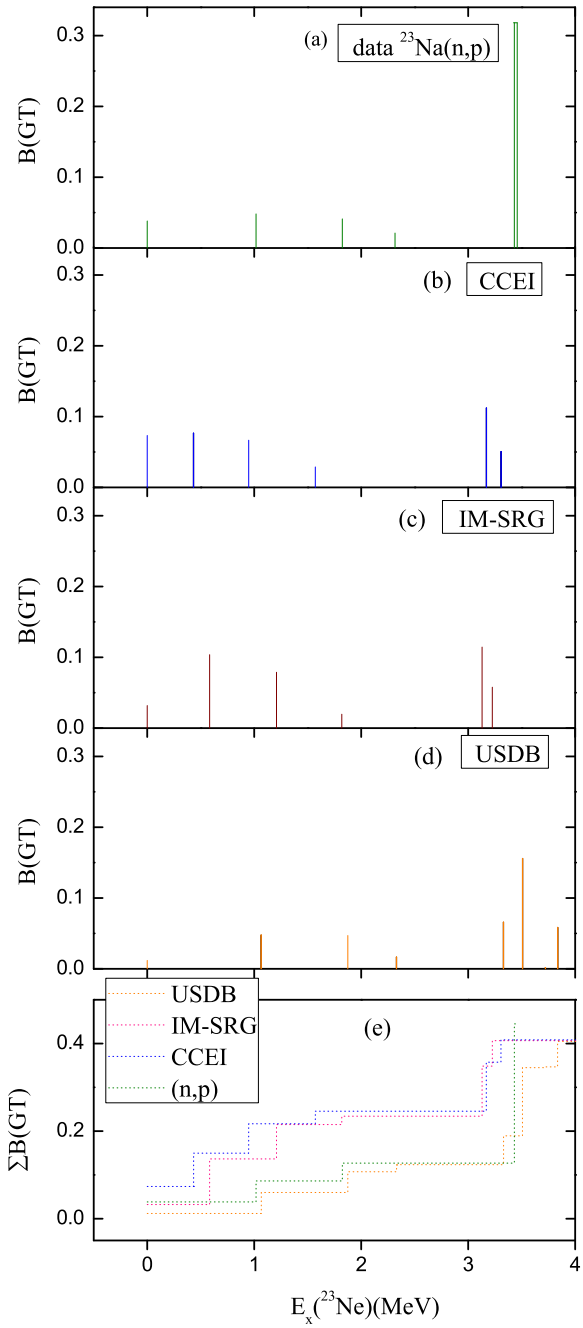

Figure 6.4: Comparison of the experimental and theoretical $B(GT)$ distributions for ^{23}Na $\rightarrow$ ^{23}Ne .

the theoretical calculations correspond to the transition ^{23}Na($\frac{3}{2}^+_1$)$\rightarrow$ ^{23}Ne($\frac{1}{2}^+_2$). All three interactions give the g.s. $\frac{5}{2}^+$ for ^{23}Ne, in agreement with the experiment. The summed $B(GT)$ values (Fig. 6.4 (e)) obtained with USDB show a similar trend as the experimental values up to the excitation energy 3.5 MeV. The theoretical $B(GT)$ strength is generally lower than the experimental one.

6.3.4 ^{24}Mg $\rightarrow$ ^{24}Na

Figure 6.5 shows the $B(GT)$ strength distribution obtained from the shell model calculations, and the experimental data for the transition ^{24}Mg $\rightarrow$ ^{24}Na. There are two experimental data for the $B(GT)$ distribution available from the ^{24}Mg(t,^{3}He)^{24}Na and ^{24}Mg(d,^{2}He)^{24}Na reactions. The ^{24}Mg(t,^{3}He)^{24}Na reaction was performed at the energy of 115 MeV per nucleon by using a secondary triton beam with an energy resolution of about 200 keV [185]. The ^{24}Mg(d,^{2}He)^{24}Na reaction was performed at the energy of 170 MeV, and a good resolution of the order of 145 keV was obtained in this reaction [186] . The shell model calculations with the phenomenological interactions USDA and USDB have already been performed [185]. Figure 6.5 (a) shows the data from ^{24}Mg(t,^{3}He)^{24}Na reaction. In this case, we see the strongest peak at the excitation energy 1.346 MeV of ^{24}Na. We also find that the distribution of the $B(GT)$ strength is in the energy windows from 3.14-3.94 MeV and 6.5-7.1 MeV for this reaction. Figure 6.5 (b) shows the experimental information for the $B(GT)$ distribution from ^{24}Mg(d,^{2}He)^{24}Na reaction. This reaction gives the strongest peak at the excitation energy 1.35 MeV with nearly the same $B(GT)$ value as obtained from the ^{24}Mg(t,^{3}He)^{24}Na reaction. Some other peaks are also observed with less strength. Figure 6.5 (c) shows the $B(GT)$ distribution obtained with the CCEI. The CCEI predicts 1^+ as the g.s. of ^{24}Na, while the g.s. from the experiment is 4^+. In Fig. 6.5 (c) we see the strongest peak at the excitation energy of 0.417 MeV, which comes from the transition ^{24}Mg(0^+) $\rightarrow$ ^{24}Na(1^+_2). The $B(GT)$ distribution obtained with the IM-SRG interaction is shown in Fig. 6.5 (d). The IM-SRG interaction gives the

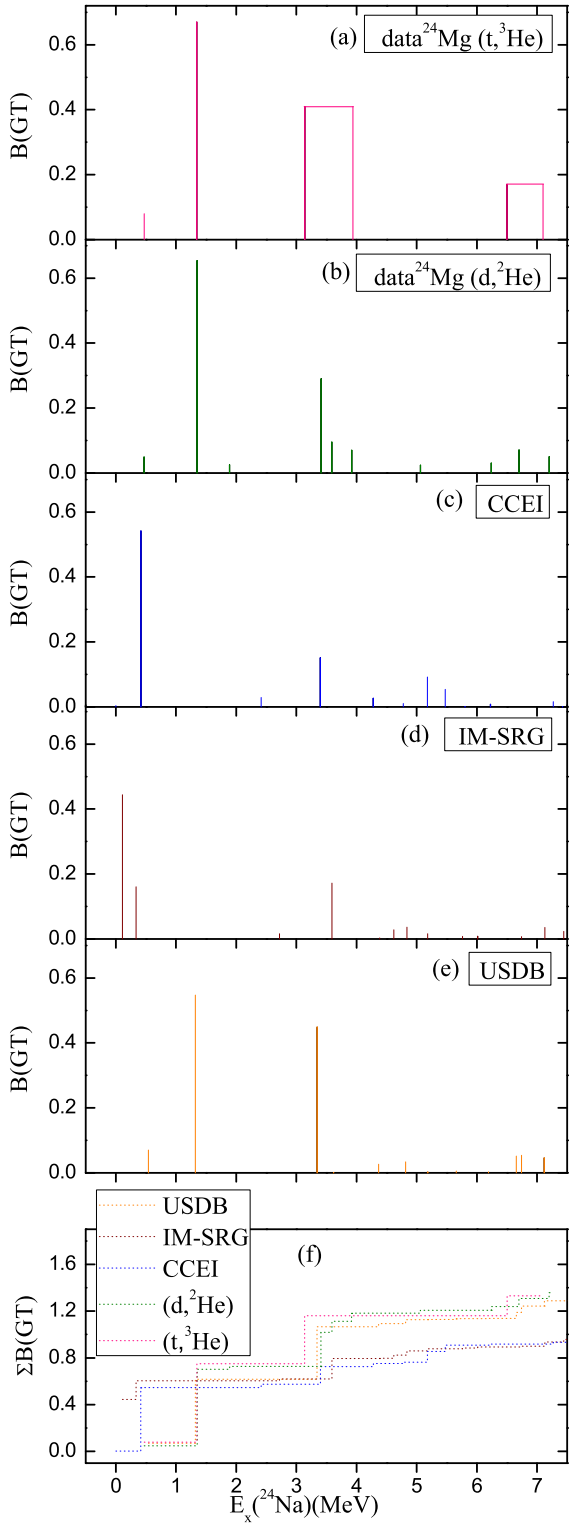

Figure 6.5: Comparison of the experimental and theoretical $B(GT)$ distributions for ^{24}Mg $\rightarrow$ ^{24}Na.

g.s. of ^{24}Na as 2^+. With this interaction we get the strongest peak at the excitation energy 0.110 MeV, which comes from the transition ^{24}Mg(0^+) $\rightarrow$ ^{24}Na(1^+_1). Figure 6.5 (e) shows the $B(GT)$ distribution obtained with the phenomenological USDB interaction. Here we see the strongest peak at the excitation energy 1.323 MeV and the next strongest peak at 3.345 MeV, which come from the transitions ^{24}Mg(0^+) $\rightarrow$ ^{24}Na(1^+_2) and ^{24}Mg(0^+) $\rightarrow$ ^{24}Na(1^+_3), respectively. Figure 6.5 (f) shows the trend of the accumulated sums of the $B(GT)$ distribution obtained from the experimental data and the theoretical calculations. The USDB interaction gives a similar trend as the experimental data for both reactions.

6.3.5 ^{24}Mg $\rightarrow$ ^{24}Al

The experimental information on the $B(GT)$ strength distribution for the transition ^{24}Mg $\rightarrow$ ^{24}Al is available from the ^{24}Mg(^{3}He,t)^{24}Al reaction observed at 420 MeV [188], and the ^{24}Mg(p,n)^{24}Al reaction observed at 136 MeV [187]. The results of the shell model calculation for the $B(GT)$ strength have been previously reported in Ref. [188], where the phenomenological interactions USDA and USDB were employed. Figure 6.6 (a) shows the data from the ^{24}Mg(^{3}He,t)^{24}Al reaction. We see the strongest peak at the excitation energy 1.090 MeV, and the next strongest peak at 3.001 MeV. Other peaks are also observed with less strengths. Figure 6.6 (b) shows the data from the ^{24}Mg(p,n)^{24}Al reaction. In this reaction the strongest peak is observed at the excitation energy 1.07 MeV, and the next strongest peak at 2.98 MeV. In Fig. 6.6 (c) the theoretical $B(GT)$ distribution, obtained by using the CCEI, is shown. The CCEI gives the g.s. 2^+ for ^{24}Al, whereas the experimental g.s. is 4^+. The CCEI gives the strongest peak at the excitation energy 0.615 MeV, which comes from the transition ^{24}Mg(0^+)$\rightarrow$ ^{24}Al (1^+_2). The second strongest peak is observed at the excitation energy 3.205 MeV. In Fig. 6.6 (d) the theoretical $B(GT)$ distribution is shown with the IM-SRG interaction. The IM-SRG interaction gives g.s. as 2^+ for ^{24}Al. The IM-SRG interaction gives the strongest peak at the excitation energy 0.077

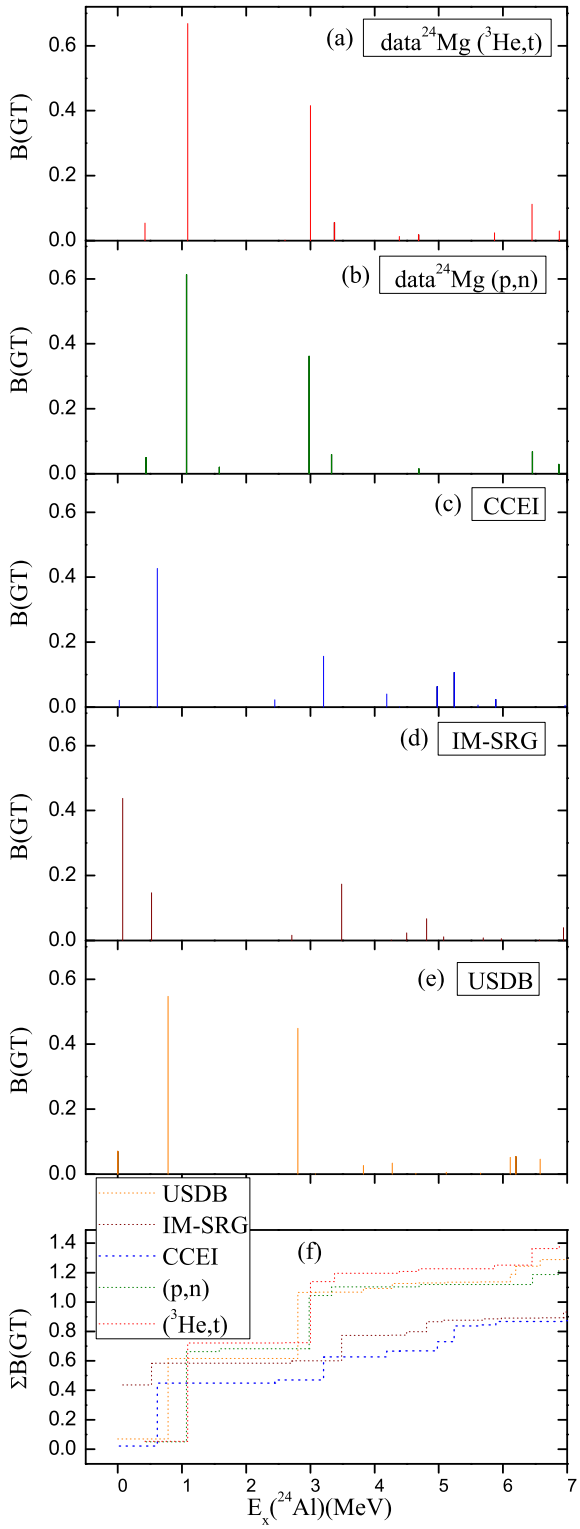

Figure 6.6: Comparison of the experimental and theoretical $B(GT)$ distributions for ^{24}Mg $\rightarrow$ ^{24}Al.

MeV which comes from the transition ^{24}Mg(0^+)$\rightarrow$ ^{24}Al (1^+_1). The second strongest peak is observed at the excitation energy 3.486 MeV. Figure 6.6 (e) shows the theoretical $B(GT)$ distribution obtained with the USDB interaction. The USDB interaction gives the strongest peak at 0.783 MeV which comes from the transition ^{24}Mg(0^+)$\rightarrow$ ^{24}Al (1^+_2), and the second strongest peak at 2.805 MeV. The USDB interaction gives the g.s. 4^+ for ^{24}Al, in agreement with the experiment. The summed $B(GT)$ strength distribution is shown up to the excitation energy 7 MeV. The USDB interaction gives a reasonable agreement with the experimental data, while the results from *ab initio* interactions show smaller strength in comparison with the experiment.

6.3.6 ^{25}Mg $\rightarrow$ ^{25}Al

The $B(GT)$ strength distribution for the transition ^{25}Mg $\rightarrow$ ^{25}Al is shown in Fig. 6.7 (a). This distribution has been measured via the ^{25}Mg(^{3}He,t)^{25}Al reaction at the energy of 140 MeV per nucleon [189]. The ^{25}Mg and ^{25}Al nuclei are known to be strongly deformed, and the states of these mirror nuclei are well described in terms of the particle rotor model [189]. In the experiment, the $B(GT)$ strength from the transition ^{25}Mg($\frac{5}{2}^+_1$) to ^{25}Al($\frac{5}{2}^+_1$) is dominant, while the other $B(GT)$ strengths are very much suppressed. The explanation of the suppression of $B(GT)$ transitions in $A = 25$ system is given on the basis of the selection rules of the K quantum number in rotational bands, and also assuming the usual selection rule $\triangle J^\pi$=1^+ for the $B(GT)$ operator. Most of the observed $B(GT)$ transition strength is very small and less reliable; see Ref. [189]. In particular, it is very weak in the $\sim$ 2 - 6 MeV energy range. In Fig. 6.7 (b), which shows the theoretical results obtained by using the CCEI approach, we see a considerable amount of $B(GT)$ strength in the 2 - 6 MeV range. This method gives two dominant peaks at excitation energies 0.474 MeV and 1.847 MeV with smaller $B(GT)$ values than the experiment. The first peak comes from the transition ^{25}Mg($\frac{5}{2}^+_1$) to ^{25}Al($\frac{5}{2}^+_1$), and the second one comes from ^{25}Mg($\frac{5}{2}^+_1$) to ^{25}Al($\frac{7}{2}^+_1$). In Fig. 6.7 (c), which shows the results for the IM-SRG, we see a peak

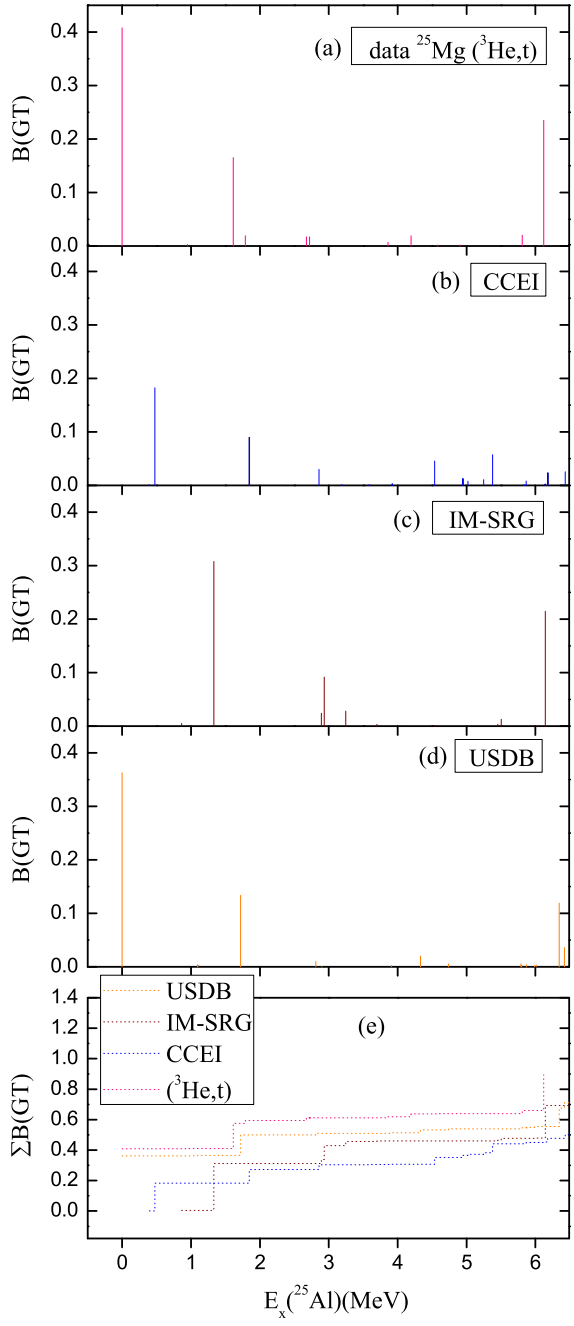

Figure 6.7: Comparison of the experimental and theoretical $B(GT)$ distributions for ^{25}Mg $\rightarrow$ ^{25}Al.

as in the experiment around ~ 6 MeV. The strength distribution calculated with the IM-SRG interaction gives the first dominant peak at higher energy in comparison with the experiment. Figure 6.7 (d) shows the $B(GT)$ strength distribution obtained with the USDB interaction. The first two peaks show a reasonable agreement with experiment. Above the excitation energy 6 MeV, we see a peak with smaller magnitude in comparison with experiment. The accumulated sums from the theoretical calculations and experimental data are shown in Fig. 6.7 (e). The USDB results agree reasonably well with experiment, compared with the *ab initio* interactions.

6.3.7 ^{26}Mg $\rightarrow$ ^{26}Na

The $B(GT)$ strength distribution for the transition ^{26}Mg $\rightarrow$ ^{26}Na is shown in Fig. 6.8. Figure 6.8 (a) shows the distribution observed with the ^{26}Mg(t,^{3}He)^{26}Na reaction at the energy of 115 MeV per nucleon [190]. From the experimental data for ^{26}Mg(t,^{3}He)^{26}Na, we see the most intense peak at the excitation energy 0.08 MeV of ^{26}Na. Figure 6.8 (b) shows the experimental information from the ^{26}Mg(d,^{2}He)^{26}Na reaction. This reaction also shows a strong peak at the excitation energy 0.08 MeV. The $B(GT)$ strengths from the ^{26}Mg(d,^{2}He)^{26}Na data are smaller in magnitude than those from the ^{26}Mg(t,^{3}He)^{26}Na data. Figure 6.8 (c) shows the distribution obtained with the CCEI approach. This method gives the g.s. of ^{26}Na as 2^+, whereas the experimental g.s. is 3^+. With the CCEI, a strong peak is observed at the excitation energy 3.894 MeV. Figure 6.8 (d) shows the theoretical calculations obtained with the IM-SRG interaction. From this figure we see the strongest peak at zero excitation energy, but the strength of this transition is less than half of the strength observed for the strongest peak in the experiment. Other calculated strengths are also weak in comparison with both the experimental data. The IM-SRG interaction gives 1^+ as the g.s. of ^{26}Na. Figure 6.8 (e) shows the distribution obtained with the USDB interaction. It shows a strong peak which is comparable with both experimental data. The USDB interaction gives 3^+ as the g.s. of ^{26}Na, in agreement with experiment.

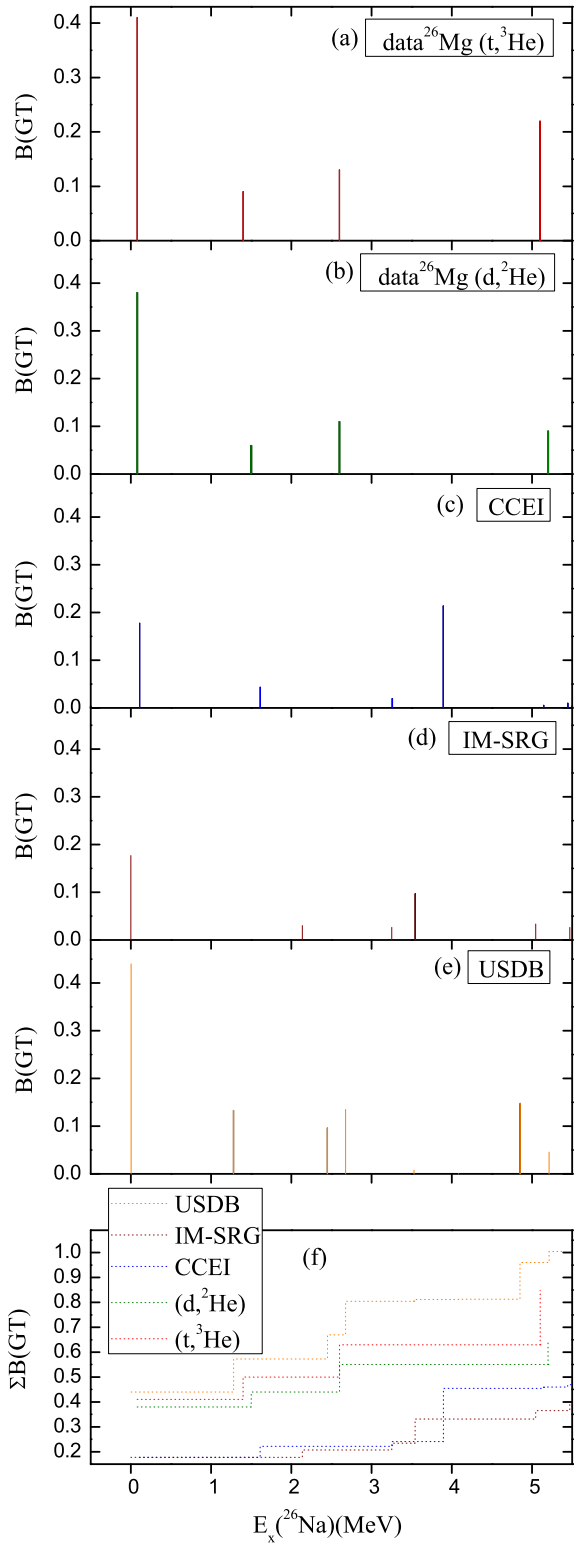

Figure 6.8: Comparison of the experimental and theoretical $B(GT)$ distributions for ^{26}Mg $\rightarrow$ ^{26}Na.

The accumulated sums are shown in Fig. 6.8 (f). The results obtained from the USDB interaction are much better than the *ab initio* interactions.

6.3.8 ^{26}Mg $\rightarrow$ ^{26}Al

Figure 6.9 shows the GT strength distribution for the transition from ^{26}Mg $\rightarrow$ ^{26}Al. Information on the $B(GT)$ strength is available from the ^{26}Mg(^{3}He,t)^{26}Al [190] (Fig. 6.9 (a)) and ^{26}Mg$(p,n)^{26}$Al [192] (Fig. 6.9 (b)) reactions. The ^{26}Mg(^{3}He,t)^{26}Al reaction was observed at 140 MeV/nucleon with an energy resolution of 100 keV. In Fig. 6.9 (c) the results obtained by using the CCEI are shown. In this case we see a strong transition at the excitation energy 3.498 MeV of ^{26}Al, which comes from the transition ^{26}Mg $(0^+) \rightarrow$ ^{26}Al (1^+_5). The CCEI gives the g.s. 3^+ for ^{26}Al, while the experimental g.s. is 5^+. Figure 6.9 (d) shows the $B(GT)$ strength distribution using the IM-SRG interaction. In this case we see a strong peak at the excitation energy 1.849 MeV, which comes from the transition ^{26}Mg $(0^+) \rightarrow$ ^{26}Al (1^+_4). The IM-SRG interaction gives g.s. 1^+ for ^{26}Al. In Fig. 6.9 (e) is shown the $B(GT)$ strength distribution obtained by using the phenomenological interaction USDB. This interaction gives a strong peak at the excitation energy 1.034 MeV, which comes from the transition ^{26}Mg $(0^+) \rightarrow$ ^{26}Al (1^+_1). The USDB interaction gives the 5^+ g.s. for ^{26}Al, in agreement with the experiment. Figure 6.9 (f) shows the accumulated sums of $B(GT)$ strength for the theoretical calculations and the experimental data. The IM-SRG and USDB interactions show almost the same trend as the experimental data, while the CCEI interaction gives lower values.

6.3.9 ^{26}Si $\rightarrow$ ^{26}Al

The experimental and theoretical information on the $B(GT)$ strength distribution for the transition ^{26}Si $\rightarrow$ ^{26}Al is shown in Fig. 6.10. In Fig. 6.10 (a) is shown the experimental data from β- decay [193]. We see a strong peak at the excitation energy 1.0577 MeV of ^{26}Al. The experimental data are very sparse. Only four peaks

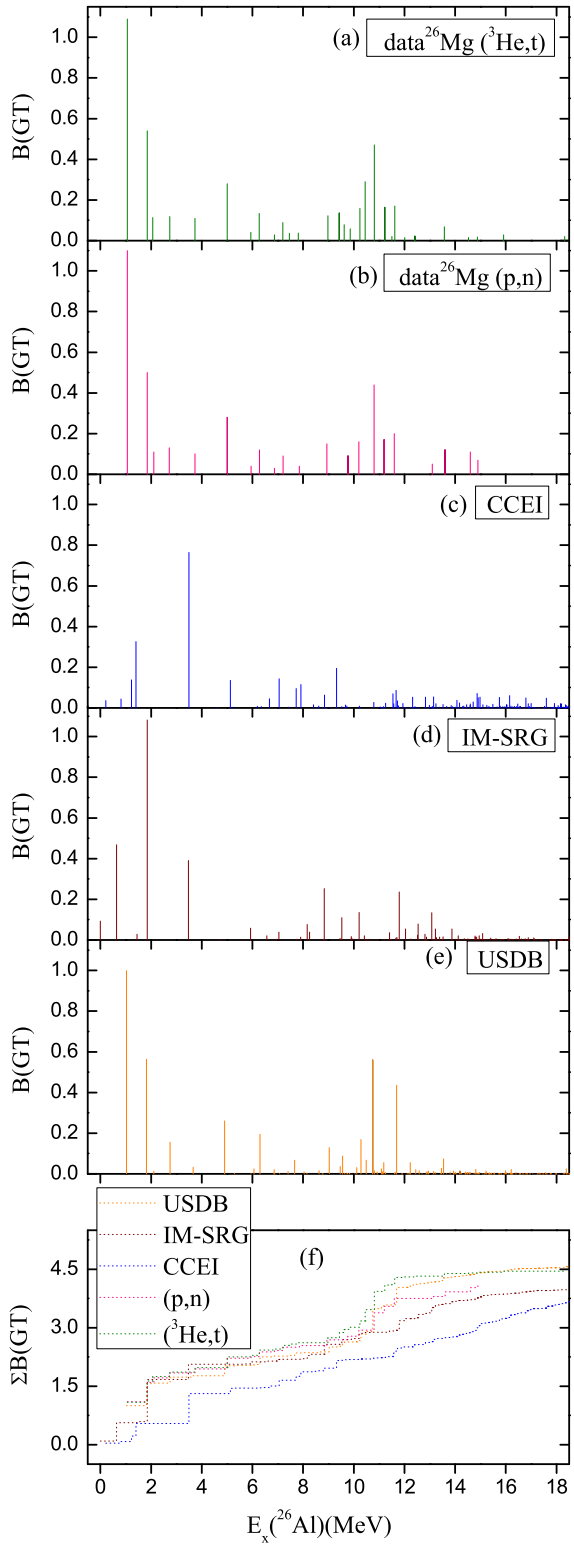

Figure 6.9: Comparison of the experimental and theoretical $B(GT)$ distributions for ^{26}Mg $\rightarrow$ ^{26}Al.

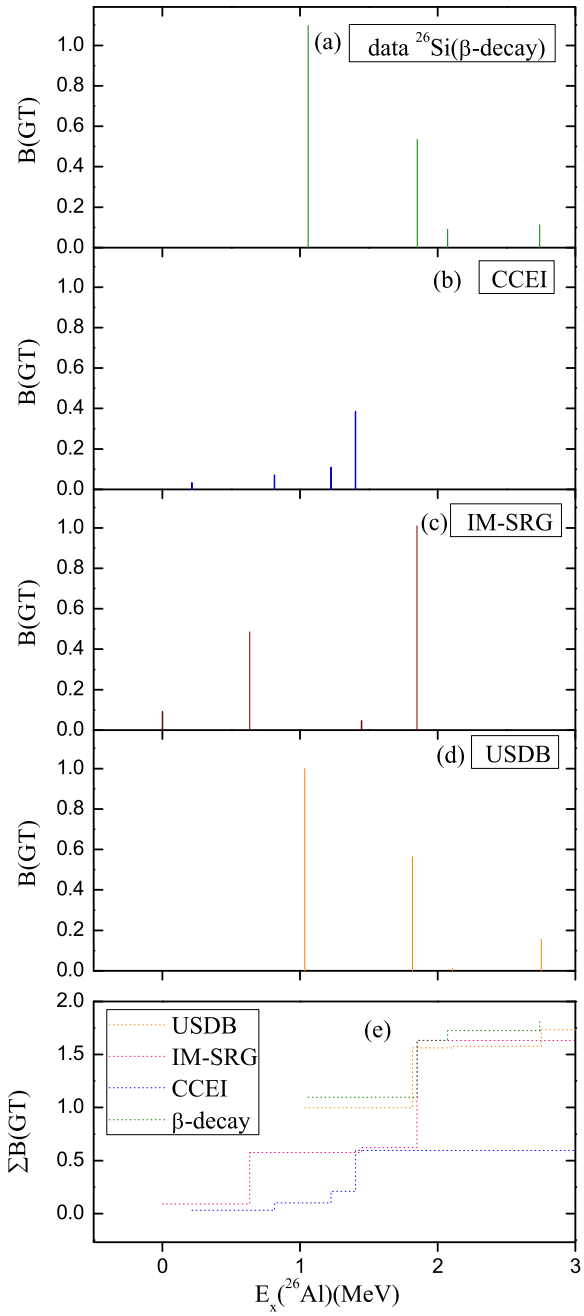

Figure 6.10: Comparison of the experimental and theoretical $B(GT)$ distributions for ^{26}Si $\rightarrow$ ^{26}Al.

are observed up to the excitation energy 3 MeV of ^{26}Al. In Fig. 6.10 (b), the theoretical $B(GT)$ strength distribution obtained by using the CCEI is shown. It gives a strong peak at the excitation energy 1.403 MeV. The strength of this peak is smaller in comparison with the strongest peak from the experimental data. The CCEI gives 3^+ as the g.s. of ^{26}Al, whereas the experimental g.s. is 5^+. Figure 6.10 (c) shows the $B(GT)$ strength distribution for the IM-SRG interaction. We get a strong peak at the excitation energy 1.849 MeV. The strength of this peak is comparable with the experimental data. The IM-SRG interaction gives 1^+ g.s. for ^{26}Al. Figure 6.10 (d) shows the $B(GT)$ strength distribution from the USDB interaction. The USDB interaction gives a strong peak at the excitation energy 1.034 MeV. The results from the USDB interaction are in better agreement with the experimental data, compared with both *ab initio* interactions. The USDB interaction gives 5^+ g.s. for ^{26}Al, in agreement with the experiment. Figure 6.10 (e) shows the accumulated sums of $B(GT)$ strengths for the experimental data and the theoretical calculations. The summed $B(GT)$ strength from the USDB interaction matches well with the experimental data, whereas the IM-SRG interaction shows the same trend after the excitation energy 2 MeV. The CCEI gives lower values in comparison with the experimental data.

6.3.10 ^{27}Al $\rightarrow$ ^{27}Si

The nuclei ^{27}Si and ^{27}Al are T=1/2 mirror nuclei. The information on the $B(GT)$ strength distribution for the transition ^{27}Al $\rightarrow$ ^{27}Si is given in Ref. [194]. For these transitions only one experimental data set is available from the reaction ^{27}Al(^{3}He,t)^{27}Si, which was performed at 150 MeV/nucleon and at scattering angle 0°. The $B(GT)$ strength distribution up to the excitation energy 9.95 MeV is shown in Fig. 6.11 (a). In the experimental data, the strength of the transition $^{27}\mathrm{Al}(\frac{5}{2}^+_1) \rightarrow {}^{27}\mathrm{Si}(\frac{5}{2}^+_1)$ is larger than the other $B(GT)$ strengths [At $E_x(^{27}\mathrm{Si})$= 0.0 MeV, this strength is obtained by removing the Fermi transition strength]. The experimental $B(GT)$ strength at the

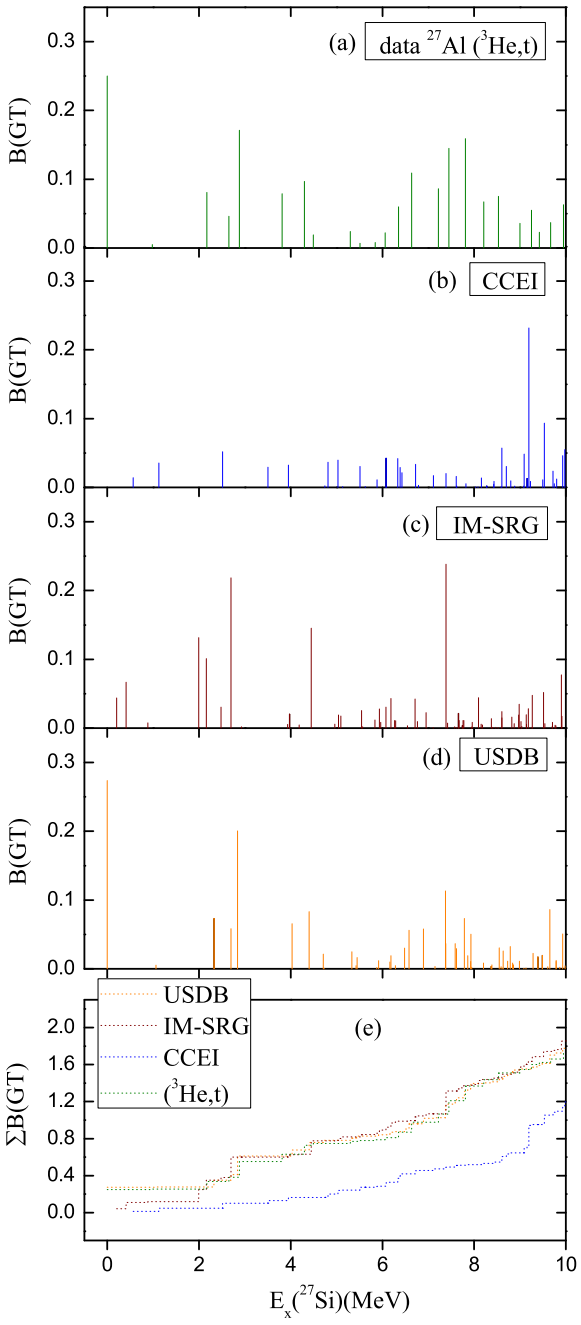

Figure 6.11: Comparison of the experimental and theoretical $B(GT)$ distributions for $^{27}\mathrm{Al} \rightarrow {}^{27}\mathrm{Si}$.

excitation energies 0.98, 5.51 and 5.84 MeV are not very reliable, and those at 4.49, 5.30 and 6.06 MeV are less reliable [194]. Figure 6.11 (b) shows the results obtained with the CCEI. At lower energies, the $B(GT)$ strength distribution is very small. We get a strong peak at the excitation energy 9.195 MeV of ^{27}Si, which comes from the transition $^{27}\mathrm{Al}(\frac{5}{2}^{+}_{1}) \rightarrow {}^{27}\mathrm{Si}(\frac{7}{2}^{+}_{12})$. In the region of the excitation energy range 5-10 MeV, the $B(GT)$ strengths are more dense as compared with below 5 MeV. For ^{27}Si, the CCEI gives $\frac{3}{2}^{+}$ as the g.s. of ^{27}Si, while the experimental g.s. is $\frac{5}{2}^{+}$. The $B(GT)$ strength distribution from the IM-SRG interaction is shown in Fig. 6.11 (c). The IM-SRG interaction gives two strong peaks at energies 2.698 MeV and 7.387 MeV. The IM-SRG interaction gives $\frac{3}{2}^{+}$ g.s. for ^{27}Si. Figure 6.11 (d) shows the $B(GT)$ distribution from the USDB interaction. In this case we also get two strong peaks at 0.0 MeV and 2.841 MeV in ^{27}Si. The USDB interaction gives $\frac{5}{2}^{+}$ as the g.s. of ^{27}Si, in agreement with the experiment. The comparison of accumulated sums of $B(GT)$ strengths for theoretical and the experimental values is shown in Fig. 6.11 (e). The USDB and IM-SRG interactions give same trend as the experimental data, while the CCEI method gives smaller values.

6.3.11 ^{28}Si $\rightarrow$ ^{28}P

The experimental information on the distribution of $B(GT)$ strength is shown in Fig. 6.12. There are two experimental data sets available for the transition $^{28}\mathrm{Si} \rightarrow {}^{28}\mathrm{P}$. The charge exchange reaction $^{28}\mathrm{Si}(^{3}\mathrm{He},t)^{28}\mathrm{P}$ was performed at 150 MeV/nucleon, using the dispersion-matching technique [195] to get good energy resolution. In Fig. 6.12(a) the results for the $^{28}\mathrm{Si}(^{3}\mathrm{He},t)^{28}\mathrm{P}$ reaction are shown up to the excitation energy 5.57 MeV. The shell model study has already been carried out [195] by using Wildenthal's USD interaction. In this figure, a large $B(GT)$ strength is obtained at the excitation energy 2.15 MeV, but this value is normalized to the (p,n) data which is taken from Ref. [187]. The $B(GT)$ distribution from the $^{28}\mathrm{Si}(p,n)^{28}\mathrm{P}$ reaction performed at energy 136 MeV per nucleon is given in Fig. 6.12(b). Here, a large

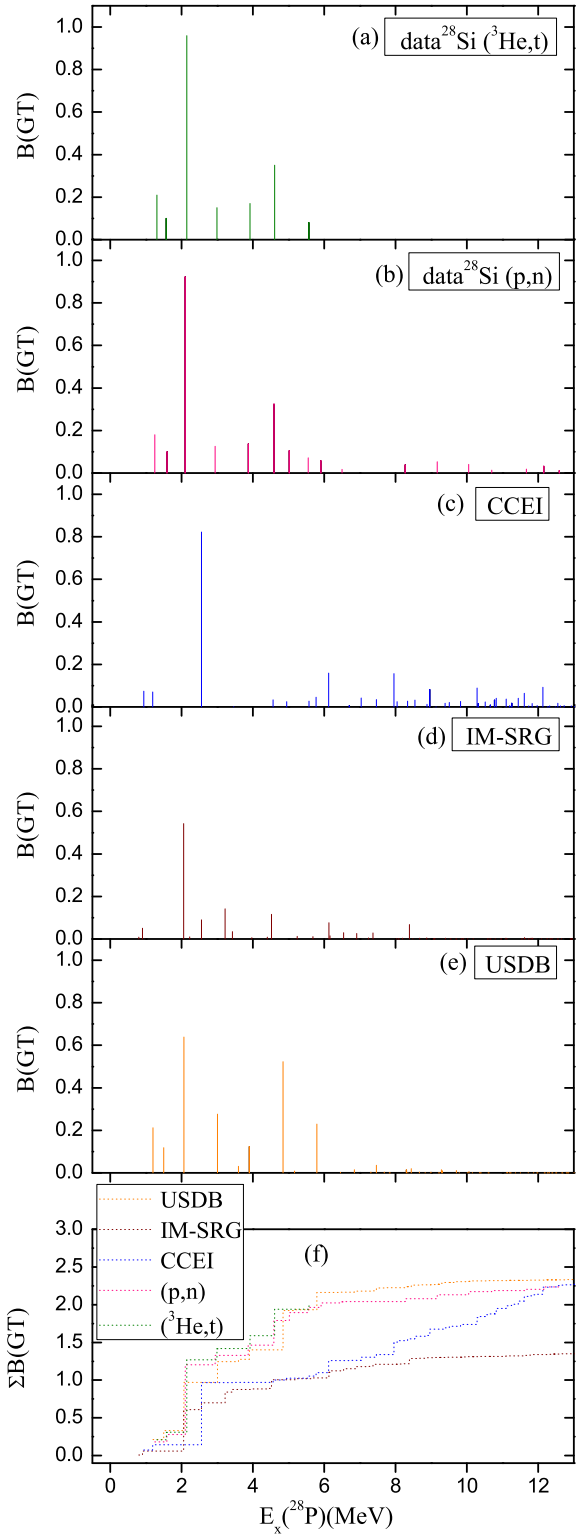

Figure 6.12: Comparison of the experimental and theoretical $B(GT)$ distributions for ^{28}Si $\rightarrow$ ^{28}P.

$B(GT)$ strength is obtained at the excitation energy 2.10 MeV of ^{28}P. Figure 6.12(c) shows the theoretical results by using CCEI. We get a strong transition at 2.562 MeV with $B(GT)$ strength 0.82, which comes from the transition $^{28}\mathrm{Si}(0^+) \rightarrow {}^{28}\mathrm{P}(1^+_3)$. We can also see many transitions above the excitation energy 4 MeV of ^{28}P, but they are very small in strength. The experimental g.s. of ^{28}P is 3^+, while the CCEI predicts 0^+. Figure 6.12(d) shows the $B(GT)$ strength distribution from the IM-SRG interaction. Here, we see a strong peak at the excitation energy 2.056 MeV of ^{28}P, which comes from the transition $^{28}\mathrm{Si}(0^+) \rightarrow {}^{28}\mathrm{P}(1^+_3)$. The IM-SRG interaction predicts 2^+ as the g.s. of ^{28}P. In Fig. 6.12(e), the $B(GT)$ strength distribution obtained with the USDB interaction is shown. In this case, we can see two comparable peaks at excitation energies 2.065 and 4.847 MeV of ^{28}P, which come from the transition $^{28}\mathrm{Si}(0^+) \rightarrow {}^{28}\mathrm{P}(1^+_3)$ and $^{28}\mathrm{Si}(0^+) \rightarrow {}^{28}\mathrm{P}(1^+_7)$, respectively. The USDB interaction gives 3^+ g.s. for ^{28}P, in agreement with the experiment. In Fig. 6.12(f), the accumulated sums of $B(GT)$ strengths is shown. The USDB interaction shows a similar trend as the experimental data. The IM-SRG interaction gives smaller value in comparison with the other interactions and the experimental data.

6.3.12 $^{31}\mathrm{P} \rightarrow {}^{31}\mathrm{Si}$

The $B(GT)$ strength distribution for the transition $^{31}\mathrm{P} \rightarrow {}^{31}\mathrm{Si}$ is shown in Fig. 6.13. In Fig. 6.13(a), the experimental data are shown for the reaction $^{31}\mathrm{P}(n,p)^{31}\mathrm{Si}$ [196]. In the experimental data, we see an intense peak at the excitation energy 5 MeV of ^{31}Si. The charge-exchange reaction $^{31}\mathrm{P}(n,p)^{31}\mathrm{Si}$ was performed to find the double differential cross section with the incident neutron energy of 198 MeV. By using multipole decomposition techniques the $B(GT)$ strength distribution was extracted. The shell model study using the universal *sd* (USD) interaction has already been done in Ref. [196]. Figure 6.13(b) shows the $B(GT)$ distribution obtained with the CCEI method. We see the strongest peak at the excitation energy 3.557 MeV of ^{31}Si, which comes from the transition $^{31}\mathrm{P}(\frac{1^+}{2\,1}) \rightarrow {}^{31}\mathrm{Si}(\frac{3^+}{2\,2})$. The strength of this

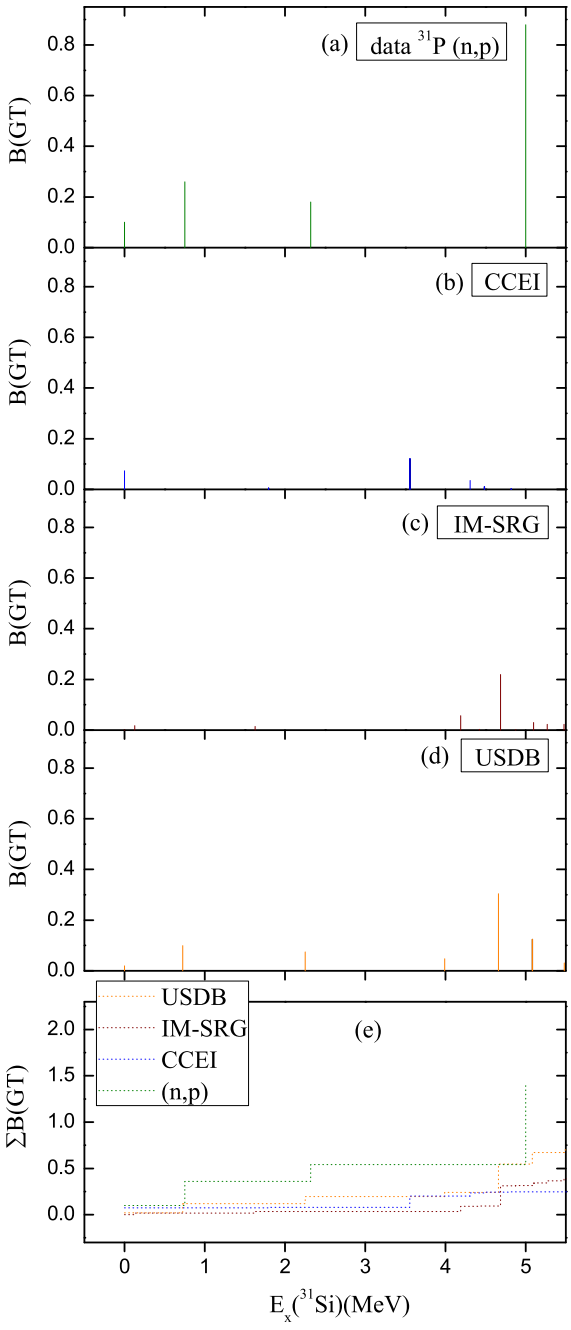

Figure 6.13: Comparison of the experimental and theoretical $B(GT)$ distributions for ^{31}P $\rightarrow$ ^{31}Si.

transition is very small in comparison to the strength of the strongest peak in the experiment. The CCEI gives the $\frac{3}{2}^+$ g.s. for ^{31}Si, which agrees with the experiment. In Fig. 6.13(c), the distribution of the $B(GT)$ strength is shown for the IM-SRG interaction. Here, we see the strongest peak at the excitation energy 4.685 MeV of ^{31}Si, which comes from the transition $^{31}\mathrm{P}(\frac{1}{2}^+_1) \rightarrow {}^{31}\mathrm{Si}(\frac{1}{2}^+_3)$, but also here the strength is very small compared with the strongest peak in the experimental data. The IM-SRG also reproduces correctly the experimental g.s. of ^{31}Si. Figure 6.13(d) shows the $B(GT)$ distribution from the USDB interaction. In this case the strongest peak is observed at the excitation energy 4.661 MeV with strength 0.30, which is larger than the strength of the peaks obtained in the *ab initio* interactions. This peak comes from the transition $^{31}\mathrm{P}(\frac{1}{2}^+_1) \rightarrow {}^{31}\mathrm{Si}(\frac{1}{2}^+_2)$. The USDB interaction also gives the correct g.s. of ^{31}Si. Fig. 6.13(e) shows the accumulated $B(GT)$ strengths for all three interactions and the experimental data. All three interactions give small values in comparison with the experimental data.

6.3.13 $^{32}\mathbf{S} \rightarrow {}^{32}\mathbf{P}$

Figure 6.14 presents the experimental and theoretical information on the distribution of the $B(GT)$ strength for the transition $^{32}\mathrm{S} \rightarrow {}^{32}\mathrm{P}$. For the experimental data, the charge exchange reaction $^{32}\mathrm{S}(d,{}^2\mathrm{He})^{32}\mathrm{P}$ was performed at forward angles and at an incident energy of E_d= 170 MeV with a resolution of 150 keV [197]. Figure 6.14 (a) shows the experimental data for $B(GT)$ strength distribution. Here, we see an intense peak at the excitation energy 4.2 MeV of ^{32}P. The experimental g.s. of ^{32}P is 1^+. Figure 6.14 (b) presents the results obtained by using the CCEI. Here, we see three strong peaks at excitation energies 4.573 MeV, 5.494 MeV and 6.741 MeV in ^{32}P, which come from the transitions $^{32}\mathrm{S}(0^+) \rightarrow {}^{32}\mathrm{P}(1^+_3)$, $^{32}\mathrm{S}(0^+) \rightarrow {}^{32}\mathrm{P}(1^+_4)$ and $^{32}\mathrm{S}(0^+) \rightarrow {}^{32}\mathrm{P}(1^+_5)$, respectively. The CCEI predicts the g.s. of ^{32}P as 2^+, while the experimental g.s. is 1^+. Figure 6.14 (c) shows the $B(GT)$ distribution obtained by using the IM-SRG interaction. Here, we notice a peak at excitation

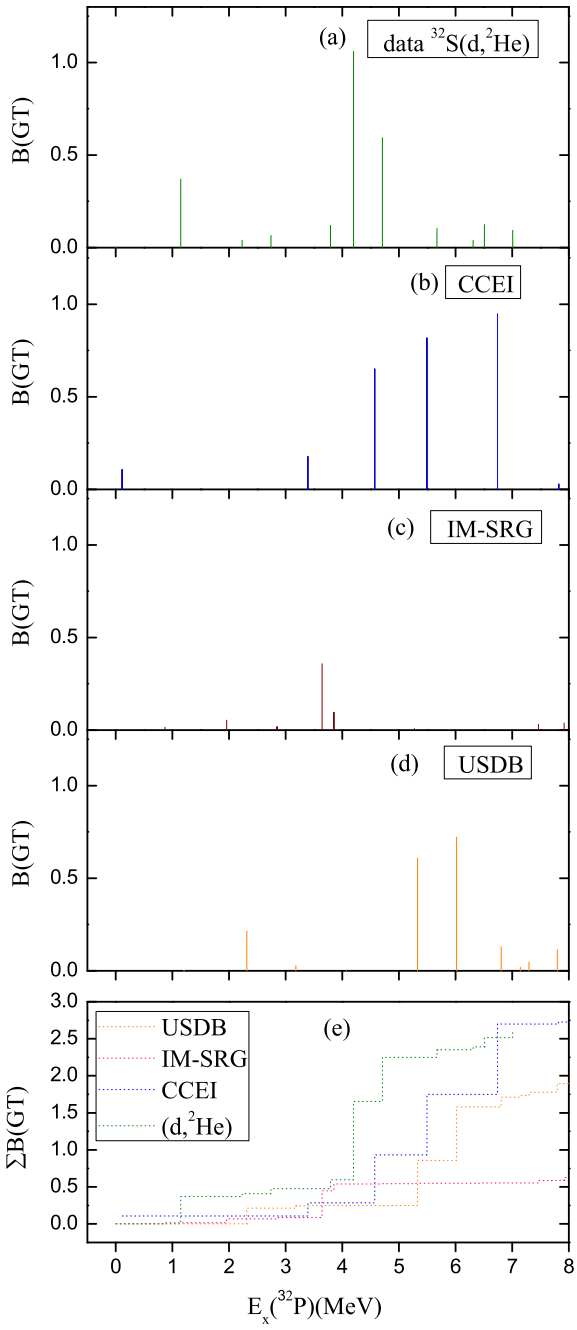

Figure 6.14: Comparison of the experimental and theoretical $B(GT)$ distributions for ^{32}S $\rightarrow$ ^{32}P.

energy 3.642 MeV of ^{32}P, which comes from the transition ^{32}S(0^+) $\rightarrow$ ^{32}P(1^+_5), which is weak in comparison with the strongest peak of the experimental data and the CCEI results. The IM-SRG interaction gives 0^+ as the g.s. of ^{32}P. Figure 6.14 (d) shows the $B(GT)$ distribution obtained by using the phenomenological USDB interaction. This interaction gives two peaks with comparable strengths, but weak compared with the strongest peak from the experimental data. The strong peaks with the USDB interaction are at excitation energies 5.33 MeV and 6.019 MeV of ^{32}P, which come from the transitions ^{32}S(0^+) $\rightarrow$ ^{32}P(1^+_6) and ^{32}S(0^+) $\rightarrow$ ^{32}P(1^+_7), respectively. The USDB interaction gives 3^+ as the g.s. of ^{32}P. Figure 6.14 (e) shows the accumulated sums of $B(GT)$ strength. Among the three interactions, the CCEI gives better results for the accumulated sums.

6.3.14 Centroid energies

In Secs. 6.3.1 - 6.3.13, we discuss GT distributions for *sd* shell nuclei obtained with the two *ab initio* interactions as well as the USDB. Among the three interactions, the USDB in general gives the best account of the experimental data. The *ab initio* interactions give a rather reasonable account of the experimental data, although there are deviations in many cases. In Table 6.2, we show a comparison between the experimental and theoretical centroid energies of the GT distributions for *sd* shell nuclei.

Ab initio interactions give larger GT strength than USDB and the experimental data in the lower excitation energy region, for example, in the ^{23}Na $\rightarrow$ ^{23}Ne and ^{24}Mg $\rightarrow$ ^{24}Na ($<$ 1 MeV) transitions. On the other hand, less GT strength is seen in lower excitation energy region; for example, in the ^{25}Mg $\rightarrow$ ^{25}Al and ^{26}Mg $\rightarrow$ ^{26}Na transitions. This is also true for the ^{26}Mg $\rightarrow$ ^{26}Al and ^{27}Al $\rightarrow$ ^{27}Si transitions in case of CCEI. These differences are reflected in the centroid energies of the GT distributions. They are smaller (larger) when more (less) strength is found in the lower-excitation-energy region as shown in Table 6.2. In case of the *ab initio*

interactions, the single-particle energy gap between $d_{3/2}$ and $d_{5/2}$ orbits is large compared with USDB, in particular for CCEI. This could explain the general feature that *ab initio* interactions show much lower strength at low energies in higher-mass nuclei. Especially small GT strengths for CCEI in the transitions shown in Figs. 6.9-6.11 can be attributed to insufficient contributions from $d_{3/2}$ orbit due to the largest gap among the interactions. As discussed in Sec. 6.2, deviations of the GT strength, calculated by using the *ab initio* interactions, from the experimental data become generally larger for the higher-mass nuclei because of the lack of three-body cluster terms among valence nucleons.

In the present calculations, we used the one-body GT operator with a universal quenching factor for both *ab initio* and phenomenological USDB interactions. However, the GT operator should be evolved in the same way as the Hamiltonians for the IM-SRG and CCEI methods. This gives rise to induced two-body operators [204]. Although this effect is taken into account here by adopting a phenomenological universal quenching factor for the one-body operator, induced two-body operators can lead to mass dependent quenching factors, which may also depend on the interactions. The present calculation, therefore, has limitations because of the truncations of the Hamiltonians up to the two-body terms, and the operator up to the one-body term.

Table 6.2: Comparison between the experimental and theoretical centroid energy of GT distributions for *sd* shell nuclei.

S.No.	Initial	Final	$\beta-$decay	(n,p)	$(d,^2\mathrm{He})$	$(t,^3\mathrm{He})$	$(^3\mathrm{He},t)$	(p,n)	CCEI	IM-SRG	USDB
1.	$^{20}\mathrm{Ne}(0^+)$	$^{20}\mathrm{F}(1^+)$		5.39					4.66	4.92	5.08
2.	$^{23}\mathrm{Na}(\frac{3}{2}^+)$	$^{23}\mathrm{Mg}(\frac{1}{2}^+,\frac{3}{2}^+,\frac{5}{2}^+)$					5.00		5.86	5.19	5.59
3.	$^{23}\mathrm{Na}(\frac{3}{2}^+)$	$^{23}\mathrm{Ne}(\frac{1}{2}^+,\frac{3}{2}^+,\frac{5}{2}^+)$		3.01					1.63	1.81	2.10
4.	$^{24}\mathrm{Mg}(0^+)$	$^{24}\mathrm{Na}(1^+)$			2.73	3.22			1.96	1.67	2.82
5.	$^{24}\mathrm{Mg}(0^+)$	$^{24}\mathrm{Al}(1^+)$					2.44	2.21	2.35	1.50	2.28
6.	$^{25}\mathrm{Mg}(\frac{5}{2}^+)$	$^{25}\mathrm{Al}(\frac{3}{2}^+,\frac{5}{2}^+,\frac{7}{2}^+)$					1.93		2.33	2.00	0.88
7.	$^{26}\mathrm{Mg}(0^+)$	$^{26}\mathrm{Na}(1^+)$			1.74	1.90			2.20	1.82	1.58
8.	$^{26}\mathrm{Mg}(0^+)$	$^{26}\mathrm{Al}(1^+)$					6.08	5.95	8.47	6.40	6.87
9.	$^{26}\mathrm{Si}(0^+)$	$^{26}\mathrm{Al}(1^+)$	1.44						1.24	1.37	1.32
10.	$^{27}\mathrm{Al}(\frac{5}{2}^+)$	$^{27}\mathrm{Si}(\frac{3}{2}^+,\frac{5}{2}^+,\frac{7}{2}^+)$					5.35		7.29	5.60	5.37
11.	$^{28}\mathrm{Si}(0^+)$	$^{28}\mathrm{P}(1^+)$					2.80	3.64	6.08	3.82	3.66
12.	$^{31}\mathrm{P}(\frac{1}{2}^+)$	$^{31}\mathrm{Si}(\frac{1}{2}^+,\frac{3}{2}^+)$		3.53					2.61	4.19	3.39
13.	$^{32}\mathrm{S}(0^+)$	$^{32}\mathrm{P}(1^+)$			4.10				5.36	3.45	5.31

6.4 Electron-capture rates in ^{23}Na and ^{25}Mg

In this section, we apply the GT transition strengths obtained by the *ab initio* effective interactions in *sd* shell nuclei to evaluate the electron capture rates in stellar environments.

Electron-capture rates at high densities and high temperatures are evaluated as [205–208]

$$\lambda = \frac{\ln 2}{6146(s)} \sum_i W_i \sum_f B(GT; i \to f)$$
$$\times \int_{\omega_{min}}^{\infty} \omega p (Q_{if} + \omega)^2 F(Z, \omega) S_e(\omega) d\omega,$$
$$Q_{if} = (M_{\rm p}c^2 - M_{\rm d}c^2 + E_i - E_f)/m_e c^2,$$
$$W_i = (2J_i + 1) e^{-E_i/kT} / \sum_i (2J_i + 1) e^{-E_i/kT}, \tag{6.2}$$

where ω and p are electron energy and momentum in units of $m_e c^2$ and $m_e c$; $M_{\rm p}$ and $M_{\rm d}$ are the masses of parent and daughter nuclei, and E_i and E_f are excitation energies of initial and final states. $F(Z, \omega)$ is the Fermi function, and $S_e(\omega)$ is the Fermi-Dirac distribution for electrons, where the chemical potential (μ_e) is determined from the density (ρY_e) by

$$\rho Y_e = \frac{1}{\pi^2 N_A} (\frac{m_e c}{\hbar})^3 \int_0^{\infty} (S_e - S_p) p^2 dp. \tag{6.3}$$

Here N_A is the Avogadro number, and S_p is the Fermi-Dirac distribution for positrons with the chemical potential $\mu_p = -\mu_e$. Its value can become as large as 2, 5 and 11 MeV at high densities $\rho Y_e = 10^8$, 10^9 and 10^{10} g/cm^3, respectively, decreasing slightly as the temperature increases. The reaction rates become larger at higher densities because of the larger chemical potential.

Here, we evaluate the electron-capture rates on ^{23}Na and ^{25}Mg. These rates are important in the study of the nuclear URCA processes that determine the cooling of the O-Ne-Mg core of stars with initial masses of 8-10 M$_\odot$ [209, 210]. The electron-

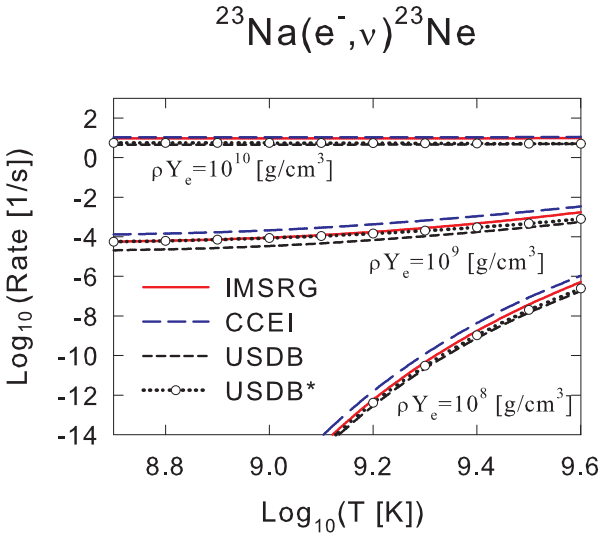

Figure 6.15: Calculated electron capture rates on ^{23}Na obtained by shell model calculations with different effective interactions.

capture rates for ^{23}Na(e$^-$,ν)^{23}Ne are evaluated by using the $B(GT)$ strengths obtained from the IM-SRG and CCEI methods for densities ρY_e =10^8, 10^9 and 10^{10} g/cm^3 and temperatures T = $10^{8.7}$-$10^{9.6}$ K. The GT transitions from $3/2^+$(g.s.) and $5/2^+$(0.440 MeV) states in ^{23}Na are included. The calculated rates are shown in Fig. 6.15. Here the same quenching factor f_q = 0.77 is used for all three interactions. The rates calculated by using the IM-SRG and CCEI methods are large compared with the USDB results. In the USDB* interaction shown in Fig. 6.15, the available experimental energies and $B(GT)$ strengths are taken into account, so the USDB* is more realistic [210]. Our results for the IM-SRG are close to those for the USDB*. This comes from the fact that the $B(GT)$ value for the transition from the g.s. of ^{23}Na to the g.s. of ^{23}Ne is close to the experimental value in case of IM-SRG, while it is smaller (larger) in case of USDB (CCEI). Both IM-SRG and CCEI give larger $B(GT)$ than USDB and the experiment for E_x = 0.5-3.5 MeV. Compared to USDB and USDB*, this leads to an enhancement of the capture rates by about a factor two

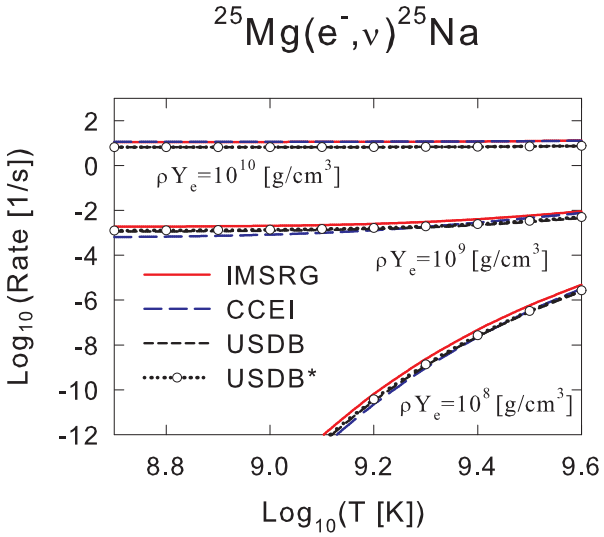

Figure 6.16: Calculated electron capture rates on ^{25}Mg obtained by shell model calculations with different effective interactions.

at higher densities; ρY_e =10^{10} g/cm^3. Since the dominant contribution to the capture rates for ^{23}Na (e^-, ν) ^{23}Ne comes from the g.s.-to-g.s. transition [209, 210], IM-SRG is practically applicable to the evaluation of the weak rates in stellar environment, in spite of the enhanced $B(GT)$ strength at E_x = 0.5-3.5 MeV. The results calculated from the CCEI are enhanced compared with the USDB* by a factor of 2-4.

Electron-capture rates for ^{25}Mg(e$^-$,ν)^{25}Na are shown in Fig. 6.16. The GT transitions from 5/2$^+$(g.s.), 1/2$^+$(0.588 MeV) and 3/2$^+$(0.975 MeV) states in ^{25}Mg are taken into account. The rates calculated with the CCEI and IM-SRG are close to those of the USDB* within a factor of two. We thus find that the GT strengths obtained by the *ab initio* interactions are reasonably valid for the evaluation of the weak rates at high densities and high temperatures for the lower-mass *sd* shell nuclei considered here.

6.5 Conclusions

In the present chapter we used *ab initio* effective interactions to calculate the GT strengths in the *sd* shell nuclei [58]. The results of the USDB interaction show reasonable agreement with the available experimental data in comparison with *ab initio* effective interactions. Our work adds more information on the GT strength distributions obtained in earlier work. In some cases shifting of energy levels occurs, because *ab initio* effective interactions are not able to reproduce correctly the excited states at the particular observed energies.

The GT calculated strengths are found to be applicable to evaluate nuclear weak rates for some lower-mass *sd* shell nuclei, such as ^{23}Na and ^{25}Mg, within a factor of 2-4 in stellar environments. These nuclear weak rates play important roles in astrophysical processes. It is highly desirable to improve the *ab initio* method by including further the three-body valence cluster terms, that is, the terms IM-SRG(3) or $H_3^{A_c+3}$.

Further, the GT strength results with *ab initio* interactions will be better by doing following: (i) if we use evolve GT operator instead of bare operator in our calculations (ii) adding the effect of two body currents (2BCs) in the quenching factor.

CHAPTER 7

^{35,37,39}S ISOTOPES IN $SD - PF$ SPACE : SHELL-MODEL INTERPRETATION

7.1 Introduction

The coexistence of normal and intruder (sometimes deformed) configurations in the low energy region [211] around the shell gaps $N = 20$ and $N = 28$, and the evidence of the erosion of these gaps [212], have been the focus of recent experimental investigations on Mg ($Z = 12$) [211], Si ($Z = 14$) [213], S ($Z = 16$) [214, 215] and Ar ($Z = 18$) isotopes [216]. A strongly deformed intruder g.s. has been reported for ^{31}Mg by the Leuven group [217]. The recent theoretical study of ^{30}Mg$(t, p)^{32}$Mg reaction revealed that 0^+ g.s. wavefunction is dominated by intruder (2p2h and 4p4h) configurations up to 95% level [218]. On the other hand, for ^{33}Mg the parity of the spin $I = 3/2$ ground-state remains a puzzle [219–222]. For this region, a reduction in the shell gap for the $s_{1/2}$ and $d_{3/2}$ proton orbitals has been reported for P, Cl and

K isotopes [223–226]. The particle-hole excitations involving intruder states play an important role in the study of nuclei lying between the *island of inversion* and the valley of stability. In Ar, the development of collectivity near the $N = 28$ shell gap has been reported in [227] where non-axially symmetric deformation was assigned to ^{48}Ar. In analogy to ^{32}Mg with $N = 20$, a new *island of inversion* around $N = 40$ has been predicted in Ref. [228]. Finally, the merging of the islands of inversion at $N = 20$ and $N = 28$, with large scale shell model calculations using an extension of the so called SDPF-U interaction was reported by Caurier *et al.* [229]. The focus in the present article is on S isotopes.

Sulfur isotopes exhibit many interesting properties: (i) ^{40}S [230] and ^{42}S [231] are deformed; (ii) ^{41}S exhibits γ-soft properties and collectivity [232]; (iii) shape coexistence in ^{43}S [233] and shape and configuration coexistence in ^{44}S is found [214, 234, 235]; (iv) experimental data indicate the erosion of $N = 28$ shell gap in the ^{42}Si and ^{44}S isotones [213, 236]. With all these, triple configuration coexistence has become a topic of current research [237]. Fig. 7.1 shows the systematics for $B(E2)$ values (top) and the energies of the 2_1^+ and 4_1^+ states (bottom), as a function of the neutron number, for even-even sulfur isotopes. A clear depletion in the $B(E2)$ values and a peak in the excitation energies are observed at ^{36}S with N = 20. As the neutron number increases, the corresponding $B(E2)$ value also increases, and the excitation energies assume nearly constant low values. These two observables are associated with the development of collectivity. Sulfur isotopes have also an astrophysical importance. In the nucleosynthesis of heavy Ca-Ti-Cr isotopes, neutron-rich sulfur isotopes play an important role [238].

From the theoretical side, besides the shell model analysis with realistic interactions presented in [60, 239, 240], Kaneko *et al.* [241] recently reported calculations for the positive parity states in even-even chain of sulfur isotopes using an extended pairing plus quadrupole-quadrupole interaction including monopole interactions (EPQQM).

In the present chapter, structure of the low energy states in ^{35,37,39}S isotopes, with

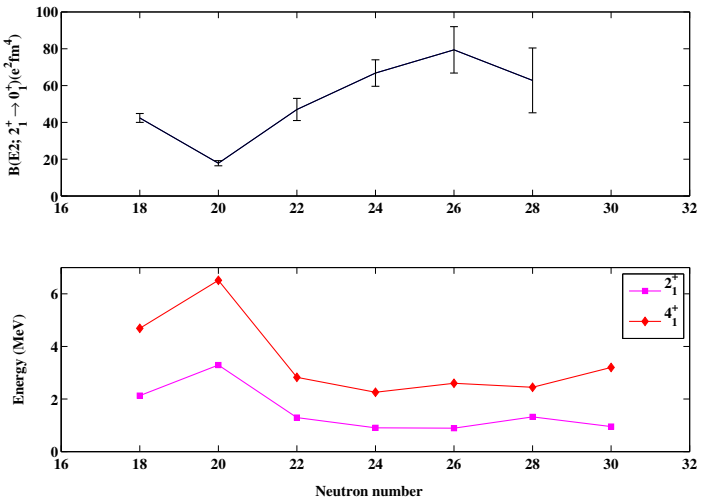

Figure 7.1: Experimental [94] $B(E2)$ values (top) and 2_1^+ and 4_1^+ energies (bottom) for even sulfur isotopes.

both positive and negative parities, are interpreted in the frame work of the shell model (SM) in $sd-pf$ space. For proper description of the states with opposite parities which involves cross shell excitations, it is necessary to remove the spurious center of mass excitations [242]. Present work will add more information to the earlier works [239, 240, 243], as we have performed calculations with the effective interaction SDPFMW that allows for the study of states of both parities. Thus, the present work gives a more comprehensive SM study for these isotopes.

7.2 Effective interactions

We present SM calculations in the $sd-pf$ space, with SDPF-U [60] and SDPFMW [61] interactions using NuShell [244] and NuShellX [111]. In the SDPFMW interaction, the sd part is the same as the original USD interaction [245]. These interactions are designed to be used in the valence space spanned by the orbitals $0d_{5/2}$, $1s_{1/2}$, $0d_{3/2}$, $0f_{7/2}$, $1p_{3/2}$, $0f_{5/2}$ and $1p_{1/2}$, for both protons and neutrons. In the case of SDPF-U, single-particle energies employed for the $0d_{5/2}$, $1s_{1/2}$, $0d_{3/2}$, $0f_{7/2}$, $1p_{3/2}$, $0f_{5/2}$ and

$1p_{1/2}$ orbitals are -3.699, -2.915, +1.895, +6.220, +6.314, +11.450, +6.479 MeV, respectively. For the SDPFMW interaction, the single-particle energies are -3.948, -3.164, +1.647, +14.008, +13.535, +18.524, +13.523 MeV, respectively. Protons and neutrons are restricted to the *sd*-shell for N<20, neutrons start filling the pf-shell for N>20. Natural parity states are described with only in-shell mixing, unnatural parity states with 1p-1h inter-shell neutron excitations.

In general, the 1p-1h state can include large spurious center-of-mass components. To remove this in the present SM calculations, we have followed the Gloeckner and Lawson approach [246], by diagonalizing the modified Hamiltonian.

$$H' = H_{\rm SM} + \beta_{\rm cm} H_{\rm cm} \tag{7.1}$$

$$= H_{\rm SM} + \beta_{\rm cm} \left\{ \frac{(\sum_{i=1}^{A} p_i)^2}{2Am} + \frac{1}{2}\frac{m\omega^2}{A}(\sum_{i=1}^{A} r_i)^2 - \frac{3}{2}\hbar\omega \right\}, \tag{7.2}$$

where $H_{\rm SM}$ is the shell model Hamiltonian, $H_{\rm cm}$ is the center of mass operator with r_i and p_i the coordinates and momenta of the individual nucleons. By taking large value of $\beta_{\rm cm}$, $H_{\rm cm}$ contribution to the low-lying states is suppressed (essentially removed). In the present work we have taken $\beta_{\rm cm} = 10$. We have also performed calculations for all the three sulfur isotopes with different set of $\beta_{\rm cm}$ values (5, 8, 10, 12, 15). Convergence of the energy levels is obtained at $\beta_{\rm cm}$=10.

To obtain natural parity states we have done calculations with SDPF-U and SDPFMW interactions but for the unnatural parity states with SDPFMW interaction only because SDPF-U interaction is not suitable for cross shell excitations. This interaction is $0\hbar\omega$ interaction and cannot be used in other circumstances with some $1\hbar\omega$ and $2\hbar\omega$ matrix elements are missing or zero in this interaction. For the positive-parity levels in ^{35}S we have performed 0p-0h calculations using SDPF-U and SDPFMW interactions, i.e. both protons and neutrons are only allowed to occupy the *sd* shell. Negative-parity levels can be obtained by exciting one neutron from the *sd* shell to the pf shell using SDPFMW interaction. The parity of the g.s. becomes

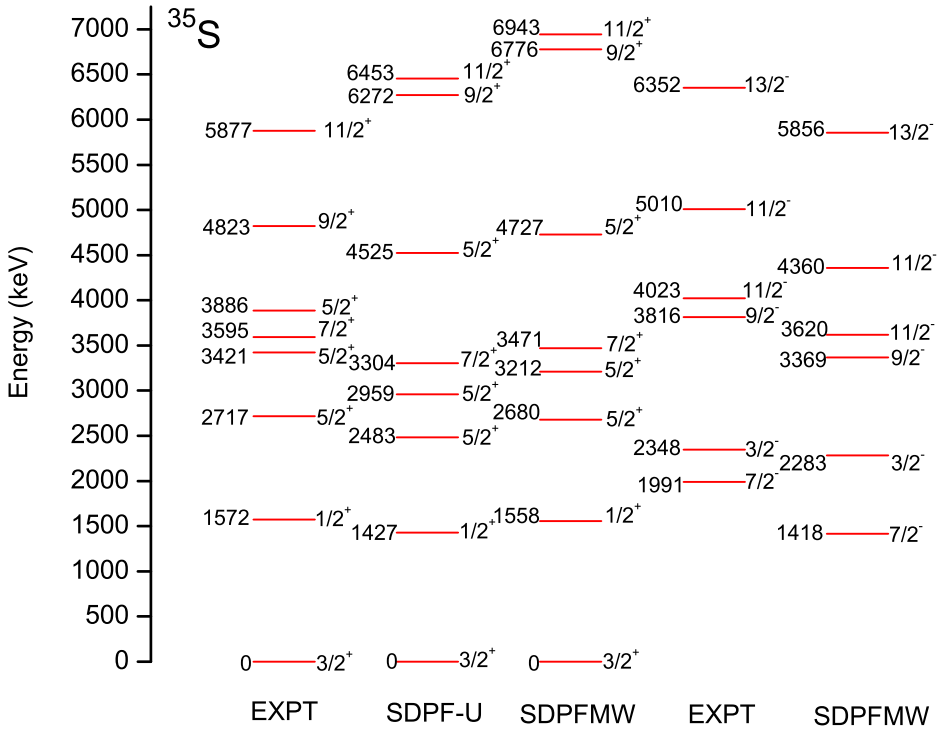

Figure 7.2: Calculated and experimental level schemes of ^{35}S. For the positive parity levels of ^{35}S the results with SDPFMW interaction are the same as with USD interaction. Here, we have allowed only neutron excitations to the pf shell.

negative from ^{37}S onwards, since one or more neutrons already occupy the pf shell. Thus negative-parity levels are obtained by 0p-0h calculations and 1p-1h calculations give the positive parity bands in case of ^{37,39}S.

7.3 Results and discussions

The comparison of the calculated positive- and negative-parity states with the experimental data for the odd ^{35,37,39}S isotopes is presented in Figs. 7.2-7.4. Experimental information for the energy levels in odd sulfur isotopes is available for ^{35}S, ^{37}S and

^{39}S isotopes in Refs. [239, 240, 243].

The angular momentum of the lowest energy states with both parities can be given a simple qualitative interpretation, associated with the last uncoupled neutron. In ^{35}S, $N = 19$, it occupies the $d_{3/2}$ orbital and corresponding g.s. is $J = 3/2^+$. For $N = 21$, the $f_{7/2}$ orbital is occupied by one neutron and therefore the g.s. is $J = 7/2^-$. For ^{39}S, though with the three neutrons in the $f_{7/2}$ shell, the lowest energy state does not necessarily have $J^\pi = 7/2^-$. The three neutron occupancies in $p_{3/2}$ orbital is important as discussed in [243]. As in many other chains of isotopes, the energy of the excited state with $J = 7/2^-$ is high in the lighter isotopes and decreases with increasing N until it becomes the g.s., while the $J = 3/2^+$ becomes the opposite parity excited state with the energy 1397-, and 864-keV for the ^{37}S and ^{39}S, respectively. In the case of ^{37}S, the SDPF-U interaction gives $J = 7/2^-$ as a g.s. and $J = 3/2^-$ as a first excited state. However, these levels are only at a difference of 4 keV in ^{39}S. One feature, where the relevance of using the full pf orbitals for the 1p-1h excitations can be seen, is in the energy of the excited opposite-parity states. The inclusion of the full pf shell decreases the energies of the opposite parity states, moving them towards the reported experimental values.

The calculated sequence of positive-parity levels has a clear correspondence with the experimentally observed ones in ^{35}S as is shown in Fig. 7.2. The results for $0\hbar w$ excitation given by SDPFMW interaction are close to the experimental values below $\sim$ 3.5 MeV. Negative parity states can be obtained using 1p-1h excitations. Previously shell model results for ^{35}S use a state-of-the-art PSDPF interaction [242] are reported in Ref. [239]. This interaction is for psdpf model space with ^{4}He core. In this, negative parity states are obtained by allowing one nucleon between major shells. The PSDPF interaction predicts the experimental $1/2^+_1$ – $5/2^+_1$ – $5/2^+_2$ – $7/2^+_1$ states at 1739, 2679, 3261 and 3544 keV [239], while corresponding values with SDPMW interaction are 1558, 2680, 3212 and 3471 keV, respectively. In the calculation with SDPFMW interaction the $1/2^+_1$ state is very close to the experimental value as compared to PSDPF interaction, while PSDPF interaction gives much better agreement

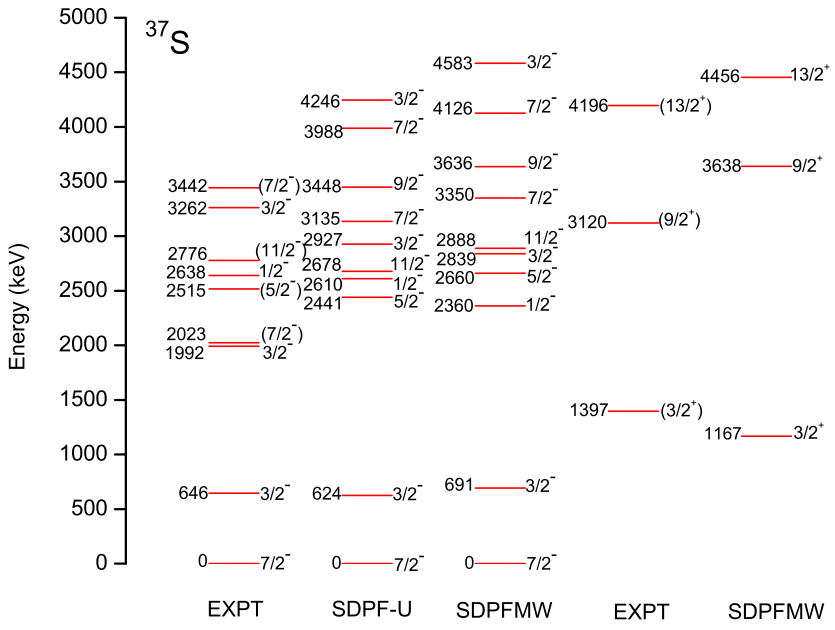

Figure 7.3: Calculated and experimental level scheme of ^{37}S.

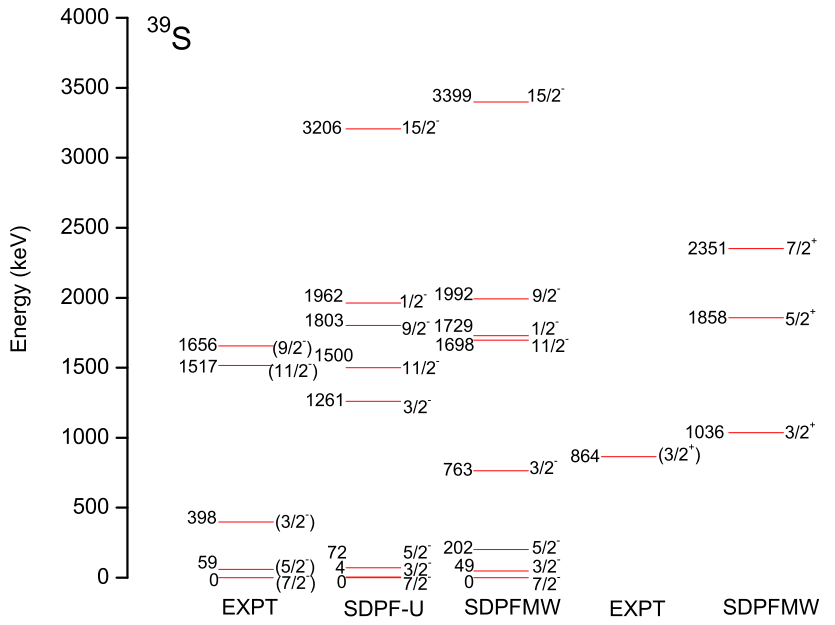

Figure 7.4: Calculated and experimental level scheme of ^{39}S.

with the measured negative parity states [239] than with SDPFMW interaction.

Experimental data are available up to $\sim$ 4.2 MeV for ^{37}S in Ref. [240]. Comparison of the calculated excited state energies with experimental data are shown in Fig. 7.3. The g.s. and first excited states have negative parities, and are correctly reproduced by the calculations. Experimentally $7/2^-_2$, $7/2^-_3$, $5/2^-_1$, $11/2^-_1$, states are not confirmed. Negative parity states are obtained by 0p-0h excitation using both interactions and positive parity states by 1p-1h excitations using SDPFMW interaction. The positive parity states are well reproduced with SDPFMW interaction. In Ref. [240], SM results are given only for the negative-parity levels and they are the same as those shown for SDPF-U results shown in Fig. 7.3. However there the positive-parity levels are not given as SDPF-U is not good for them and those in Fig. 7.3 are the first SM results. It is useful to add that for the positive parity states excitation from pf to $0g$ shell may contribute (also for ^{39}S discussed below) but the $0g$ orbit is not included in the present study.

For ^{39}S experimental and calculated results are shown in Fig. 7.4. The SDPF-U calculations predict very good results for these levels. The $3/2^-_1$ level is predicted in both calculations a few keV above the $7/2^-$ g.s. The SDPFMW calculations predict $3/2^+_1$ level at 1036 keV, while corresponding experimental values is 864 keV. The order of calculated levels with SDPF-U and SDPFMW interactions are $7/2^-$-$3/2^-$-$5/2^-$, while the experimental one is as $7/2^-$-$5/2^-$-$3/2^-$. In the case of ^{39}S, the shell model results show large configuration mixing, this reflects that the ^{39}S state is deviating from the single-particle nature.

In case of ^{35}S, with SDPFMW interaction, the dominant wave function for $7/2^-_1$, $3/2^-_1$ and $9/2^-_1$ is $\pi(d^6_{5/2}d^0_{3/2}s^2_{1/2})\otimes\nu(d^6_{5/2}d^2_{3/2}s^2_{1/2}f^1_{7/2})$, $\pi(d^6_{5/2}d^0_{3/2}s^2_{1/2})\otimes\nu(d^6_{5/2}d^2_{3/2}s^2_{1/2}p^1_{3/2})$ and $\pi(d^6_{5/2}d^0_{3/2}s^2_{1/2})\otimes\nu(d^6_{5/2}d^2_{3/2}s^2_{1/2}\ f^1_{7/2})$ with probabilities 36%, 32% and 20%, respectively. Wave functions of the natural parity states of ^{37}S and ^{39}S are discussed in Refs. [240, 243]. In the present work, we have focused on unnatural parity states. In the case of ^{37}S, unnatural parity states $3/2^+_1$, $9/2^+_1$ and $13/2^+_1$ are coming from the dominant configuration $\pi(d^6_{5/2}d^0_{3/2}s^2_{1/2})\otimes\ \nu(d^6_{5/2}d^3_{3/2}s^2_{1/2}f^2_{7/2})$ with probabilities 43%,

26% and 41%, respectively. In the case of ^{39}S, the dominant wave function for the unnatural parity state $3/2_1^+$ is $\pi(d^6_{5/2}d^0_{3/2}s^2_{1/2})\otimes\nu(d^6_{5/2}d^3_{3/2}s^2_{1/2}f^4_{7/2})$ with probability 17% and next major one is $\pi(d^6_{5/2}d^2_{3/2}s^0_{1/2})\otimes\nu(d^6_{5/2}d^3_{3/2}s^2_{1/2}f^4_{7/2})$ with probability 16%. As we move beyond ^{35}S, there are large number of configurations with very small probabilities. The configurations are strongly mixed.

For ^{37}S, the SDPFMW interaction predicts $11/2^-$ state at 2888 keV, this state correspond to $^{36}\mathrm{S}_{2_1^+}\otimes\nu f^1_{7/2}$ structure. The wave function of 2_1^+ at 3269 keV is dominated by the configuration $\pi(d^6_{5/2}s^1_{1/2}d^1_{3/2})\otimes\nu(d^6_{5/2}s^2_{1/2}d^4_{3/2})$. The dominant wave function of $^{37}\mathrm{S}_{11/2_1^-}$ is $\pi(d^6_{5/2}s^1_{1/2}d^1_{3/2})\otimes\nu(d^6_{5/2}s^2_{1/2}d^4_{3/2}f^1_{7/2})$ (87.6%). This supports the nature of particle-core coupled state similar to the SDPF-U result reported by Chapman *et al.,* in Ref. [240]. In the case of ^{39}S, the SDPFMW interaction predicts $11/2^-$ state at 1698 keV. The wave function of 2_1^+ at 1459 keV for ^{38}S is dominated by the configuration $\pi(d^6_{5/2}s^1_{1/2}d^1_{3/2})\otimes\nu(d^6_{5/2}s^2_{1/2}d^4_{3/2}f^2_{7/2})$. The dominant wave function of $^{39}\mathrm{S}_{11/2_1^-}$ is $\pi(d^6_{5/2}s^0_{1/2}d^2_{3/2})\otimes\nu(d^6_{5/2}s^2_{1/2}d^4_{3/2}f^3_{7/2})$ (24.75%). For the ^{39}S the $11/2^-$ state also favours the particle-core nature but this is not pure particle-core nature as compared to to ^{37}S because of small component of the wave function.

In the Fig. 7.5, the decomposition of proton and neutron wave functions decomposition is shown. For ^{37}S, the $11/2^-$ state corresponds to $I_p = 2^+\otimes I_n = 7/2^-$ configuration with probability of 97% of the total wave function. As we move to ^{39}S, the $11/2^-$ state shows many components: $I_p = 2^+\otimes I_n = 7/2^-$ (30%); $I_p = 2^+\otimes I_n = 9/2^-$ (2.5%); $I_p = 2^+\otimes I_n = 11/2^-$ (7%): $I_p = 2^+\otimes I_n = 15/2^-$ (3%), while the $I_p = 0^+\otimes I_n = 11/2^-$ corresponds to the largest component of the wave function (53%). Thus, $11/2^-$ state of ^{39}S shows more mixed type of configuration. This reflects weak particle-core type of structure.

For further understanding the structure of the levels, in Table 7.1, we present the $M1$, $E1$, $M2$ and $E3$ reduced transition probabilities with SDPFMW effective interaction. In this Table we have compared our calculated results with PSDPF interaction (Ref. [239]) also. The predictions of the SDPFMW interaction are in moderate agreement with $B(M1)$ and $B(E1)$ values. The $B(M2; 7/2_1^- \rightarrow 3/2_1^+)$ is

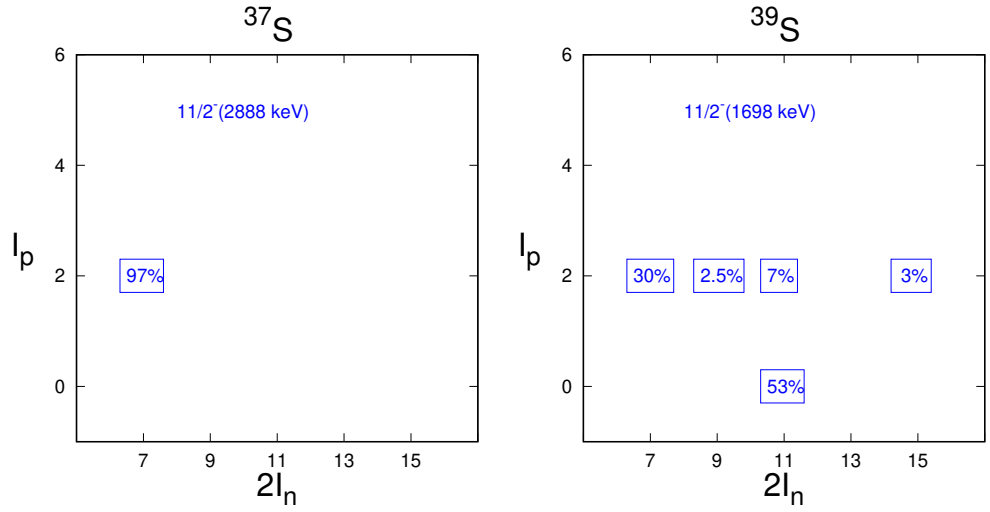

Figure 7.5: Decomposition of the total angular momentum of $11/2^-$ state of ^{37}S and ^{39}S into their $I_n \otimes I_p$ components.

3.4 $\mu_N^2 fm^2$ with $g_s^{\rm eff} = g_s^{\rm free}$. Using the new g factor values $g_{\nu s}^{\rm eff}$ = -2.869, $g_{\nu l}^{\rm eff}$ = -0.1, $g_{\pi s}^{\rm eff}$ = 4.189, $g_{\pi l}^{\rm eff}$ = 1.1 as suggested in Ref. [239], the $B(M2)$ value for this transition with SDPFMW interaction is 1.7 $\mu_N^2 fm^2$, corresponding to the experimental value 1.6 $\mu_N^2 fm^2$. The $B(E3 : 7/2_1^- \rightarrow 3/2_1^+)$ is 26.64 $e^2 fm^6$ with $e_{\rm eff}^{\pi}$=1.5e, $e_{\rm eff}^{\nu}$=0.5e. The recent PSDPF interaction gives a much better value of $B(E3 : 7/2^- \rightarrow 3/2^+)$ transition in ^{35}S than does a calculation based on the SDPFMW interaction. It is possible to get closer value by taking higher value of effective charges.

In Table 7.2, we have shown quadrupole and magnetic moments using e_p=1.5e, e_n=0.5e and $g_s^{\rm eff} = g_s^{\rm free}$ for ^{35,37,39}S. Our results are very close to the experimental values for $3/2_1^+$ in ^{35}S. In the case of magnetic moment for ^{35}S , the sign is not yet confirmed, our SM results predict the sign as positive. We have also predicted quadrupole and magnetic moments for few low-lying states for ^{37,39}S which are not experimentally known. It may be useful to plan for future experiments. Finally, for ^{37}S presented in Table 7.3 are the calculated and recently available experimental data [247] on spectroscopic factors (SFs) for single nucleon transfer. Results with SDPF-U interaction are reported in the Ref. [240]. We have recalculated spectroscopic factors with SDPFMW interaction. Both calculations give reasonable agreement with

Table 7.1: Comparison of calculated and experimental values of $B(M1)$, $B(E1)$, $B(M2)$ and $B(E3)$ transition rates for ^{35}S isotope with effective charges $e^{\pi}_{\rm eff}$=1.5e, $e^{\nu}_{\rm eff}$=0.5e and $g_s^{\rm eff} = g_s^{\rm free}$ in μ_N^2, e^2fm^2, $\mu_N^2 fm^2$ and e^2fm^6 units respectively. E_γ is given in keV.

Nucleus	$I_i^\pi \rightarrow I_f^\pi$	E_γ	Expt.	SDPFMW	PSDPF [239]
$B(M1)$					
^{35}S	$1/2_1^+ \rightarrow 3/2_1^+$	1572	0.004(1)	0.0407	0.020
	$5/2_1^+ \rightarrow 3/2_1^+$	2717	0.028(10)	0.0738	0.038
$B(E1)$					
^{35}S	$3/2_1^- \rightarrow 1/2_1^+$	775	$32(6)\times10^{-5}$	14.95×10^{-5}	54×10^{-5}
	$3/2_1^- \rightarrow 3/2_1^+$	2348	$31(6)\times10^{-6}$	24.63×10^{-5}	10×10^{-7}
$B(M2)$					
^{35}S	$7/2_1^- \rightarrow 3/2_1^+$	1991	1.6(5)	3.4	2.11
	$3/2_1^- \rightarrow 3/2_1^+$	2348	45(18)	0.0009	0.0044
$B(E3)$					
^{35}S	$7/2_1^- \rightarrow 3/2_1^+$	1991	115(86)	26.64	119

Table 7.2: Comparison of calculated and experimental value of quadrupole moments (with e_p=1.5e, e_n=0.5e) and magnetic moments ($g_s^{\rm eff} = g_s^{\rm free}$).

	$Q(eb)$			$\mu(\mu_N)$		
J^π	Expt.	SDPF-U	SDPFMW	Expt.	SDPF-U	SDPFMW
^{35}S						
$3/2_1^+$	+0.0471(9)	+0.055	+0.053	(+)1.00(4)	+1.084	+1.060
$5/2_1^+$	N/A	-0.0038	-0.0067	N/A	+1.787	+2.020
^{37}S						
$3/2_1^-$	N/A	-0.041	-0.039	N/A	-2.002	-1.900
$5/2_1^-$	N/A	-0.022	-0.013	N/A	-0.526	-0.613
$7/2_1^-$	N/A	-0.12	-0.11	N/A	-1.512	-1.586
^{39}S						
$3/2_1^-$	N/A	+0.110	+0.098	N/A	-0.820	-0.812
$5/2_1^-$	N/A	-0.058	-0.041	N/A	-0.680	-0.704
$7/2_1^-$	N/A	-0.094	-0.081	N/A	-1.127	-1.223

Table 7.3: Comparison of calculated and experimental value of spectroscopic factors for ^{37}S with SDPFMW (SF1) interaction. SF2 is SDPF-U calculation [240]

J^π	E(SM) (keV)	% [configuration]	SF(exp)	SF1	SF2
$7/2_1^-$	0	77% $[\nu f^1_{7/2}]$	0.77	0.91	0.86
$3/2_1^-$	691	75%$[\nu p^1_{3/2}]$	0.65	0.86	0.75
$1/2_1^-$	2360	87% $[\nu p^1_{1/2}]$	0.77	0.97	0.88
$5/2_1^-$	2660	79% $[\nu(d_{3/2}s_{1/2})^{-1} \otimes \nu(f^1_{7/2})]$	0.02	0.008	0.015
$3/2_2^-$	2839	60%$[\nu(d_{3/2}s_{1/2})^{-1} \otimes \nu(f^1_{7/2})]$	0.15	0.12	0.20
$7/2_2^-$	3350	41% $[\nu(d_{3/2}s_{1/2})^{-1} \otimes \nu(f^1_{7/2})]$	0.02	0.04	0.07

the experimental data.

7.4 Conclusions

In the present chapter, we have made a comprehensive shell model analysis of the latest experimental data on odd ^{35,37,39}S isotopes [59], using SDPF-U and SDPFMW effective interactions in the $sd-pf$ valence space.

Following broad conclusions are drawn:

1. The low energy levels are successfully reproduced, employing 0p-0h excitations for normal parity states and 1p-1h for opposite parity states.

2. Overall the SDPFMW interaction is seen to be much better for describing simultaneously properties of levels of both parities in ^{37,39}S isotopes.

3. We have also calculated the electric quadrupole and the magnetic dipole moments for ^{35,37,39}S and spectroscopic factors in ^{37}S. The shell model results are in good agreement with recently available experimental data.

CHAPTER 8

SUMMARY AND FUTURE OUTLOOK

8.1 Summary and conclusions

The focus of the present thesis is to perform *ab initio* no core shell model calculations (NCSM) for the lighter region of the nuclear chart. For this, we have performed calculations for O, F and N isotopes with NCSM. For heavier *sd* shell nuclei, we have calculated electromagnetic properties, *GT* strengths, electron capture rates using two *ab initio* effective interactions which are based on in-medium similarity renormalization group (IM-SRG) and coupled-cluster effective interaction (CCEI) approaches. In the last chapter we have reported shell model analysis of the latest experimental data for odd ^{35,37,39}S isotopes.

We have done the systematic study of low-lying energy spectrum (positive parity) for oxygen ($^{18-23}$O) and fluorine ($^{18-24}$F) chain using *ab initio* NCSM. We have used INOY, N3LO, and N2LOopt interactions and corresponding results are compared with the experimental data and phenomenological interaction USDB. The largest

model space we have reached for $^{18-21}$O and $^{18-19}$F is N_{max}=6 and for other oxygen and fluorine isotopes is N_{max}=4. We have also discussed the g.s. energy for O and F chain.

We have calculated the energy spectra for neutron rich $^{18-22}$N isotopes using NCSM. To calculate the energy spectrum we have used three different NN potentials: INOY, N3LO and CDB2K. The calculations have been done at $\hbar\Omega$=20 MeV, 14 MeV and 12 MeV using INOY, N3LO and CDB2K potentials, respectively. Apart from this, we have also performed shell model calculations with the YSOX interaction. The results with INOY interaction show good agreement with the experimental data in comparison to the other three interactions.

Using IM-SRG and CCEI approaches, we have reported the shell model results for quadrupole and magnetic moments for *sd* shell nuclei. We have also compared these results with the phenomenological USDB interaction. The results show reasonable agreement with the available experimental data. The results for $B(E2; 2_1^+ \rightarrow 0_1^+)$ transitions are also reported for Ne, Mg and Si isotopes. The $B(E2)$ results with IM-SRG and CCEI are in reasonable agreement with the experimental data except at N =20. This demonstrates the validity of *ab initio* description of deformation for doubly open-shell nuclei for *sd* shell. To see the importance of pf orbitals, we have also compared our results with SDPF-MU interaction by taking account of $2p-2h$ and $4p-4h$ configurations in *sd*-pf-shell model space.

We perform a systematic shell model study of Gamow-Teller transition strength distributions for thirteen sets of transitions in *sd* shell nuclei using IM-SRG and CCEI approaches. For comparison, we also show the results obtained by using the phenomenological USDB Hamiltonian. The phenomenological USDB results of the Gamow-Teller (GT_+/GT_-) strength distributions show reasonable agreements with the experimental data in comparison to the *ab initio* interactions. We also calculate the electron capture reaction rates for ^{23}Na(e$^-$, ν)^{23}Ne and ^{25}Mg(e$^-$, ν)^{25}Na.

We have made a comprehensive shell model analysis of the latest experimental data on odd ^{35,37,39}S isotopes, using SDPF-U and SDPFMW effective interactions in

the $sd-pf$ valence space. Overall the SDPFMW interaction is seen to be much better for describing simultaneously properties of levels of both parities in ^{37,39}S isotopes. We have also calculated the electric quadrupole and the magnetic dipole moments for ^{35,37,39}S and spectroscopic factors in ^{37}S. The shell model results are in good agreement with recently available experimental data.

8.2 Future directions

The present *ab initio* study can be extended to the followings:

- With the rapid progress in computational facilities, we can go for heavier nuclei with new and improved interactions from chiral effective field theory.
- The NCSM wave functions can be used to get more precisely other properties like proton charge radii and magnetic moments etc.
- The NCSM calculations can also be extended to calculate astrophysical spectroscopic factor strengths.
- *Ab initio* methods can be applied to double beta decay and neutrinoless double beta decay which are a current research topics in nuclear physics.
- In the present work the operator is not evolved when we are doing calculations with IM-SRG and CCEI for electromagnetic properties and GT-strengths. This work can be extended by evolving the operator for electromagnetic moments, GT-strengths and $B(E2)$ transitions using these *ab initio* effective interactions.
- In future using shell model it is possible to study normal and isospin-rich nuclei important for neutron stars [248].

BIBLIOGRAPHY

[1] P. Grangé, A. Lejeune, M. Martzolff, and J.-F.Mathiot, Consistent three-nucleon forces in the nuclear many-body problem, Phys. Rev. C **40**, 1040 (1989).

[2] S. Weinberg, Nuclear forces from chiral lagrangians, Phys. Lett. B **251**, 288 (1990).

[3] S. Weinberg, Effective chiral lagrangians for nucleon-pion interactions and nuclear forces, Nucl. Phys. B **363**, 3 (1991).

[4] V. Bernard, N. Kaiser, and U.-G. Meissner, Chiral dynamics in nucleons and nuclei, Int. J. Mod. Phys. E **4**, 193 (1995).

[5] A. M. Shirokov, A. I. Mazur, S. A. Zaytsev, J. P. Vary, and T. A. Weber, Nucleon-nucleon interaction in the J-matrix inverse scattering approach and few-nucleon systems, Phys. Rev. C **70**, 044005 (2004).

[6] D. R. Entem, and R. Machleidt, Accurate charge-dependent nucleon-nucleon potential at fourth order of chiral perturbation theory, Phys. Rev. C **68**, 041001(R) (2003).

[7] R. Machleidt, High-precision, charge-dependent Bonn nucleon-nucleon potential, Phys. Rev. C **63**, 024001 (2001).

[8] P. Doleschall, and I. Borbély, Properties of the nonlocal NN interactions required for the correct triton binding energy, Phys. Rev. C **62**, 054004 (2000).

[9] B. R. Barrett, P. Navrátil and J. P. Vary, Ab initio no core shell model, Prog. Part. Nucl. Phys. **69**, 131-181 (2013).

[10] S. C. Pieper, K. Varga, and R. B. Wiringa, Quantum Monte Carlo calculations of $A = 9, 10$ nuclei, Phys. Rev. C **66**, 044310 (2002).

[11] G. R. Jansen, M. D. Schuster, A. Signoracci, G. Hagen, and P. Navrátil, Open *sd*-shell nuclei from first principles, Phys. Rev. C **94**, 011301(R) (2016).

[12] G. R. Jansen, J. Engel, G. Hagen, P. Navrátil, and A. Signoracci, *Ab Initio* coupled-cluster effective interactions for the shell model: Application to neutron-rich oxygen and carbon isotopes, Phys. Rev. Lett. **113**, 142502 (2014).

[13] S. K. Bonger, R. J. Frunstahl and A. Schwenk, From low-momentum interactions to nuclear structure, Prog. Part. Nucl. Phys. **65**, 94 (2010).

[14] J. D. Holt, J. Menéndez, J. Simonis, and A. Schwenk, Three-nucleon forces and spectroscopy of neutron-rich calcium isotopes, Phys. Rev. C **90**, 024312 (2014).

[15] J. Simonis, K. Hebeler, J. D. Holt, J. Menendez, and A. Schwenk, Exploring *sd*-shell nuclei from two- and three-nucleon interactions with realistic saturation properties, Phys. Rev. C **93**, 011302(R) (2016).

[16] K. Tsukiyama, S. K. Bogner, and A. Schwenk, In-medium similarity renormalization group for open-shell nuclei, Phys. Rev. C **85**, 061304(R) (2012).

[17] S. R. Stroberg, A. Calci, H. Hergert, J. D. Holt, S. K. Bogner, R. Roth, and A. Schwenk, Nucleus-dependent valence-space approach to nuclear structure, Phys. Rev. Lett. **118**, 032502 (2017).

[18] H. Hergert, S. K. Bogner, T. D. Morris, A. Schwenk, and K. Tsukiyama, The In-Medium Similarity Renormalization Group: A novel *ab initio* method for nuclei, Phys. Rep. **621**, 165 (2016).

[19] P. C. Srivastava and V. Kumar, Spectroscopic factor strengths using *ab initio* approaches, Phys. Rev. C **94**, 064306 (2016).

[20] S. R. Stroberg, H. Hergert, J. D. Holt, S. K. Bonger, and A. Schwenk, Ground and excited states of doubly open-shell nuclei from ab initio valence-space Hamiltonians, Phys. Rev. C **93**, 051301(R) (2016).

[21] J. A. Sheikh, P. A. Ganai, R. P. Singh, R. K. Bhowmik, and S. Frauendorf, Shell model study of pairing correlations, Phys. Rev. C **77**, 014303 (2008).

[22] M. Hjorth-Jensen, Thomas T. S. Kuo and E. Osnes, Realistic effective interactions for nuclear systems, Phys. Rep. **261**, 125 (1995).

[23] C. Bloch, and J. Horowitz, Sur la détermination des premiers états dún systéme de fermions dans le cas dégéńéŕé, Nucl. Phys. **8**, 91 (1958).

[24] A. de. Shalit, and H. Feshbach, Theoretical Nuclear Physics Volume 1: Nuclear Structure, John Wiley, New York, 1974, p. 177.

[25] B. R. Barrett, R.G.L. Hewitt, and R. J. McCarthy, Simple and Exact Method for Calculating the Nuclear Reaction Matrix, Phys. Rev. C **3**, 1137 (1971).

[26] J. P. Vary, P. U. Sauer, and C. W. Wong, Convergence Rate of Intermediate-State Summations in the Effective Shell-Model Interaction, Phys. Rev. C **7**, 1776 (1973).

[27] B. R. Barrett, and M. W. Kirson, Higher-order terms and the apparent non-convergence of the perturbation expansion for the effective interaction in finite nuclei, Nucl. Phys. A **148**, 145 (1970).

[28] B. R. Barrett, and M. W. Kirson, The Microscopic Theory of Nuclear Effective Interactions and Operators, in: M. Baranger, E. Vogt (Eds.), Advances in Nuclear Physics, **6**, Plenum Press, New York, 1973, p. 219.

[29] T. H. Schucan, and H. A. Weidenmüller, The Effective Interaction in Nuclei and its Perturbation Expansion: An Algebraic Approach, Ann. Phys. (N.Y.) **73**, 108 (1972).

[30] T. H. Schucan, and H. A. Weidenmüller, Perturbation theory for the effective interaction in nuclei, Ann. Phys. (N.Y.) **76**, 483 (1973).

[31] G. E. Brown, T.T.S. Kuo, J. W. Holt, and S. Lee (Eds.), The Nucleon–Nucleon Interaction and the Nuclear Many-Body Problem, World Scientific Publishers, Singapore, (2010).

[32] P. Navrátil, and B. R. Barrett, Shell-model calculations for the three-nucleon system, Phys. Rev. C **57**, 562 (1998).

[33] P. Navrátil, and B. R. Barrett, Four-nucleon shell-model calculations in a Faddeev-like approach, Phys. Rev. C **59**, 1906 (1999).

[34] P. Navrátil, G. P. Kamuntavicius, and B. R. Barrett, Few-nucleon systems in a translationally invariant harmonic oscillator basis, Phys. Rev. C **61**, 044001 (2000).

[35] P. Navrátil, J. P. Vary, and B. R. Barrett, Properties of ^{12}C in the Ab Initio Nuclear Shell Model, Phys. Rev. Lett. **84**, 5728 (2000).

[36] P. Navrátil, J. P. Vary, and B. R. Barrett, Large-basis *ab initio* no-core shell model and its application to ^{12}C, Phys. Rev. C **62**, 054311 (2000).

[37] D.C.J. Marsden, P. Navrátil, S. A. Coon, and B. R. Barrett, Feasibility study of a three-nucleon force in the no-core shell model: ^{3}H binding energy, Phys. Rev. C **66**, 044007 (2002).

[38] I. Stetcu, B. R. Barrett, P. Navrátil, and J. P. Vary, Effective operators within the ab initio no-core shell model, Phys. Rev. C **71**, 044325 (2005).

[39] I. Stetcu, B. R. Barrett, P. Navrátil, and C. W. Johnson, Electromagnetic transitions with effective operators, Int. J. Mod. Phys. E **14**, 95 (2005).

[40] I. Stetcu, B. R. Barrett, P. Navrátil, and J. P. Vary, Effective operators in the NCSM formalism, Eur. Phys. J. A **25**, 489, s01 (2005).

[41] I. Stetcu, B. R. Barrett, P. Navrátil, and J. P. Vary, Long-and short-range correlations in the $ab-initio$ no-core shell model, Phys. Rev. C **73**, 037307 (2006).

[42] L. Jaqua, M. A. Hasan, J. P. Vary, and B. R. Barrett, Kinetic-energy operator in the effective shell-model interaction, Phys. Rev. C **46**, 2333 (1992).

[43] L. Jaqua, D. C. Zheng, B. R. Barrett, and J. P. Vary, Effects of the single-particle potential insertions in the effective interaction, Phys. Rev. C **48**, 1765 (1993).

[44] D.C. Zheng, B. R. Barrett, J.P. Vary, and H. Muther, Auxiliary potential in no-core shell-model calculations, Phys. Rev. C **51**, 2471 (1995).

[45] M. Thoresen, D. C. Zheng, and B. R. Barrett, Test of shell-model interactions for nuclear structure calculations, Phys. Rev. C **53**, 1997 (1996).

[46] M. Thoresen, P. Navrátil, and B. R. Barrett, Comparison of techniques for computing shell-model effective operators, Phys. Rev. C **57**, 3108 (1998).

[47] C. Forssén, B. D. Carlsson, H. T. Johansson, and D. Sööf, Large-scale exact diagonalizations reveal low-momentum scales of nuclei, Phys. Rev. C **97**, 034328 (2018).

[48] A. Saxena, and P. C. Srivastava, No core shell model study of $^{18-23}$O and $^{18-24}$F isotopes, arXiv:1812.08744 (Submitted for Publication).

[49] P. Doleschall, I. Borbély, Z. Papp, and W. Plessas, Nonlocality in the nucleon-nucleon interaction and three-nucleon bound states, Phys. Rev. C **67**, 064005 (2003).

[50] R. Machleidt, and D. R. Entem, Chiral effective field theory and nuclear forces, Phys. Rep. **503**, 1 (2011).

[51] A. Ekström, G. Baardsen, C. and Forssén, G. Hagen, M. Hjorth-Jensen, G. R. Jansen, R. Machleidt, W. Nazarewicz, T. Papenbrock, J. Sarich, and S. M. Wild, Optimized Chiral Nucleon-Nucleon Interaction at Next-to-Next-to-Leading Order, Phys. Rev. Lett. **110**, 192502 (2013).

[52] K. Suzuki and S. Y. Lee, Convergent theory for effective interaction in nuclei, Prog. Theor. Phys. **64**, 2091 (1980).

[53] K. Suzuki, Construction of Hermitian effective interaction in nuclei general relation between hermitian and non-hermitian forms, Prog. Theor. Phys. **68** (1), 246 (1982).

[54] S. Okubo, Diagonalization of Hamiltonian and Tamm-Dancoff Equation, Progr. Theor. Phys. **12**, 603 (1954).

[55] A. Saxena, and P. C. Srivastava, *Ab initio* no-core shell model study of neutron-rich nitrogen isotopes, Prog. Theor. Exp. Phys. **2019**, 073D02 (2019).

[56] C. Yuan, T. Suzuki, T. Otsuka, F. Xu, and N. Tsunoda, Shell-model study of boron, carbon, nitrogen, and oxygen isotopes with a monopole-based universal interaction, Phys. Rev. C **85**, 064324 (2012).

[57] A. Saxena, and P. C. Srivastava, First-principles results for electromagnetic properties of *sd* shell nuclei, Phys. Rev. C **96**, 024316(2017).

[58] A. Saxena, P. C. Srivastava, and T. Suzuki, *Ab initio* calculations of Gamow-Teller strengths in the *sd* shell, Phys. Rev. C **97**, 024310 (2018).

[59] A. Saxena, P. C. Srivastava, J. G. Hirsch, V.K.B. Kota and M. J. Ermamatov, ^{35,37,39}S isotopes in *sd*–*pf* space: Shell-model interpretation, Nucl. Phys. A **961**, 68 (2017).

[60] F. Nowacki and A. Poves, New effective interaction for $0\hbar\omega$ shell-model calculations in the $sd-pf$ valence space, Phys. Rev. C **79**, 014310 (2009).

[61] E. K. Warburton, J.A. Becker, and B.A. Brown, Mass systematics for $A = 29-44$ nuclei: The deformed A$\sim$32 region, Phys. Rev. C **41**, 1147 (1990).

[62] R. B. Wiringa, V.G.J. Stoks, and R. Schiavilla, Accurate nucleon-nucleon potential with charge-independence breaking, Phys. Rev. C **51**, 38 (1995).

[63] P. Doleschall, Influence of the short range nonlocal nucleon-nucleon interaction on the elastic $n-d$ scattering: Below 30 MeV, Phys. Rev. C **69**, 054001 (2004).

[64] K. Suzuki, and R. Okamoto, Degenerate Perturbation Theory in Quantum Mechanics, Progr. Theor. Phys. **70**, 439 (1983).

[65] K. Suzuki, and R. Okamoto, Effective Interaction Theory and Unitary-Model-Operator Approach to Nuclear Saturation Problem, Progr. Theor. Phys. **92**, 1045 (1994).

[66] S. K. Bogner, R. J. Furnstahl, and R. J. Perry, Similarity renormalization group for nucleon-nucleon interactions, Phys. Rev. C **75**, 061001(R) (2007).

[67] S. Bogner, T.T.S. Kuo, L. Coraggio, A. Covello, and N. Itaco, Low momentum nucleon-nucleon potential and shell model effective interactions, Phys. Rev. C **65**, 051301 (2002).

[68] S. K. Bogner, T. T. S. Kuo and, A. Schwenk, Model-independent low momentum nucleon interaction from phase shift equivalence, Phys. Rept. **386**, 1 (2003).

[69] R. Machleidt, K. Holinde, and Ch. Elster, The bonn meson-exchange model for the nucleon—nucleon interaction, Phys. Rep. **149**, 1 (1987).

[70] B. F. Gibson, H. Kohlhoff, and H. V. von Geramb, Inversion potential analysis of the nuclear dynamics in the triton, Phys. Rev. C **51**, R465(R) (1995).

[71] P. Navrátil, (private communication)

[72] D. H. Gloekner, and D. R. Lawson, Spurious center-of-mass motion, Phys. Lett. B **53**, 313 (1974).

[73] I. Talmi, Simple Models of Complex Nuclei, Harwood Academic Publishers, Switzerland (1993).

[74] C. Lanczos, J. Res. Nat. Bur. Standards, Sect. B **45**, 255 (1950).

[75] E. Caurier and F. Nowacki, Present status of shell model techniques, Acta Phys. Pol. B **30** (3), 705 (1999).

[76] E. Caurier, G. Martínez-Pinedo, F. Nowacki, A. Poves, J. Retamosa, and A. P. Zuker, Full $0\hbar\omega$ shell model calculation of the binding energies of the $1f_{7/2}$ nuclei, Phys. Rev. C **59**, 2033 (1999).

[77] P. Navrátil, and E. Caurier, Nuclear structure with accurate chiral perturbation theory nucleon-nucleon potential: Application to ^{6}Li and ^{10}B, Phys. Rev. C **69**, 014311 (2004).

[78] C. W. Johnson, W. E. Ormand, K. S. McElvain, and H. Shan, BIGSTICK: A flexible configuration-interaction shell-model code, arXiv:1801.08432.

[79] K. A. Wendt, C. Forssén, T. Papenbrock, and D. Sääf, Infrared length scale and extrapolations for the no-core shell model, Phys. Rev. C **91**, (2015) 061301.

[80] I. J. Shin, Y. Kim, P. Maris, J. P. Vary, C. Forssén, J. Rotureau, and N. Michel, *Ab initio* no-core solutions for ^{6}Li, J. Phys. G **44**, (2017) 075103.

[81] J. P. Vary, The Many-Fermion Dynamics Code, Iowa. State University (1992); J. P. Vary and D. C. Zheng, ibid. (1994) (unpublished).

[82] P. Navrátil, S. Quaglioni, I. Stetcu, and B. R. Barrett, Recent developments in no-core shell-model calculations, J. Phys. G **36**, 083101 (2009).

[83] S. Baroni, P. Navrátil, and S. Quaglioni, Ab Initio Description of the Exotic Unbound ^{7}He Nucleus, Phys. Rev. Lett. **110**, 022505 (2013).

[84] S. Baroni, P. Navrátil, and S. Quaglioni, Unified ab initio approach to bound and unbound states: No-core shell model with continuum and its application to ^{7}He, Phys. Rev. C **87**, 034326 (2013).

[85] P. Navrátil, S. Quaglioni, G. Hupin, C. Romero-Redondo, and A. Calci, Unified *ab initio* approaches to nuclear structure and reactions, Phys. Scr. **91**, 053002 (2016).

[86] A. Calci, P. Navrátil, R. Roth, J. Dohet-Eraly, S. Quaglioni, and G. Hupin, Can *Ab Initio* Theory Explain the Phenomenon of Parity Inversion in ^{11}Be ?, Phys. Rev. Lett. **117**, 242501 (2016).

[87] C. Forssén, P. Navrátil, W. E. Ormand, and E. Caurier, Large basis ab initio shell model investigation of ^{9}Be and ^{11}Be, Phys. Rev. C **71**, 044312(2005).

[88] E. Dikmen, A. F. Lisetskiy, B. R. Barrett, P. Maris, A. M. Shirokov, and J. P. Vary, *Ab initio* effective interactions for *sd*-shell valence nucleons, Phys. Rev. C **91**, 064301 (2015).

[89] A. Tichai, E. Gebrerufael, K. Vobig, and R. Roth, Open-Shell Nuclei from No-Core Shell Model with Perturbative Improvement, Phys. Lett. B, **786**, 448 (2018).

[90] T. Otsuka, T. Suzuki, J. D. Holt, A. Schwenk, and Y. Akaishi, Three-Body Forces and the Limit of Oxygen Isotopes, Phys. Rev. Lett. **105**, 032501 (2010).

[91] B. A. Brown and W. A. Richter, New USD Hamiltonians for the *sd* shell, Phys. Rev. C **74**, 034315 (2006).

[92] E. Caurier, P. Navrátil, W. E. Ormand, and J. P. Vary, Intruder states in ^{8}Be, Phys. Rev. C **64**, 051301(R) (2001).

[93] W. Polyzou, and W. Gloc̈kle, Three-body interactions and on-shell equivalent two-body interactions, Few-Body Syst. **9**, 97 (1990).

[94] NNDC, https://www.nndc.bnl.gov/.

[95] G. Hagen, M. Hjorth-Jensen, G. R. Jansen, R. Machleidt, and T. Papenbrock, Continuum Effects and Three-Nucleon Forces in Neutron-Rich Oxygen Isotopes, Phys. Rev. Lett. **108**, 242501(2012).

[96] A. Cipollone, and C. Barbieri, and P. Navrátil, Isotopic Chains Around Oxygen from Evolved Chiral Two- and Three-Nucleon Interactions, Phys. Rev. Lett. **111**, 062501(2013).

[97] H. Hergert, S. Binder, A. Calci, J. Langhammer, and R. Roth, *Ab Initio* Calculations of Even Oxygen Isotopes with Chiral Two-Plus-Three-Nucleon Interactions, Phys. Rev. Lett. **110**, 242501 (2013).

[98] C Forssén, R Roth and P Navrátil, Systematics of 2^+ states in C isotopes from the no-core shell model, J. Phys. G: Nucl. Part. Phys. **40**, 055105 (2013).

[99] D. Sohler, M. Stanoiu, Zs. Dombrádi, F. Azaiez, B. A. Brown, M. G. Saint-Laurent, O. Sorlin, Yu.-E. Penionzhkevich, N. L. Achouri, and J. C. Angélique *et.al.*, In-beam γ-ray spectroscopy of the neutron-rich nitrogen isotopes $^{19-22}$N, Phys. Rev. C **77**, 044303 (2008).

[100] C. S. Sumithrarachchi, D. J. Morrissey, A. D. Davies, D. A. Davies, M. Facina, E. Kwan, P. F. Mantica, M. Portillo, Y. Shimbara, J. Stoker *et.al.*, States in ^{22}O via β decay of ^{22}N, Phys. Rev. C **81**, 014302 (2010).

[101] C. Rodríguez-Tajes, D. Cortina-Gil, H. Álvarez-Pol, T. Aumann, E. Benjamim, J. Benlliure, M. J. G. Borge, M. Caamaño, E. Casarejos, A. Chatillon *et.al.*, Structure of ^{22}N and the $N = 14$ subshell, Phys. Rev. C **83**, 064313 (2011).

[102] S. Bagchi, R. Kanungo, W. Horiuchi, G. Hagen, T.D. Morris, S.R. Stroberg, T. Suzuki, F. Ameil, J. Atkinson,Y. Ayyad *et.al.*, Neutron skin and signature of the N = 14 shell gap found from measured proton radii of $^{17-22}$N, Phys. Lett. B **790**, 251 (2019).

[103] H. Nakada, and T. Otsuka, E2 properties of nuclei far from stability and the proton-halo problem of ^{8}B, Phys. Rev. C **49**, 886 (1994).

[104] C. R. Hoffman, M. Albers, M. Alcorta, S. Almaraz-Calderon, B. B. Back, S. I. Baker, S. Bedoor, P. F. Bertone, B. P. Kay, J. C. Lighthall, T. Palchan, *et.al.*, Single-neutron excitations in ^{18}N, Phys. Rev. C **88**, 044317 (2013).

[105] N. Shimizu, Nuclear shell-model code for massive parallel computation, "KSHELL", (private communication).

[106] Ruprecht Machleidt (private communication).

[107] T. Otsuka, T. Suzuki, J.D. Holt, A. Schwenk, and Y. Akaisji, Three-Body Forces and the Limit of Oxygen Isotopes, Phys. Rev. Lett. **105**, 032501 (2010).

[108] J. D. Holt, T. Otsuka, A. Schwenk, and T. Suzuki, Three-body forces and shell structure in calcium isotopes, J. Phys. G **39**, 085111 (2012).

[109] L. Cáceres, A. Lepailleur, O. Sorlin, M. Stanoiu, D. Sohler, Z. Dombradi, S. K. Bogner, B. A. Brown, H. Hergert, J. D. Holt et al., Nuclear structure studies of ^{24}F, Phys. Rev. C **92**, 014327 (2015).

[110] Z. Vajta, M. Stanoiu, D. Sohler, G. R. Jansen, F. Azaiez, Z. Dombradi, O. Sorlin, B. A. Brown, M. Belleguic, C. Borcea et al., Excited states in the neutron-rich nucleus ^{25}F, Phys. Rev. C **89**, 054323 (2014).

[111] B. A. Brown, and W. D. M. Rae, The Shell-Model Code NuShellX@MSU, Nuclear Data Sheets **120**, 115 (2014).

[112] K. Tsukiyama, S. K. Bogner, and A. Schwenk, In-medium similarity renormalization group for nuclei, Phys. Rev. Lett. **106**, 222502 (2011).

[113] P. Navrátil, Local three-nucleon interaction from chiral effective field theory, Few-Body Syst. **41**, 117 (2007).

[114] S. Okubo, Diagonalization of Hamiltonian and Tamm-Dancoff Equation, Prog. Theor. Phys. **12**, 603 (1954).

[115] P. Navrátil and B. R. Barret, No-core shell-model calculations with starting-energy-independent multivalued effective interactions, Phys. Rev. C **54**, 2986 (1996).

[116] W. A. Richter, S. Mkhize, and B. Alex Brown, *sd*-shell observables for the USDA and USDB Hamiltonians, Phys. Rev. C **78**, 064302 (2008).

[117] N. J. Stone, Atomic Data and Nuclear Data Tables **90**, 75 (2005).

[118] IAEA https://www-nds.iaea.org/nuclearmoments/.

[119] M. De Rydt, M. Depuydt, and G. Neyens, Atomic Data and Nuclear Data Tables **99**, 391 (2013).

[120] H. Iwasaki, T. Motobayashi, H. Sakurai, K. Yoneda, T. Gomi, N. Aoi, N. Fukuda, Zs. Fülöp, U. Futakami, Z. Gacsi et al., Quadrupole collectivity of ^{28}Ne and the boundary of the island of inversion, Phys. Lett. B **620**, 118 (2005).

[121] B. V. Pritychenko, T. Glasmacher, P. D. Cottle, M. Fauerbach, R. W. Ibbotson, K. W. Kemper, V. Maddalena, A. Navin, R. Ronningen, A. Sakharuk et al., Role of intruder configurations in ^{26,28}Ne and ^{30,32}Mg, Phys. Lett. B **461**, 322 (1999).

[122] G. Neyens, M. Kowalska, D. Yordanov, K. Blaum, P. Himpe, P. Lievens, S. Mallion, R. Neugart, N. Vermeulen, Y. Utsuno, and T. Otsuka, et al., Measurement of the Spin and Magnetic Moment of ^{31}Mg: Evidence for a Strongly Deformed Intruder Ground State, Phys. Rev. Lett. **94**, 022501 (2005).

[123] M. De Rydt, G. Neyens, K. Asahi, D. L. Balabanski, J. M. Daugas, M. Depuydt, L. Gaudefroy, S. Grévy, Y. Hasama, Y. Ichikawa et al., Precision measurement of the electric quadrupole moment of ^{31}Al and determination of the effective proton charge in the sd-shell, Phys. Lett. B **678**, 344 (2009).

[124] P. Himpe, G. Neyens, D. L. Balabanski, G. Bélier, D. Borremans, J. M. Daugas, F. de Oliveira Santos, M. De Rydt, K. Flanagan, G. Georgiev et al., g factors of ^{31,32,33}Al: Indication for intruder configurations in the ^{33}Al ground state, Phys. Lett. B **643**, 257 (2006).

[125] M. Keim, U. Georg, A. Klein, R. Neugart, M. Neuroth, S. Wilbert, P. Lievens, L. Vermeeren, B. A. Brown, and ISOLDE Collaboration, Measurement of the electric quadrupole moments of $^{26–29}$Na, Eur. Phys. J. A **8**, 31 (2000).

[126] P. Doornenbal, H. Scheit, S. Takeuchi, N. Aoi, K. Li, M. Matsushita, D. Steppenbeck, H. Wang, H. Baba, E. Ideguchi et al., Mapping the deformation in the "island of inversion": Inelastic scattering of ^{30}Ne and ^{36}Mg at intermediate energies, Phys. Rev. C **93**, 044306 (2016).

[127] A. M. Hurst, C. Y. Wu, J. A. Becker, M. A. Stoyer, C. J. Pearson, G. Hackman, M. A. Schumaker, C. E. Svensson, R.A.E. Austin, G. C. Ball et al., Narrowing of the neutron *sd-pf* shell gap in ^{29}Na, Phys. Lett. B **674**, 168 (2009).

[128] M. Seidlitz, P. Reiter, R. Altenkirch, B. Bastin, C. Bauer, A. Blazhev, N. Bree, B. Bruyneel, P. A. Butler, J. Cederkall et al., Coulomb excitation of ^{29,30}Na: Mapping the borders of the island of inversion, Phys. Rev. C **89**, 024309 (2014).

[129] O. Niedermaier, H. Scheit, V. Bildstein, H. Boie, J. Fitting, R.von Hahn, F. Kock, M. Lauer, U.K. Pal, H. Podlech et al., "Safe" Coulomb Excitation of ^{30}Mg, Phys. Rev. Lett. **94**, 172501 (2005).

[130] M. Seidlitz, D. Mücher, P. Reiter, V. Bildstein, A. Blazhev, N. Bree, B. Bruyneel, J. Cederkäll, E. Clement, T. Davinson et al., Coulomb excitation of ^{31}Mg, Phys. Lett. B **700**, 181 (2011).

[131] J. A. Church, C. M. Campbell, D.-C. Dinca, J. Enders, A. Gade, T. Glasmacher, Z. Hu, R. V. F. Janssens, W. F. Mueller, H. Olliver et al., Measurement of E2 transition strengths in ^{32,34}Mg, Phys. Rev. C **72**, 054320 (2005).

[132] D. Borremans, S. Teughels, N. A. Smirnova, D. L. Balabanski, N. Coulier, J.-M Daugas, F. de Oliveira Santos, G. Georgiev, M. Lewitowicz, I. Matea et al., Spin and magnetic moment of ^{31}Al ground state, Phys. Lett. B **537**, 45 (2002).

[133] D. Kameda, H. Ueno, K. Asahi, M. Takemura, A. Yoshimi, T. Haseyama, M. Uchida, K. Shimada, D. Nagae, G. Kijima et al., Measurement of the electric quadrupole moment of ^{32}Al, Phys. Lett. B **647**, 93 (2007).

[134] H. Heylen, M. De Rydt, G. Neyens, M. L. Bissell, L. Caceres, R. Chevrier, J. M. Daugas, Y. Ichikawa, Y. Ishibashi, O. Kamalou et al., High-precision quadrupole moment reveals significant intruder component in $^{33}_{13}\mathrm{Al}_{20}$ ground state, Phys. Rev. C **94**, 034312 (2016).

[135] E. Caurier, F. Nowacki, and A. Poves, Merging of the islands of inversion at $N = 20$ and $N = 28$, Phys. Rev. C **90**, 014302 (2014).

[136] Y. Utsuno, T. Otsuka, T. Glasmacher, T. Mizusaki, and M. Honma, Onset of intruder ground state in exotic Na isotopes and evolution of the $N = 20$ shell gap, Phys. Rev. C **70**, 044307 (2004).

[137] W. Geithner, B. A. Brown, K. M. Hilligsøe, S. Kappertz, M. Keim, G. Kotrotsios, P. Lievens, K. Marinova, R. Neugart, H. Simon, and S. Wilbert, Nuclear moments of neon isotopes in the range from ^{17}Ne at the proton drip line to neutron-rich ^{25}Ne, Phys. Rev. C **71**, 064319 (2005).

[138] Data extracted using the NNDC World Wide Web site from the ENSDF database.

[139] D. Sundholm, and J. Olsen, Finite element multiconfiguration Hartree-Fock calculations on carbon, oxygen, and neon: the nuclear quadrupole moments of carbon-11, oxygen-17, and neon-21, J. Phys. Chem. **96**, 627 (1992).

[140] N. J. Stone, Atomic Data and Nuclear Data Tables **111-112**, 1 (2016).

[141] A. Halkier, O. Christiansen, D. Sundholm, and P. Pyykkö, An improved value of the nuclear quadrupole moment of the 197 keV $I = 52$ excited state of ^{19}F, Chem. Phys. Lett. **271**, 273 (1997).

[142] P. Pyykkö, and A. J. Sadlej, Determination of the ^{23}Na nuclear quadrupole moment from molecular data for NaF and NaCl, Phys. Lett. **227**, 221 (1994).

[143] G. Neyens, P. Himpe, D. L. Balabanski, P. Morel, L. Perrot, M. De Rydt, I. Stefan, C. Stodel, J. C. Thomas, N. Vermeulen et al., The "island of inversion" from a nuclear moments perspective and the g factor of ^{35}Si, Eur. Phys. J. Special Topics **150**, 149 (2007).

[144] D. Sundholm and J. Olsen, Finite element MCHF calculations on Mg(3s3p; ^{3}P^0): The nuclear quadrupole moment of ^{25}Mg, Nucl. Phys. A **534**, 360 (1991).

[145] V. Kellö, A. J. Sadlej, P. Pyykkö, D. Sundholm, and M. Tokman, Electric quadrupole moment of the ^{27}Al nucleus: Converging results from the AlF and AlCl molecules and the Al atom, Chem. Phys. Lett. **304**, 414 (1999).

[146] K. Matsuta, T. Minamisono, M. Fukuda, M. Mihara, K. Sato, K. Minamisono, T. Yamaguchi, T. Onishi, T. Miyake, M. Sasaki et al., Recent studies on the nuclear moments of light mirror nuclei ($T = 1/2, 3/2$), Nucl. Phys. A **704**, 98c (2002).

[147] D. Sundholm and J. Olsen, Nuclear quadrupole moments of ^{33}S and ^{35}S, Phys. Rev. A **42**, 1160 (1990).

[148] Y. Utsuno et al., Extreme location of F drip line and disappearance of the $N = 20$ magic structure, Phys. Rev. C **64**, 011301(R) (2001).

[149] Y. Utsuno, T. Otsuka, T. Mizusaki, and M. Honma, et al., Varying shell gap and deformation in $N \sim 20$ unstable nuclei studied by the Monte Carlo shell model, Phys. Rev. C **60**, 054315 (1999).

[150] D. T. Yordanov, M. L. Bissell, K. Blaum, M. De Rydt, C. Geppert, J. Kramer, K. Kreim, M. Kowalska, A. Krieger, P. Lievens et al., Spin and magnetic moment of ^{23}Mg, J. Phys. G **44**, 075104 (2017).

[151] A. O. Macchiavelli, H. L. Crawford, C. M. Campbell, R. M. Clark, M. Cromaz, P. Fallon, M. D. Jones, I. Y. Lee, M. Salathe, B. A. Brown, and A. Poves, The ^{30}Mg$(t,p)^{32}$Mg "puzzle" reexamined, Phys. Rev. C **94**, 051303(R) (2016).

[152] A. Kusoglu, A. E. Stuchbery, G. Georgiev, B. A. Brown, A. Goasduff, L. Atanasova, D. L. Balabanski, M. Bostan, M. Danchev, P. Detistov et al., Magnetism of an Excited Self-Conjugate Nucleus: Precise Measurement of the g Factor of the 2_1^+ State in ^{24}Mg, Phys. Rev. Lett. **114**, 062501 (2015).

[153] L. Huth, V. Durant, J. Simonis, ans A. Schwenk, Shell-model interactions from chiral effective field theory, Phys. Rev. C **98**, 044301 (2018).

[154] Y. Utsuno, T. Otsuka, B. A. Brown, M. Honma, T. Mizusaki, and N. Shimizu, Shape transitions in exotic Si and S isotopes and tensor-force-driven Jahn-Teller effect, Phys. Rev. C **86**, 051301(R) (2012).

[155] H. Iwasaki *et al.*, Quadrupole collectivity of ^{28}Ne and the boundary of the island of inversion, Phys. Lett. B **620**, 118 (2005).

[156] N. Tsunoda, T. Otsuka, N. Shimizu, M. Hjorth-Jensen, K. Takayanai, and T. Suzuki, Exotic neutron-rich medium-mass nuclei with realistic nuclear forces, Phys. Rev. C **95**, 021304(R) (2017).

[157] A. Saxena, A. Kumar, V. Kumar, P. C. Srivastava, and T. Suzuki, *Ab initio* description of collectivity for *sd* shell nuclei, Hyperfine Int. **240**, 37 (2019).

[158] J. Suhonen, From Nucleons to Nucleus, Concepts of Microscopic Nuclear Theory, Springer (2007).

[159] P. K. Rath, H. Müther, A. Polls, A. Faessler, B. Metsch, and D. Zwarts, Spectra of sd-shell nuclei and three-nucleon forces, Nucl. Phys. A **427**, 511 (1984).

[160] P. K. Raina, A. Shukla, S. Singh, P.K. Rath, and J. G. Hirsch, The $0^+ \rightarrow 0^+$ positron double- β decay with emission of two neutrinos in the nuclei ^{96}Ru, ^{102}Pd, ^{106}Cd and ^{108}Cd, Eur. Phys. J. A **28**, 27 (2006).

[161] A. K. Singh, and G. Gangopadhyay, β decay in the mass 60 region in the framework of the interacting boson approximation,Phys. Rev. C **55**, 2734 (1997).

[162] E. Caurier, A. Poves, and A. P. Zuker, Missing and Quenched Gamow-Teller Strength, Phys. Rev. Lett. **74**, 1517 (1995).

[163] A. L. Cole, T. S. Anderson, R. G. T. Zegers, Sam M. Austin, B. A. Brown, L. Valdez, S. Gupta, G. W. Hitt, and O. Fawwaz, Gamow-Teller strengths and electron-capture rates for pf-shell nuclei of relevance for late stellar evolution, Phys. Rev. C **86**, 015809 (2012).

[164] P. Sarriguren, Contribution of excited states to stellar weak-interaction rates in odd-A nuclei, Phys. Rev. C **93**, 054309 (2016).

[165] A. Negret, T. Adachi, B. R. Barrett, C. Bumer, A. M. van den Berg, G. P. A. Berg, P. von Brentano, D. Frekers, D. De Frenne, H. Fujita et al., Gamow-Teller Strengths in the $A = 14$ Multiplet: A Challenge to the Shell Model, Phys. Rev. Lett. **97**, 062505 (2006).

[166] V. Kumar, and P.C. Srivastava, Shell model description of Gamow-Teller strenghts in pf-shell nuclei, Eur. Phys. J. A **52**, 181 (2016).

[167] V. Kumar, P.C. Srivastava and H. Li, Nuclear β^--decay half-lives for fp and fpg shell nuclei, J.Phys. G **43**, 105104 (2016).

[168] K. Langanke, and G. Martínez-Pinedo, Nuclear weak-interaction processes in stars, Rev. Mod. Phys. **75**, 819 (2003).

[169] Y. Fujita, B. Rubio, and W. Gelletly, Spin-isospin excitations probed by strong, weak and electro-magnetic interactions, Prog. Part. Nucl. Phys. **66**, 549 (2011).

[170] K.G. Balasi, K. Langanke, and G. Martínez-Pinedo, Neutrino-nucleus reactions and their role for supernova dynamics and nucleosynthesis, Prog. Part. Nucl. Phys. **85**, 33 (2015).

[171] T. Suzuki, M. Honma, Hélène Mao, T. Otsuka and T. Kajino, Evaluation of electron capture reaction rates in Ni isotopes in stellar environments, Phys. Rev. C **83**, 044619 (2011).

[172] G. Martínez-Pinedo, Y. H. Lam, K. Langanke, R. G. T. Zegers, and C. Sullivan, Astrophysical weak interaction rates for selected $A = 20$ and $A = 24$ nuclei, Phys. Rev. C **89**, 045806 (2014).

[173] S. E. Woosley, D. H. Hartmann, R. D. Hoffman, and W. C. Haxton, The ν-process, Astrophys. J. **356**, 272 (1990).

[174] A. Heger, E. Kolbe, W. C. Haxton, K. Langanke, G. Martinez-Pinedo, and S. E. Woosley, Neutrino nucleosynthesis, Phys. Lett. B **606**, 258 (2005).

[175] T. Suzuki, and T. Kajino, Element synthesis in the supernova environment and neutrino oscillations, J. Phys. G **40**, 083101 (2013).

[176] A. Byelikov, T. Adachi, H. Fujita, K. Fujita, Y. Fujita, K. Hatanaka, A. Heger, Y. Kalmykov, K. Kawase, K. Langanke et al., Gamow-Teller Strength in the Exotic Odd-Odd Nuclei ^{138}La and ^{180}Ta and Its Relevance for Neutrino Nucleosynthesis, Phys. Rev. Lett. **98**, 082501 (2007).

[177] H. Hergert, S. K. Bogner, S. Binder, A. Calci, J. Langhammer, R. Roth, and A. Schwenk, In-medium similarity renormalization group with chiral two-plus three-nucleon interactions, Phys. Rev. C **87**, 034307 (2013).

[178] D. J. Dean, and M. Hjorth-Jensen, Coupled-cluster approach to nuclear physics, Phys. Rev. C **69**, 054320 (2004).

[179] V. Soma, A. Cipollone, C. Barbieri, P. Navrátil, and T. Duguet, Chiral two- and three-nucleon forces along medium-mass isotope chains, Phys. Rev. C **89**, 061301 (2014).

[180] P. Navrátil, V. G. Gueorguiev, J. P. Vary, W. E. Ormand, and A. Nogga, Structure of $A = 10 - 13$ Nuclei with Two- Plus Three-Nucleon Interactions from Chiral Effective Field Theory, Phys. Rev. Lett. **99**, 042501 (2007).

[181] P. Navrátil and W. E. Ormand, *Ab initio* shell model with a genuine three-nucleon force for the p-shell nuclei Phys. Rev. C **68**, 034305 (2003).

[182] B. W. Pointon, O. Häusser, R. Henderson, A. Celler, K. Hicks, K. P. Jackson, R. Jeppesen, B. Larson, J. Mildenberger, A. Trudel, et al., Gamow-Teller strength from the ^{20}Ne$(n, p)^{20}$F reaction at E_n=198 MeV, Phys. Rev. C **44**, 2430 (1991).

[183] Y. Fujita, Y. Shimbara, I. Hamamoto, T. Adachi, G. P. A. Berg, H. Fujimura, H. Fujita, J. Görres, K. Hara, K. Hatanaka et al., $M1$ and Gamow-Teller transitions in $T = 1/2$ nuclei ^{23}Na and ^{23}Mg, Phys. Rev. C **66**, 044313 (2002).

[184] B. Siebels, T. P. Gorringe, W. P. Alford, J. Bauer, J. Evans, S. El-Kateb, K. P. Jackson, A. Trudel, and S. Yen, Gamow-Teller strength in ^{23}Na(n, p) and a comparison to ^{23}Na(μ^-,ν), Phys. Rev. C **52**, 1488 (1995).

[185] M. E. Howard, R. G. T. Zegers, Sam M. Austin, D. Bazin, B. A. Brown, A. L. Cole, B. Davids, M. Famiano, Y. Fujita, A. Gade et al., Gamow-Teller strengths in ^{24}Na using the ^{24}Mg$(t, ^3$He$)$ reaction at 115A MeV, Phys. Rev. C **78**, 047302 (2008).

[186] S. Rakers, C. Bäumer, D. Frekers, R. Schmidt, A. M. van den Berg, V. M. Hannen, M. N. Harakeh, M. A. de Huu, H. J. Wörtche, D. De Frenne et al., Gamow-Teller matrix elements from the ^{12}C$(d,^2$He$)$ and ^{24}Mg$(d,^2$He$)$ reactions at 170 MeV, Phys. Rev. C **65**, 044323 (2002).

[187] B. D. Anderson, N. Tamimi, A. R. Baldwin, M. Elaasar, R. Madey, D. M. Manley, M. Mostajabodda'vati, J. W. Watson, W. M. Zhang, and C. C. Foster, Gamow-Teller strength in the (p, n) reaction at 136 MeV on ^{20}Ne, ^{24}Mg, and ^{28}Si, Phys. Rev. C **43**, 50 (1991).

[188] R. G. T. Zegers, R. Meharchand, T. Adachi, Sam M. Austin, B. A. Brown, Y. Fujita, M. Fujiwara, C. J. Guess, H. Hashimoto, K. Hatanaka et al., Spectroscopy of ^{24}Al and extraction of Gamow-Teller strengths with the ^{24}Mg$(^3$He$,t)$ reaction at 420 MeV, Phys. Rev. C **78**, 014314 (2008).

[189] Y. Shimbara, Y. Fujita, T. Adachi, G. P. A. Berg, H. Fujita, K. Fujita, I. Hamamoto, K. Hatanaka, J. Kamiya, K. Nakanishi et al., Suppression of Gamow-Teller and $M1$ transitions in deformed mirror nuclei ^{25}Mg and ^{25}Al, Eur. Phys. J. A. **19**, 25-31 (2004).

[190] R. G. T. Zegers, H. Akimune, Sam M. Austin, D. Bazin1, A. M.van den Berg, G. P. A. Berg, B. A. Brown, J. Brown, A. L. Cole, I. Daito et al., The $(t,^3\mathrm{He})$ and $(^3\mathrm{He}, t)$ reactions as probes of Gamow-Teller strength, Phys. Rev. C **74**, 024309 (2006).

[191] T. Niizeki, H. Ohnuma, T. Yamamoto, K. Katoh, T. Yamashita, Y. Hara, H. Okamura, H. Sakai, S. Ishida, N. Sakamoto et al., Spin-isospin excitation in *sd*-shell nuclei studied by the $(d, {}^2\mathrm{He})$ reaction at E_d=270 MeV, Nucl. Phys. A **577**, 37 (1994).

[192] R. Madey, B. S. Flanders, B. D. Anderson, A. R. Baldwin, C. Lebo, J. W. Watson, Sam M. Austin, A. Galonsky, B. H. Wildenthal, and C. C. Foster, Gamow-Teller strength in the $^{26}\mathrm{Mg}(p,n)^{26}\mathrm{Al}$ reaction at 135 MeV and its fractionation into $T = 0$, 1, and 2 isospin channels, Phys. Rev. C **35**, 2011 (1987); **36**, 1647 (1987).

[193] Y. Fujita, Y. Shimbara, A. F. Lisetskiy, T. Adachi, G. P. A. Berg, P. von Brentano, H. Fujimura, H. Fujita, K. Hatanaka, J. Kamiya, et al., Analogous Gamow-Teller and $M1$ transitions in $^{26}\mathrm{Mg}$, $^{26}\mathrm{Al}$, and $^{26}\mathrm{Si}$, Phys. Rev. C **67**, 064312 (2003).

[194] Y. Fujita, H. Akimune, I. Daito, H. Fujimura, M. Fujiwara, M. N. Harakeh, T. Inomata, J. Jänecke, K. Katori, A. Tamii, et al., Mirror-symmetry structure of $A = 27$, $T = 1/2$ nuclei studied through strong, weak, and electromagnetic interactions, Phys. Rev. C **59**, 90 (1999).

[195] Y. Fujita, H. Akimune, I. Daito, M. Fujiwara, M. N. Harakeh, T. Inomata, J. Jänecke, K. Katori, C. Lüttge, S. Nakayama et al., Isospin and spin-orbital structures of $J^\pi = 1^+$ states excited in $^{28}\mathrm{Si}$, Phys. Rev. C **55**, 1137 (1997).

[196] R. M. Sedlar, T. P. Gorringe, W. P. Alford, D. A. Beatty, J. Campbell, H. T. Fortune, P. Hui, D. A. Hutcheon, R. B. Ivie, K. P. Jackson et al., Gamow-Teller strength in (n,p) charge exchange on $^{31}\mathrm{P}$, Phys. Rev. C **59**,789 (1999).

[197] E. W. Grewe, C. Bäumer, A. M. van den Berg, N. Blasi, B. Davids, D. De Frenne, D. Frekers, P. Haefner, M. N. Harakeh, M. Huynyadi, et al., Gamow-Teller transitions to $^{32}\mathrm{P}$ studied through the $^{32}\mathrm{S}(d,{}^2\mathrm{He})$ reaction at $E_d = 170$ MeV, Phys. Rev. C **69**, 064325 (2004).

[198] B. A. Brown, and B. H. Wildenthal, Status of the Nuclear Shell Model, Annu. Rev. Nucl. Part. Sci. **38**, 29 (1988).

[199] B. A. Brown, and B. H. Wildenthal, Corrections to the free-nucleon values of the single-particle matrix elements of the $M1$ and Gamow-Teller operators, from a comparison of shell-model predictions with sd-shell data, Phys. Rev. C **28**, 2397 (1983).

[200] B. H. Wildenthal, Empirical strengths of spin operators in nuclei, Prog. Part. Nucl. Phys. **11**, 5 (1984).

[201] T. Suzuki, A. Arima, and K.-I. Kubo, Mixing of the 0g orbit in ^{20}Ne and the analysis of a one-step forbidden transition, Nucl. Phys. A **288**, 493 (1977).

[202] B. Jeckelmann, W. Beer, I. Beltrami, F. W. N. de Boer, G. de Chambrier, P. F. A. Goudsmit, J. Kern, H. J. Leisi, W. Ruckstuhl, and A. Vacchi, Spectroscopic quadrupole moment of ^{23}Na from muonic X-rays, Nucl. Phys. A **408**, 495 (1983); P. Raghavan, Table of nuclear moments, At. Data Nucl. Data Tables **42**, 189 (1989).

[203] K. Matsuta, T. Onishi, M. Fukuda, T. Minamisono, H. Akai, M. Sasaki, T. Yamaguchi, T. Miyake , K. Sato, K. Minamisono et al., Electromagnetic moments of short lived β emitters ^{21}F, ^{23}Mg, ^{27}Si and ^{39}Ca, Hyperfine Interact. **120/121**, 673 (1999).

[204] N. M. Parzuchowski, S. R. Stroberg, P. Navrátil, H. Hergert, and S. K. Bogner, *Ab initio* electromagnetic observables with the in-medium similarity renormalization group, Phys. Rev. C **96**, 034324 (2017).

[205] G. M. Fuller, W. A. Fowler, and M. J. Newton, Stellar weak-interaction rates for *sd*-shell nuclei. I - Nuclear matrix element systematics with application to Al-26 and selected nuclei of importance to the supernova problem, Astrophys. J. Suppl. Ser., **42**, 447 (1980).

[206] G. M. Fuller, W. A. Fowler, and M. J. Newton, Stellar weak interaction rates for intermediate-mass nuclei. II - $A = 21$ to $A = 60$, Astrophys. J. **252**, 715 (1982).

[207] G. M. Fuller, W. A. Fowler, and M. J. Newton, Stellar weak interaction rates for intermediate mass nuclei. III - Rate tables for the free nucleons and nuclei with $A = 21$ to $A = 60$, Astrophys. J. **48**, 279 (1982).

[208] G. M. Fuller, W. A. Fowler, and M. J. Newton, Stellar weak interaction rates for intermediate-mass nuclei. IV - Interpolation procedures for rapidly varying lepton capture rates using effective log (ft)-values, Astrophys. J. **293**, 1 (1985).

[209] H. Toki, T. Suzuki, K. Nomoto, S. Jones, and R. Hirsci, Detailed β transition rates for URCA nuclear pairs in 8-10 solar-mass stars, Physical Review C **88**, 015806 (2013).

[210] T. Suzuki, H. Toki, and K. Nomoto, Electron-capture and β-decay rates for *sd*-shell nuclei in stellar environments relevant to high-density O-Ne-Mg cores, Astrophys. J. **817**, 163 (2016).

[211] K. Wimmer, T. Kröll, R. Krücken, V. Bildstein, R. Gernhäuser, B. Bastin, N. Bree, J. Diriken, P. Van Duppen, M. Huyse et al., Discovery of the Shape Coexisting 0^+ State in ^{32}Mg by a Two Neutron Transfer Reaction, Phys. Rev. Lett. **105**, 252501 (2010).

[212] T. Motobayashi Y. Ikeda, Y. Ando, K. Ieki, M. Inoue, N. Iwasa, T. Kikuchi, M. Kurokawa, S. Moriya, S. Ogawa, et al., Large deformation of the very neutron-rich nucleus ^{32}Mg from intermediate-energy Coulomb excitation, Phys. Lett. B **346**, 9 (1995).

[213] B. Bastin, S. Grevy, D. Sohler, O. Sorlin, Zs.Dpmbrádi N. L. Achouri, J. C. Angélique, F. Azaiez, D. Baiborodin, R. Borcea, et al., Collapse of the $N = 28$ Shell Closure in ^{42}Si, Phys. Rev. Lett. **99**, 022503 (2007).

[214] C. Force, S. Grévy, L. Gaudefroy, O. Sorlin, L. Cáceres, F. Rotaru, J. Mrazek, N. L. Achouri, J. C. Angélique, F. Azaiez, et al., Prolate-Spherical Shape Coexistence at $N = 28$ in ^{44}**S**, Phys. Rev. Lett. **105**, 102501 (2010).

[215] R. Chevrier, J. M. Daugas, L. Gaudefroy, Y. Ichikawa, H. Ueno, M. Hass, H. Haas, S. Cottenier, N. Aoi, K. Asahi, et al., Is the $7/2^-_1$ Isomer State of ^{43}S Spherical ?, Phys. Rev. Lett. **108**, 162501 (2012).

[216] R. Winkler, A. Gade, T. Baugher, D. Bazin, B. A. Brown, T. Glasmacher, G. F. Grinyer, R. Meharchand, S. McDaniel, A. Ratkiewicz, and D. Weisshaar, Quadrupole Collectivity beyond $N = 28$: Intermediate-Energy Coulomb Excitation of ^{47,48}Ar, Phys. Rev. Lett. **108**, 182501 (2012).

[217] G. Neyens, M. Kowalska, D. Yordanov, K. Blaum, P. Himpe, P. Lievens, S. Mallion, R. Neugart, N. Vermeulen, Y. Utsuno, and T. Otsuka, Measurement of the Spin and Magnetic Moment of ^{31}Mg: Evidence for a Strongly Deformed Intruder Ground State, Phys. Rev. Lett. **94**, 022501 (2005).

[218] A. O. Macchiavelli, H. L. Crawford, C. M. Campbell, R. M. Clark, M. Cromaz, P. Fallon, M. D. Jones, I. Y. Lee, M. Salathe, B. A. Brown, and A. Poves, The ^{30}Mg$(t,p)^{32}$Mg "puzzle" reexamined, Phys. Rev. C **94**, 051303(R) (2016).

[219] S. Nummela, F. Nowacki, P. Baumann, E. Caurier, J. Cederkäll, S. Courtin, P. Dessagne, A. Jokinen, A. Knipper, G. Le Scornet, et al., Intruder features in the island of inversion: The case of ^{33}Mg, Phys. Rev. C **64**, 054313 (2001).

[220] V. Tripathi, S. L. Tabor, P. Bender, C. R. Hoffman, Sangjin Lee, K. Pepper, M. Perry, P. F. Mantica, J. M. Cook, J. Pereira, et al., Excited intruder states in ^{32}Mg, Phys. Rev. C **77**, 034310 (2008).

[221] D. T. Yordanov, M. Kowalska, K. Blaum, M. De Rydt, K. T. Flanagan, P. Lievens, R. Neugart, G. Neyens, and H. H. Stroke, Spin and Magnetic Moment of ^{33}Mg: Evidence for a Negative-Parity Intruder Ground State, Phys. Rev. Lett. **99**, 212501 (2007).

[222] R. Kanungo, C. Nociforo, A. Prochazka, Y. Utsuno, T. Aumann, D. Boutin, D. Cortina-Gil, B. Davids, M. Diakaki, F. Farinon, et al., Structure of ^{33}Mg sheds new light on the N=20 island of inversion, Phys. Lett. B **685**, 253 (2010).

[223] A. Gade, B. A. Brown, D. Bazin, C. M. Campbell, J. A. Church, D. C. Dinca, J. Enders, T. Glasmacher, M. Horoi, Z. Hu, et al.,Evolution of the $E(1/2_1^+) - E(3/2_1^+)$ energy spacing in odd-mass K, Cl, and P isotopes for $N = 20-28$, Phys. Rev. C **74**, 034322 (2006).

[224] O. Sorlin, Zs. Dombrádi, D. Sohler, F. Azaiez, J. Timár, Yu. -E. Penionzhkevich, F. Amorini, D. Baiborodin, A. Bauchet, F. Becker, et al., Structure of the neutron-rich ^{37,39}P and ^{43,45}Cl nuclei, Eur. Phys. J. A **22**, 173 (2004).

[225] M. De Rydt, J. M. Daugas, F. de Oliveira Santos, L. Gaudefroy, S. Grévy, D. Kameda, V. Kumar, R. Lozeva, T. J. Mertzimekis, P. Morel, et al., g factor of the ^{44}Cl ground state: Probing the reduced $Z = 16$ and $N = 28$ gaps, Phys. Rev. C **81**, 034308 (2010).

[226] R. Broda, J. Wrzesiński, A. Gadea, N. Mărginean, B. Fornal, L. Corradi, A. M. Stefanini, W. K rólas, T. Pawłat, B. Szpak, et al., Proton-hole states in the $N = 30$ neutron-rich isotope ^{49}K, Phys. Rev. C **82**, 034319 (2010).

[227] S. Bhattacharyya, M. Rejmund, A. Navin, E. Caurier, F. Nowacki, A. Poves, R. Chapman, D. O'Donnell, M. Gelin, A. Hodsdon, et al., Structure of Neutron-Rich Ar Isotopes Beyond $N = 28$, Phys. Rev. Lett. **101**, 032501 (2008).

[228] J. Ljungvall, A. Görgen, A. Obertelli, W. Korten, E. Clément, G. de France, A. Bürger, J.-P. Delaroche, A. Dewald, A. Gadea, et al., Onset of collectivity in neutron-rich Fe isotopes: Toward a new island of inversion ?, Phys. Rev. C **81**, 061301 (2010).

[229] E. Caurier, F. Nowacki, and A. Poves, Merging of the islands of inversion at $N = 20$ and $N = 28$, Phys. Rev. C **90**, 014302 (2014).

[230] Z. M. Wang, R. Chapman, X. Liang, F. Haas, F. Azaiez, B. R. Behera, M. Burns, E. Caurier, L. Corradi, D. Curien, et al., γ-ray spectroscopy of neutron-rich ^{40}S, Phys. Rev. C **81**, 054305 (2010).

[231] H. Scheit, T. Glasmacher, B. A. Brown, J. A. Brown, P. D. Cottle, P. G. Hansen, R. Harkewicz, M. Hellström, R. W. Ibbotson, J. K. Jewell, et al., New Region of Deformation: The Neutron-Rich Sulfur Isotopes, Phys. Rev. Lett. **77**, 3967 (1996).

[232] Z. M. Wang, R. Chapman, F. Haas, X. Liang, F. Azaiez, B. R. Behera, M. Burns, L. Corradi, D. Curien, A. N. Deacon, et al., Collectivity in ^{41}S, Phys. Rev. C **83**, 061304 (2011).

[233] L. Gaudefroy, J. M. Daugas, M. Hass, S. Grévy, Ch. Stodel, J. C. Thomas, L. Perrot, M. Girod, B. Rossé, J. C. Angélique, et al., Shell Erosion and Shape Coexistence in $^{43}_{16}S_{27}$, Phys. Rev. Lett. **102**, 092501 (2009).

[234] L. Cáceres, D. Sohler, S. Grévy, O. Sorlin, Zs. Dombrádi, B. Bastin, N. L. Achouri, J. C. Angélique, F. Azaiez, D. Baiborodin, et al., In-beam spectroscopic studies of the ^{44}S nucleus, Phys. Rev. C **85**, 024311 (2012).

[235] T. R. Rodríguez and J. L. Egido, Configuration mixing description of the nucleus ^{44}S, Phys. Rev. C **84**, 051307 (2011).

[236] D. Sohler, Zs. Dombrádi, J. Timár, O. Sorlin, F. Azaiez, F. Amorini, M. Belleguic, C. Bourgeois, C. Donzaud, J. Duprat, et al., Shape evolution in heavy sulfur isotopes and erosion of the $N = 28$ shell closure, Phys. Rev. C **66**, 054302 (2002).

[237] D. Santiago-Gonzalez, I. Wiedenhöver, V. Abramkina, M. L. Avila, T. Baugher, D. Bazin, B. A. Brown, P. D. Cottle, A. Gade, T. Glasmacher, et al., Triple configuration coexistence in ^{44}S, Phys. Rev. C **83**, 061305 (2011).

[238] A. D. Davies, Ph.D. thesis, Michigan State University (2006).

[239] S. Aydin, M. Ionescu-Bujor, F. Recchia, S. M. Lenzi, M. Bouhelal, D. Bazzacco, P. G. Bizzeti, A. M. Bizzeti-Sona, G. de Angelis, I. Deloncle, et al., High-spin level structure of ^{35}S, Phys. Rev C **89**, 014310 (2014).

[240] R. Chapman, Z. M. Wang, M. Bouhelal, F. Haas, X. Liang, F. Azaiez, B. R. Behera, M. Burns, E. Caurier, L. Corradi, et al., Particle-core coupling in ^{37}S, Phys. Rev C **93**, 044318 (2016).

[241] K. Kaneko, Y. Sun, T. Mizusaki, and M. Hasegawa, Shell-model study for neutron-rich *sd*-shell nuclei, Phys. Rev. C **83**, 014320 (2011).

[242] M. Bouhelal, F. Haas, E. Caurier, F. Nowacki and A. Bouldjedri, A PSDPF interaction to describe the $1\hbar\omega$ intruder states in sd shell nuclei, Nucl. Phys. A **864**, 113 (2011).

[243] R. Chapman, Z. M. Wang, M. Bouhelal, F. Haas, X. Liang, F. Azaiez, B. R. Behera, M. Burns, E. Caurier, L. Corradi, et al., First in-beam γ-ray study of the level structure of neutron-rich ^{39}S, Phys. Rev. C **94**, 024325 (2016).

[244] NuShell@MSU, B. A. Brown and W. D. M. Rae, MSU-NSCL report (2007).

[245] B. H. Wildenthal, Empirical strengths of spin operators in nuclei, Prog. Part. Nucl. Phys. **11**, 5 (1984).

[246] D. H. Gloeckner, and R. D. Lawson, Spurious center-of-mass motion, Phys. Lett. B **53**, 313 (1974).

[247] S. Pisko and P. Franc, and J. Kemnek and W. Schferlingov, Spectroscopic information on ^{35}S and ^{37}S from the (d, p) reaction, Nucl. Phys. A **414**, 219 (1984).

[248] B. K. Agrawal, S. K. Dhiman, and R. Kumar, Exploring the extended density-dependent Skyrme effective forces for normal and isospin-rich nuclei to neutron stars, Phys. Rev. C **73**, 034319 (2006).